Finite Temperature Corrections to Dark Matter Annihilation Cross Sections using Thermal Field Theory

By

Prabhat Butola
PHYS10201804001

The Institute of Mathematical Sciences, Chennai

A thesis submitted to the

Board of Studies in Physical Sciences

In partial fulfillment of requirements
For the Degree of
DOCTOR OF PHILOSOPHY
of
HOMI BHABHA NATIONAL INSTITUTE

July, 2025

Homi Bhabha National Institute[1]

Recommendations of the Viva Voce Committee

As members of the Viva Voce Committee, we certify that we have read the dissertation prepared by **Prabhat Butola**, entitled "*Finite Temperature Corrections to Dark Matter Annihilation Cross Sections using Thermal Field Theory*" and recommend that it may be accepted as fulfilling the thesis requirement for the award of Degree of Doctor of Philosophy.

S.N.	Doctoral Committee	Name	Signature	Date	In-person /Online
1.	Chairman	Shrihari Gopalakrishna		17.11.25	In-P
2.	Guide/Convener	D. Indumathi	D. Indumathi	17.11.25	In-P
3.	Coguide(if any)	–			
4.	Examiner	Priyotosh Bandyopadhyay		17.11.25	In-P
5.	Member-1	V. Ravindran	V. Ravindran	17.11.25	In-P
6.	Member-2	Manjari Bagchi	Manjari Bagchi	17.11.25	In-P
7.	Member-3	Pinaki Choudhuri		17.11.25	In-P
8.	Member-4	James Libby		17.11.25	In-P
9.	Advisor (if any)	–			

Final approval and acceptance of this thesis is contingent upon the candidate's submission of the final copies of the thesis to HBNI.

I/We hereby certify that I/we have read this thesis prepared under my/our direction and recommend that it may be accepted as fulfilling the thesis requirement.

Date: 17.11.2025

Place: IMSc, Chennai

Signature

Co-guide (if any)

Signature D. Indumathi

Guide : D. Indumathi

---

[1] This page is to be included only for final submission after successful completion of viva voce.

STATEMENT BY AUTHOR

This dissertation has been submitted in partial fulfillment of requirements for an advanced degree at Homi Bhabha National Institute (HBNI) and is deposited in the Library to be made available to borrowers under rules of the HBNI.

Brief quotations from this dissertation are allowable without special permission, provided that accurate acknowledgment of source is made. Requests for permission for extended quotation from or reproduction of this manuscript in whole or in part may be granted by the Competent Authority of HBNI when in his or her judgment the proposed use of the material is in the interests of scholarship. In all other instances, however, permission must be obtained from the author.

Prabhat Butola.

Prabhat Butola

DECLARATION

I hereby declare that the investigation presented in the thesis has been carried out by me. The work is original and has not been submitted earlier as a whole or in part for a degree / diploma at this or any other Institution / University.

Prabhat Butola

Prabhat Butola

CERTIFICATION ON ACADEMIC INTEGRITY

Undertaking by the Student

1. I Prabhat Butola, HBNI Enrolment No.**PHYS10201804001,** hereby undertake that the Thesis, titled "**Finite Temperature Corrections to Dark Matter Annihilation Cross Sections using Thermal Field Theory**" is prepared by me and is the original work undertaken by me.

2. I also hereby undertake that this document has been duly checked through a plagiarism detection tool and the document is found to be plagiarism free as per the guidelines of the Institute/ UGC.

3. I am aware and undertake that if plagiarism is detected in my thesis at any stage in the future, suitable penalty will be imposed as per the guidelines of the Institute/ UGC.

Prabhat Butola. (17/11/2025)
Signature of the Student with date

Endorsed by the Thesis Supervisor:

I certify that the thesis written by the researcher is plagiarism free as mentioned above by the student.

D. Indumathi

Signature of the Thesis Supervisor with Date and Name: D. Indumathi, Nov 25, 2025
Designation: Prof H
Department/ Centre: IMSc
Name of the CI/ OCC: IMSc

List of Publications arising from the thesis

Journal :

1. "NLO thermal corrections to dark matter annihilation cross sections: A novel approach", Prabhat Butola, D. Indumathi and Pritam Sen,Phys.Rev.D 110 (2024) 3, 036006

Submitted to Journal :

1. "Thermal corrections to dark matter annihilation with real photon emission/absorption", Prabhat Butola, D. Indumathi and Pritam Sen, arXiv : 2506.07663

Conferences :

1. "Thermal Corrections to Dark Matter Annihilation Processes", Prabhat Butola, D. Indumathi and Pritam Sen,Springer Proc.Phys. 304 (2024) 994-996
2. "Effect of thermal fluctuations on dark matter annihilation cross section", Prabhat Butola, D. Indumathi and Pritam Sen, PoS ICHEP2024 (2025) 719

.

Name & Signature
of the student
Prabhat Butola

Prabhat Butola.

List of Presentations at Conferences

1. Poster presentation at 25th DAE-BRNS High energy physics Symposium , IISER Mohali,2022 on *Thermal Corrections to Dark Matter Annihilation Processes*.
2. Talk at Phoenix, IIT Hyderabad, Phoenix- 2023, IIT Hyderabad, *Thermal Corrections to Dark Matter Annihilation Processes at NLO*.
3. Poster at 42nd International Conference on High Energy Physics (ICHEP 2024), Prague, 2024 on *Effect of thermal fluctuations on dark matter annihilation cross section*.
4. Poster presentation at Trends in Astroparticle and Particle Physics, IMSc, Chennai, Sep. 2024,*Application of thermal field theory to dark matter annihilation cross section*.
5. Talk at 17th International Conference on Interconnections between Particle Physics and Cosmology (PPC 2024), IIT, Hyderabad, Oct 2024, *Thermal correction to dark matter annihilation processes through real photon emission and absorption*.

ACKNOWLEDGEMENTS

I would like to express my sincere gratitude to my supervisor, Prof. D. Indumathi, for her valuable guidance, crucial academic advices and scholarly inputs I have received throughout my doctoral endeavor. I am grateful for her to nourishing me in my academic advancement.

I would like to thank my collaborator and brother like friend Dr. Pritam Sen for precious physics discussions and for collaboration.

I thank Prof. Shrihari Gopalakrishna, Prof. V. Ravindran, Prof. Shankha Banerjee and Prof. D. Indumathi for their valuable advices and deep physics discussions. I would like to thank members of the doctoral committee for their valuable suggestions. I would like to thank Prof. V. Ravindran, Prof. Nita Sinha, Prof. Rahul Sinha, Prof. Nemani V. Suryanarayana, Prof. R. Rajesh, Prof. M. V. N. Murthy, Prof. Shrihari Gopalakrishna and Prof. D. Indumathi for their great courses in physics.

I learnt a great deal of physics from the pheno journal club and would like to thank all the members of PhenoJC. I thank Prof. Sayantan Sharma for giving me opportunity to organize PhenoJC and enjoyed organizing PhenoJC with Aparna and Shivam.

I would like to thank Pritam, Tousik, Biswajit, Purusottam, Ratan, Navdeep, Juhi, Disha, Shivam, Suprabh, Vishudath and Shubham for fruitful discussion on physics and on the other aspects of life.

I would like to thank all my classmates, seniors and juniors and office-mates for making life in IMSc memorable. I enjoyed intellectual and amusing discussions while dinner and lunch and at office with Vinod, Apurba, Sushovan, Tanmay, Jyotijwal, Ankur, Amit, Hitesh, Saurav, Vaibhav, Harshit, Goutham, Arindam, Pritam and other colleagues at IMSc family. I enjoyed playing tennis with Suraj, Tirtharaj and Sushant. I thank Jitin for taking me in his team for cosmic ray demonstration at IMSc open day.

I thank Administration staff, Library staff and Technical staff for providing quick support whenever needed. Special thanks to Srinivasan for his fast technical support. I would also like to thank staff at IMSc canteen for providing us quality food.

I would like to thank my parents, Brother and Sister-in-Law for their love, support and believing in me.

Abstract

We present the finite temperature higher order corrections to the annihilation cross section of Majorana and Dirac type dark matter candidates considering a model in which the dark matter, χ, annihilates to Standard Model fermion pairs via a scalar portal having Yukawa interaction, $\mathcal{L} \supset (\lambda\, \overline{\chi} P_L f^- \phi^+ + h.c.)$. The finite temperature corrections are computed for virtual photon corrections to the cross section for the process $\chi\chi \to f\overline{f}$ at next-to-leading order in the QED coupling constant as well as to real photon emission and absorption process $\chi\overline{\chi} \to f\overline{f}(\gamma)$. We use techniques of thermal field theory in order to calculate these finite temperature corrections. At finite temperature there are no ultra-violet divergences due to the presence of the Bose-Einstein or Fermi-Dirac distribution functions which act as a regulator; however, infra-red and collinear divergences are still present. We use the generalized technique of Grammer and Yennie to factorise the photon propagator into an infra-red-safe and infra-red-divergent part in order to deal with the soft divergences. We show the cancellation of infra-red divergences among complementary diagrams between the virtual photon correction and real photon correction to the dark matter annihilation process at next-o-leading order (at $\mathcal{O}(\alpha)$). We note that the thermal correction in the virtual case appears due to the finite temperature terms in the photon and fermion propagators whereas the thermal correction in the real photon case appears due to finite temperature terms in the phase space factors. In our study we consider the mediator scalar to be heavy compared to the dark matter particles and fermions $m_\phi > m_\chi \gg m_f$. We find the cross section at both leading and next-to-leading order to be helicity suppressed for Majorana dark matter, whereas helicity suppression is lifted for Dirac dark matter. We finally present the dominant thermal corrections to the dark matter annihilation cross section at this order, keeping terms up-to quadratic order in fermion mass m_f^2 at $\mathcal{O}(T^2)$.

Contents

Summary of the Thesis

The core content of this thesis is the computation of thermal higher order corrections to dark matter annihilation cross sections into standard model fermions using the techniques of thermal quantum field theory. This cross section plays an important role in the collision term in the Boltzmann equation for the evolution of the dark matter density n_χ in the Universe. The Boltzmann equation can be solved to determine the relic density of dark matter in today's Universe, that is, the dark matter density left over today from the early Universe, after the Big Bang; this is extremely precisely measured today.

The collision term involves the thermal average of the dark matter annihilation cross section σ, to be precise, the product, $\sigma_{\chi\bar{\chi}\to ij}\, v_{rel}$, where v_{rel} is the relative velocity between the annihilating particles:

$$\langle\sigma_{\chi\bar{\chi}\to ij} v_{rel}\rangle_T = \frac{1}{n_\chi^{eq} n_{\bar{\chi}}^{eq}} \int \frac{\mathrm{d}^3\vec{p}_\chi}{(2\pi)^3} \frac{\mathrm{d}^3\vec{p}_{\bar{\chi}}}{(2\pi)^3}\, f_\chi^{eq} f_{\bar{\chi}}^{eq}\, \sigma_{\chi\bar{\chi}\to ij}\, v_{rel}\,, \tag{1}$$

where the phase space distribution function is given by $f_\chi = n_\chi / n_\chi^{eq} \times f_\chi^{eq}$ (for details, see Chapter 1). The key point to note is that the thermal average of the *zero temperature* cross section is computed here. For consistency, the cross section must also be computed at the same temperature T of the thermal heat bath which comprises the early Universe. This is the main task in this thesis.

We first describe some relevant details of thermal quantum field theory in the real time formulation. We consider the interaction to occur at temperature T in a heat bath containing standard model fermions, photons and additional beyond-the-standard-model charged scalars and the dark matter χ, which interact with the standard model fermions through the scalars via a Yukawa interaction. We assume that electro-weak symmetry breaking has already occurred so that we can ignore the corrections due to heavy $W^{\pm}$ and Z^0 bosons and consider only the massless photon. We use the ensuing Feynman rules to compute these corrections. Both the thermal propagator and the phase space acquire temperature dependences proportional to the distribution function $n_B(\omega)$ (for bosons) and $n_F(\omega_t)$ (for fermions) where $\omega(E)$ is the energy of the photon (fermion):

$$n_B(\omega) = \frac{1}{\exp[\beta\omega] - 1}~, \qquad n_F(\omega_t) = \frac{1}{\exp[\beta\omega_t] + 1}~. \tag{2}$$

Due to the presence of the Bose distribution function for photons, we note also that the infra-red (IR) divergences are more severe in the case of thermal interactions than at zero temperature. This is because of the additional $1/\omega$ factor at small energies of the Bose distribution function. This gives rise to linear IR divergences and logarithmic sub-divergences in the thermal field theory (only logarithmic divergences occur in the zero temperature theory). We describe the Grammer and Yennie technique to handle the IR divergences in a simple and straightforward fashion.

We then compute the thermal corrections to both virtual next-to-leading order corrections to the cross section $\sigma(\chi\chi \to f\overline{f}$ and the real photon thermal corrections to $\sigma(\chi\chi \to f\overline{f}(\gamma))$ where (γ) indicates that the photon can be both emitted into and absorbed from the heat bath, in contrast to the zero temperature case where only emission is possible. All calculations have been performed assuming that the scalar is heavy compared to other particles. Our main findings are as follows:

1. The NLO thermal corrections when the dark matter particle is a Majorana fermion is helicity suppressed by a factor m_f^2, where m_f is the fermion mass, as in the leading order; these are not suppressed when the dark matter particle is Dirac type. This holds for both virtual and real photon thermal corrections

2. In addition, during this computation, we explicitly show the cancellation of both soft IR and collinear divergences between the virtual and real contributions, hence showing the consistency of the thermal field theory to NLO.

3. The ratio of the total NLO thermal correction to the leading order cross section is the same for both Majorana and Dirac DM. In the s-wave limit when the dark matter is highly non-relativistic, the leading thermal correction is

   $$\frac{\sigma_{NLO}}{\sigma_{LO}} = \frac{\alpha\pi}{6}\,\frac{T^2}{m_\chi^2}\,. \tag{3}$$

   The thermal corrections are small but they may be significant especially in freeze-in scenarios where $m_\chi/T \sim O(1)$. In any case, increasingly precise measurements of the dark matter relic density [1] indicate that more accurate estimates of the dark matter annihilation cross section may be of use.

We have presented in this thesis the finite temperature correction in the s-wave approximation; however, the complete results are listed in Mathematica notebooks on-line [2]) up-to $O(T^2)$. These may be useful for numerical computations in the solution of the Boltzmann equation.

In this thesis, we have presented thermal corrections to NLO of the dark matter annihilation cross sections. These need to be incorporated in the collision term of the Boltzmann equation to obtain a consistent calculation of the dark matter relic density today, which is being very precisely determined. We have not done so here, and leave it to future work.

There is nowadays a great deal of interest in such thermal corrections udder general considerations for various processes that occur not only in the early Universe but also in the presence of thermal plasma such as Quark Gluon Plasma. The theoretical underpinnings of thermal field theory, especially its soft and collinear divergences, are just being explored. This study is one such that aims to obtain a consistent approach to the problem of scattering in a heat bath.

List of Figures

List of Tables

Abbreviations

- SM : Standard Model of Particle Physics
- DM : Dark Matter
- CMB : Cosmic Microwave Background
- LSS : Large scale structure
- QFT : Quantum field theory
- TFT : Thermal field theory
- ACS : Annihilation cross section

Chapter 1

Introduction and Motivation

1.1 Introduction and Background

Modern theoretical physics leads us to two robust theories, one for dealing with infinitesimal scale problems i.e. Standard Model (SM) of Particle Physics and another for dealing with cosmic scale problems, the concordance model of cosmology, viz., ΛCDM. The technical framework for SM is given by quantum field theory and for ΛCDM, by Einstein's theory of General Relativity. There are unresolved problems in both the sectors; the problem of Dark Matter (DM) is one of them; it is basically the matter whose correct nature is unknown to us.

In the present day Universe, DM interacts with SM particles via only gravitation as per current understanding, which we infer from various observations. In particular, the exact particle nature of DM is unknown to us and we have only the option to test various possible models and constrain the parameter space for those models to be a fit candidate for DM. DM can be taken as relativistic or non-relativistic. In the ΛCDM model, dark matter is taken to be non-relativistic, we call it cold dark matter (CDM). Relativistic dark matter is called hot dark matter. A possible alternative is warm DM, having velocity between relativistic and non-relativistic regime. DM shares 84.4% of the total matter density of our Universe and 26.4 % of critical density of our Universe. Relic abundance of the dark matter is encoded in its relic density, measured to be $\Omega_c h^2 = 0.1200(12)$ [1, 3] where h is the reduced Hubble constant, $h = H_0/(100 \text{ km s}^{-1} \text{ MPc}^{-1})$ with a typical value of 0.67. Here H_0 is the rate at which the Universe is currently expanding, about 73 km/s/MPc. (Galaxies are receding from us with a velocity proportional to their distance; H_0 is the constant of proportionality.) The share of the baryonic matter in the energy density budget is $\Omega_b h^2 = 0.02237(15)$. The remaining energy, Dark Energy, is responsible for the expansion of our Universe.

The following is the list for the share of energy in different sectors of our Universe [1]: $\Omega_b = 0.0493(6)$, $\Omega_c = 0.265(7)$, $\Omega_\Lambda = 0.685(7)$. Here $\Omega_b, \Omega_c, \Omega_\Lambda$ are the energy density of baryonic matter, CDM and dark energy respectively, normalized by the critical density ρ_c $(= 3H_0/8\pi G_N \approx 10^{-26}\text{Kg m}^{-3})$ of our Universe.

1.2 A brief introduction to the Standard Model

The Standard Model of particle physics incorporates in it three fundamental interactions — strong, electromagnetic and weak interactions — and their force mediators along with the Higgs field that is responsible for mass generation; see Fig. 1.1. The gluon, photon and the $W^\pm$ and Z^0 bosons are the mediators respectively of these interactions. The gluon interacts with the colour charge of the quarks (and itself, via self-interactions), the photon with charged fields (all fermions such as quarks and charged leptons (other than the neutrinos) and the weak interactions with all particles. After electro-weak symmetry breaking (EWSB), the weak mediators W and Z become massive, and we have a massive Higgs boson. The set of particles can be written in terms of SU(2) left-doublets containing the up-type and down-type quarks in one doublet, and the charged lepton and its neutrino neutral partner in one doublet, with three generational copies of each. The right handed fields are SU(2) singlets [1] and the right handed neutrino does not exist. Furthermore, the quarks come in SU(3) copies due to their colour charge and are thus charged under the entire SM group of SU(3)$_c$ $\times$ SU(2)$_L$$\times$ U(1)$_Y$, where c represents colour, L the weak left-handed doublet, and Y the hypercharge. After EWSB, only SU(3)$_c$ and the sub-group U(1)$_{em}$ are left unbroken, where em represents the electromagnetic charge. All the particles listed here have been discovered, and many of the predictions of the SM regarding their interactions have been experimentally confirmed.

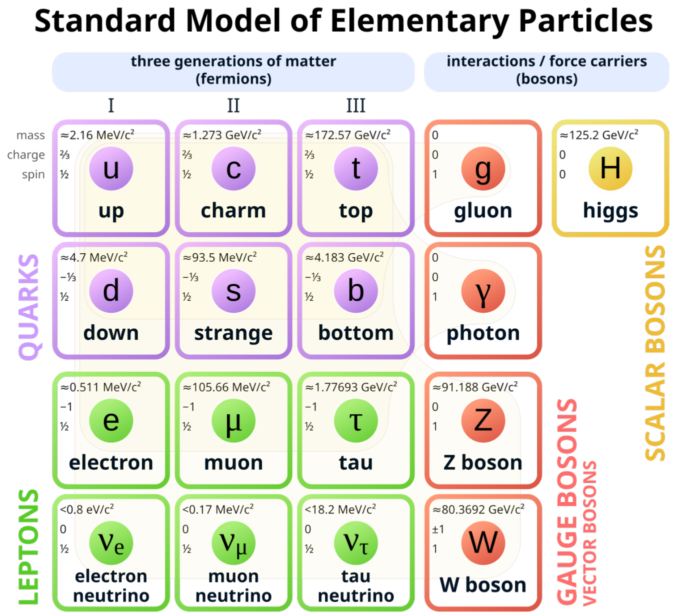

Figure 1.1: *Standard Model Particles and mediators; image courtesy Wikipedia.*

It can be seen that neutrinos, with their weak interactions are good candidates for Dark Matter [2]; however, most models of DM include additional particles that are outside the SM of particle physics. In particular, the model that we will consider in this thesis is of fermionic dark matter interacting with SM fermions through (integer) charged scalars. Hence the model is a simple one that only considers interactions with the (integer) charged leptons, e, μ, τ. Many detailed models exist in the literature as we will see below, but this theory captures the essence of the problem and enables us to discuss thermal effects in a

---

[1] SU(2) singlets are e_R, u_R, d_R and their three generations

[2] Neutrinos in SM are relativistic and most budget of the DM is cold in nature so SM neutrinos are only capable of filling small portion of the full budget of DM in our universe.

straightforward manner.

1.3 A brief introduction to Cosmology

The Big Bang Theory is the cosmological model that is favoured to explain the origin and evolution of the Universe from an extremely hot, dense state billions of years ago. It underwent a rapid phase of expansion called inflation, which is reflected in the extreme uniformity of the cosmic microwave background. As the Universe expanded, it also cooled; about 380,000 years after the Big Bang, the Universe cooled sufficiently so that protons and electrons combined to form neutral hydrogen. This allowed photons to decouple from matter and this light, seen as the cosmic microwave background (CMB) is an important evidence for inflation and big bang theory. The photon background is measured to be at a very low temperature of about 2.725K, and is red-shifted due to the expansion of the Universe, and its fluctuations are very small, of the order of 1 part in 10^4. However, these tiny fluctuations are very important and lead to the formation of galaxies and other large-scale structures. The preferred framework for the Big Bang theory is the ΛCDM model, which incorporates dark energy (via Λ) into Einstein's General Theory of Relativity, where massive objects curve space-time itself. The cosmological constant Λ represents the observed accelerating expansion of the Universe. The component of relevance for this thesis is the cold dark matter (CDM). It interacts very weakly with ordinary matter and radiation (described by SM). (Since neutrinos are nearly massless they are relativistic and hence not good candidates of CDM.) The "critical" energy density is defined as

$$\rho_c = \frac{3H^2}{8\pi G_N}\,, \tag{1.1}$$

where G_N is Newton's gravitational constant. Today, $\rho_c \approx 1.05 \times 10^{-5} h^2$ GeV/cm^3. The energy density of each component of the Universe is then expressed in terms of this critical density as Ω_C, where C stands for matter (Baryons), radiation (photons) or dark matter/energy, with the Universe being almost flat. Non-relativistic matter contributes about 31.43% of the budget (4.93(6)% baryonic and 26.5(7)% dark matter), while the remaining is in the form of unknown vacuum dark energy[3] [1]. The contribution of the dark energy makes our Universe about 13 billion years old (9 billion without dark energy).

DM is known to play an important role in the formation of large-scale structures like galaxies and galaxy clusters. While we do not understand the precise nature of this dark matter (and also dark energy, which we do not discuss further), there is abundant evidence for the existence of dark matter, which we now discuss.

1.4 Evidence for Dark Matter

In this thesis, we focus on calculations related to the theoretical determination of the dark matter relic density. Evidences for dark matter are found from cosmic scales ($\geq$ 100 MPc) to sub-galactic scales. At sub-galactic scales, we find evidence of dark matter in dwarf spheroidal galaxies (dSphs), analyzing the kinematics of stars and gas cloud in the dSphs [4]. At galactic scales dark matter was discovered via studies of galaxy rotation curves. In galaxy clusters we get evidence for dark matter from X-ray spectra of gas in the cluster as well as the gravitational lensing effects. At cosmic scales we get the evidence for dark matter through the analysis of the Cosmic Microwave Background (CMB) power spectrum, Large-Scale Structure (LSS) and Baryon acoustic oscillations (BAO). Other evidences come from the study of the Lyman-alpha forest. We shall delve into these evidences for dark matter next, in further detail.

---

[3] Dark energy budged is estimated to be 68.5(7) %.

1.4.1 The CMB Power Spectrum

At *cosmic scales*, robust evidence of dark matter comes from the analysis of temperature fluctuations in CMB. The all-sky map of CMB temperature has anisotropies and so it is not completely homogeneous. The temperature fluctuations in the map are further encoded into the temperature power spectrum; see Fig. 1.2. Among all known four forces, DM is sensitive to the gravitational force and further leads to regions of high gravitational potential regions in our Universe, after clumping due to the influence of gravity. Impact of those higher gravitational regions leaves an imprint on the CMB temperature map and further on the CMB temperature power spectrum.

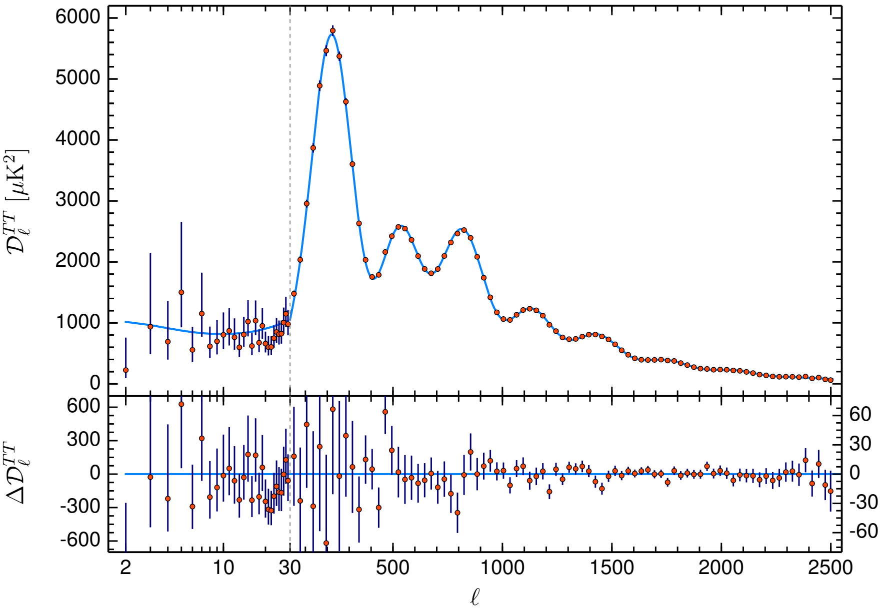

Figure 1.2: *CMB temperature power spectrum [3]*

Baryon acoustic oscillation (BAO), are the longitudinal sound waves, which are generated due to oscillation of baryon and radiation plasma. Due to lack of interaction of DM to photons, it doesn't feel the radiation pressure and hence clumps and provides high gravitational potential where baryons get attracted. Due to presence of photons in plasma, radiation pressure develops and further two countering forces, radiation pressure and gravity makes baryonic plasma oscillate to and fro, in turn generating longitudinal acoustic waves. After the recombination period, photons decouple and stream freely but BAO freezes in, due to no more radiation pressure.

These acoustic waves generated by the baryon-photon plasma, are encoded in the CMB temperature power spectrum. The heights of the peaks in the CMB power spectrum are related to the densities of both baryonic and dark matter. In the CMB power spectrum, the first peak corresponds to this acoustic wave due to the first compression of baryon-photon fluid after recombination epoch and is crucial for estimating the geometry as well as dark energy of our Universe. The second peak corresponds to one compression and one rarefaction of acoustic waves and similarly we get other acoustic peaks in the CMB power spectrum, with the odd and even numbered peaks corresponding to regions of maximum and minimal density during the baryon acoustic oscillations.

The second peak is crucial for estimating the baryon abundance in our Universe. A smaller peak indicates more baryonic matter density. The third peak's height is enhanced by dark matter, as it doesn't interact with photons in the same way as normal matter, allowing it to contribute more to gravitational clumping. In particular, while interaction with photons pushes ordinary (baryonic) matter away from over-dense regions, DM does not, and hence enhances the height of the third peak. The amplitude of the third peak is seen — see Fig. 1.2 — to be higher that the second one which is the indication of availability of high gravitation region generated [5–7] due to the clumping of dark matter.

1.4.2 Lyman alpha and 21 cm spectral lines

Neutral hydrogen absorbs or emits radio waves from transitions between the spin-flip hyperfine levels of the ground state. This emission corresponds to a wavelength of 21 cm and is known as the 21 cm line. As large-scale structures formed, and began to emit radiation (during the re-ionisation epoch), the neutral hydrogen absorbed this light and became ionised. This occurred some time about 100-1000 million years after the Big

Bang. However, since the Universe had considerably expanded at this time, the density of the ionised gas was very low and the Universe was mostly transparent to radiation. The distribution of neutral hydrogen is affected by the presence of dark matter and this is in turn reflected in observations of the red-shifted 21 cm line.

Similarly, neutral hydrogen clouds can affect the spectra from distant quasars. These show up as absorption lines in the Lyman region and are called the Lyman-alpha forest. They probe smaller scale structure than the 21 cm line which are thought to be governed by the distribution of dark matter.

Both the 21 cm and Lyman-alpha lines are sensitive to the scattering and decay of dark matter as well as the thermal evolution of the Universe [8]. Lyman-α forest and 21 cm signal are highly useful in constraining the mass of dark matter in various models, e.g. freeze-in dark matter [9, 10], axion-like particle (ALP) dark matter [11, 12], sterile neutrinos [13, 14], as well as constraining the dark matter velocity distribution in the intergalactic medium [15].

Other evidences on cosmic scale comes from Large scale structure (LSS). LSS of luminous matter in our Universe is not homogeneous. The cause of formation of the large scale structure is matter immune to radiation pressure, i.e., DM. The DM clumps due to gravitational attraction and provides seeds of high gravitational potential region. Luminous matter, due to radiation pressure, do not clump and fall into the high gravity regions provided by DM clumps. The Illustris TNG project and the EAGLE simulations both simulate galaxy (structure) formation in the Universe.

1.4.3 Evidence from Galaxy and Galaxy Clusters

At the scale of galaxy clusters, evidence for dark matter comes from the observation of Fritz Zwicky in 1933 [16], who discovered the presence of extra mass in the Coma galaxy cluster. In order to understand his discovery, we need to know virial theorem. As per the virial theorem, for a system following inverse square law of force, the average kinetic and potential energy are related by

$$2\langle K\rangle = -\langle U\rangle\,, \tag{1.2}$$

For a galaxy cluster with collective velocity dispersion, σ_v having total mass M_{tot}, $\langle K\rangle = (1/2)M_{tot}\sigma_v^2$ and the average potential energy at radius R from the centre of the cluster is $\langle U\rangle = -(3/5)GM_{tot}^2/R$. This gives rise to the velocity dispersion:

$$\sigma_v^2 = \frac{3}{5}\frac{GM_{tot}}{R}\,. \tag{1.3}$$

Coma cluster has about 800 galaxies in it with average mass of $10^9 M_\odot$ and this cluster spans approximately $3\times 10^5 Pc$ so $\sigma_v = 80$ km/s. However, Zwicky observed the velocity dispersion to be around 1000 km/s, implying the presence of extra invisible matter in Coma galaxy cluster, which we now know as the dark matter. From the measured value of the dispersion and using the virial theorem, the mass of the cluster is estimated to be $\sim 1.25\times 10^{14} M_\odot$, which is around 200 times more than the predicted mass [17].

A robust evidence for dark matter at galactic scales comes from the rotation curves of intergalactic objects. Initial efforts in this direction were done by Vera Rubin and Kent Ford [18, 19]. They studied rotation curves for 21 Sc galaxies. The circular velocity,v_c of stars in the galaxy is expected to increase until the edge of the galaxy, after which it is expected to fall, according to Newtonian Gravity, as

$$v_c(r) \propto r^{-1}$$

as a function of the radial distance from the centre of the galaxy.

But studies show that, instead, the rotation curve start to follow asymptotic behavior as in Fig: 1.3, which demands the presence of an extra source of gravity.

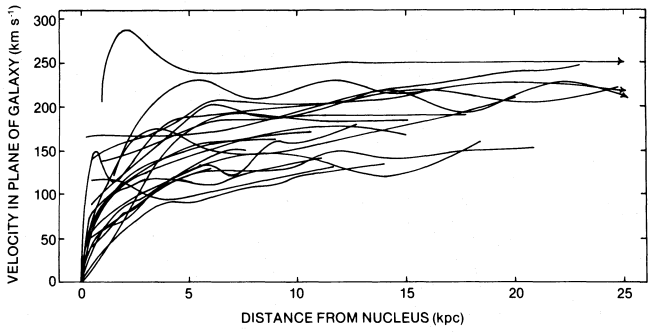

Figure 1.3: *Asymptotic behavior of circular velocity at large distance from the centre [19].*

Other evidence also exists for the presence of dark matter. Gravitational lensing provides strong evidence for dark matter. Here the extent of bending of light around massive objects like galaxy clusters is much greater than the mass of the visible matter (stars, gas, etc.) in those objects. This extra "missing" mass is attributed to the presence of dark matter. When the lensing effect is strong, it can create multiple images or arcs of the background object. This is called strong gravitational lensing and the Bullet Cluster is a very good example.

1.5 Models and Production mechanism of Dark Matter

While there is considerable evidence for the presence of a substantial amount of dark matter in the Universe, it is not clear whether it has a particle-like nature, and if so, what its properties are. Several models exist that extend the SM to include possible dark matter candidates.

The mass of the dark matter can range from 10^{-22} eV in the case of Ultra-light Dark Matter [20] to the order of solar mass ($M_{\odot}$) in the case of Primordial Black Holes (PBH) [21]. Some other candidates of dark matter are WIMP, Axion, ALP (axion like particles), Dark photon and Sterile neutrino; see Fig. 1.4. We briefly discuss a few of the more popular models below, and discuss the model of our choice later.

There are mainly two production mechanisms of dark matter—thermal production or non-

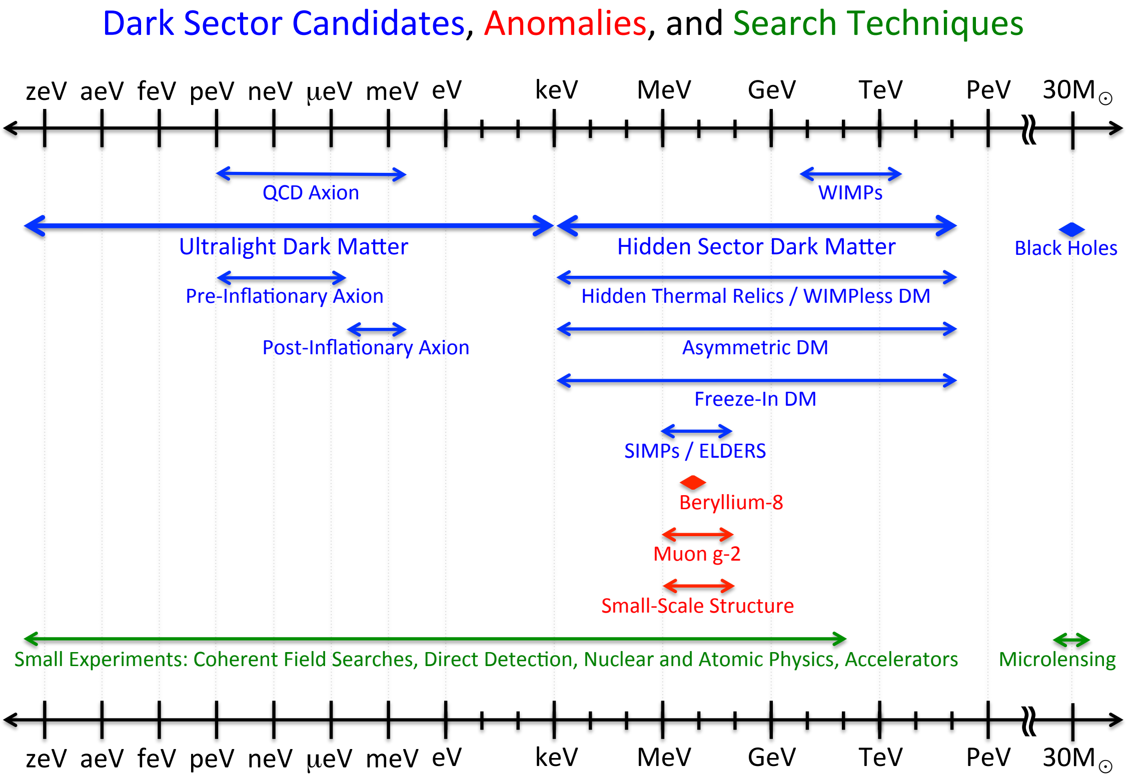

Figure 1.4: *Dark matter candidates with their mass range; Ref: [21]*

thermal production. In thermal production, DM is considered to be in chemical and kinetic equilibrium with the thermal plasma of SM particles. Whereas in non-thermal production mechanism it is considered that DM is never in equilibrium with the thermal plasma of SM particles.

1.5.1 Thermal Production

1.5.1.0.1 Freeze-out mechanism : Here, the DM is considered to be in chemical and kinetic equilibrium with thermal plasma and decoupling of DM takes place when the Hubble expansion rate of the Universe starts dominating over the annihilation rate of the dark matter i.e. $H_0 > \Gamma_{DM}$. One of the widely studied scenarios under this mechanism is the WIMP (Weakly interacting massive particle) scenario, in which dark matter annihilation process $DM + DM \to SM + SM$ is taken into account. WIMP mass is usually taken to be in the range of 10 GeV to 1 TeV [22]. SIMP (Strongly interaction massive particle) is another dark matter scenario which is produced through the freeze-out mechanism. In SIMP scenario, DM are taken to be self interacting. SIMP is a DM number changing process e.g. $DM + DM + DM \rightarrow DM + DM$, in which the DM density freezes-out due to domination of expansion rate of the Universe over the $3 \rightarrow 2$ number changing process. SIMP is considered to be thermally connected to SM particles via very small coupling. The mass of the SIMP particle is taken to be in sub GeV range (1–1000 MeV).

1.5.1.0.2 Elastic Decoupling : In this scenario we assume DM and SM particles to be in thermal equilibrium via elastic scattering ($DM + SM \rightarrow DM + SM$) [23, 24]. Due to expansion of the Universe this scattering rate is insufficient to keep DM and SM in thermal equilibrium and DM decouples from the thermal plasma. Particles studied via this production mechanism are named ELDER (Elastically DEcoupling Relics).

1.5.1.0.3 Cannibal dark matter : This is a self-interacting dark matter number-changing process in which the number of final state particle is less than number of particle in initial state [25–27]. Usually $3 \rightarrow 2$ or $4 \rightarrow 2$ processes are taken into account but the number of particles in the in-state can be more than 4 as well. Self-interaction of dark matter is taken to be much greater that in the case of WIMP. The dark sector is taken to be kinetically and chemically decoupled from standard model but is considered to be in thermal equilibrium with its own species via $n \rightarrow m$ process, for $n > m$. Dark matter particles consumed into the cannibalization causes extra heat of the thermal plasma of dark sector. When the Hubble expansion rate of the Universe becomes more than the cannibalization rate of DM, the number density of cannibal DM becomes fixed. There is a vast mass range, eV to TeV, where cannibal DM can be looked for [27, 28]

1.5.2 Non-thermal production of dark matter

1.5.2.0.1 Freeze-in : In freeze-in mechanism we assume DM to be never in equilibrium with the SM particle [29]. Interaction between DM and SM particles is assumed to be feeble and the initial abundance of DM compared to SM particles is assumed to be very small. As the Universe expands and Hubble rate dominates over production rate of the DM candidate, DM number density starts freezing. A comparison of freeze-in and freeze-out scenario is presented in Fig. 1.5.

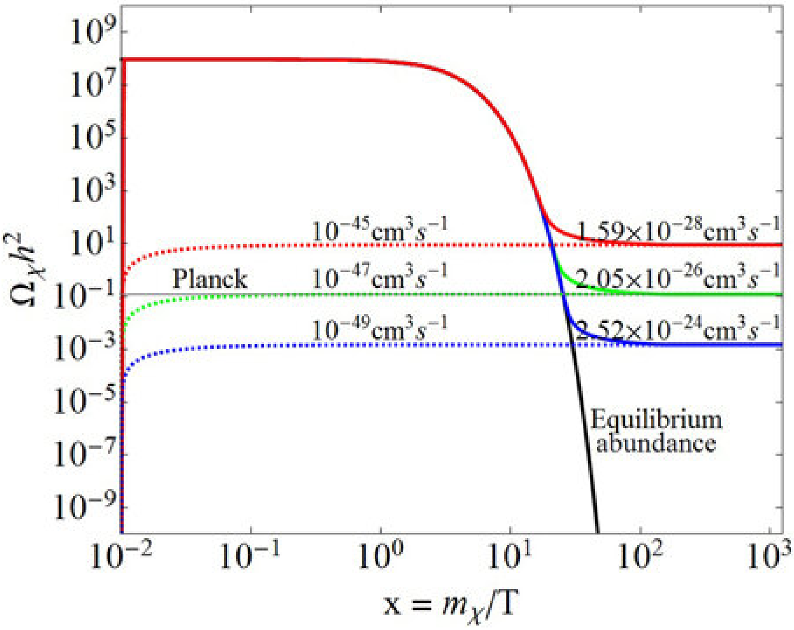

Figure 1.5: *Possible freeze-in and freeze-out scenarios [30]. The dotted lines show the slow increase of DM reaching constant values as a function of the DM mass to temperature ratio. The solid lines show the freeze-out scenario for different values of the DM annihilation/production cross section.*

1.5.2.0.2 Schwinger Mechanism : In this mechanism, DM is assumed to be produced from vacuum. In analogy to $U(1)$ gauge symmetry of QED, the dark gauge field $U(1)_D$ is taken to be the symmetry of DM which is generated from vacuum analogous to pair production process in SM [31]. Production of such DM can be done without them being thermally connected to SM. [4]

---

[4] Fermion and Scalar charged under $U(1)_D$ are usually taken to be DM but gauge field of this symmetry can be taken to be DM candidate too.

1.5.2.0.3 Axions and ALPs : Axion are pseudo-scalar particles, initially introduced to solve the strong CP problem in the QCD Lagrangian [32–34]; the relevant part of the Lagrangian can be expressed in terms of the gluon field strength tensor and its dual:

$$\mathcal{L} \supset \theta \frac{g^2}{32\pi^2} G_a^{\mu\nu} \tilde{G}^a_{\mu\nu} = \mathcal{L}_\theta \, , \tag{1.4}$$

CP violation is observed in the weak interaction but not in the strong interaction yet. Experimental inference comes from the upper bound of electric dipole moment (eDM) of neutron , $|d_n| \leq 10^{-26} e$ cm, which is theoretically calculated to be of the order $10^{-13} e$ cm. Introducing a pseudo-scalar axion field ‘a' following extra U_1 symmetry, called Peccei Quinn symmetry (U_{PQ}) and new coupling ‘f_a' in Eq. 1.4 resolves the problem, via tuning ‘f_a' . These axions are considered to be potential candidates for dark matter in the $1 \mu eV$ to $100 \mu eV$ range. Inspired by the QCD axion, other axion like particles (ALPs) are studied and constrained [35] for dark matter which can have masses ranging from 10^{-22} eV to GeV.

There are many other exotic models including Axion Misalignment, Sterile Neutrino production, Asymmetric Dark matter, Primordial Black Holes (PBH), Gravitational Production, Afleck-Dine Mechanism, etc. See Ref. [1] for a review.

1.5.3 Detection techniques of dark matter

Although this thesis does not involve DM detection, we present a list for the sake of completeness. There are three class of detection technique for dark matter: Direct detection, Indirect detection, and collider searches; see Fig. 1.6. So far, only limits have been placed on the nature of DM, its mass, and coupling to SM particles.

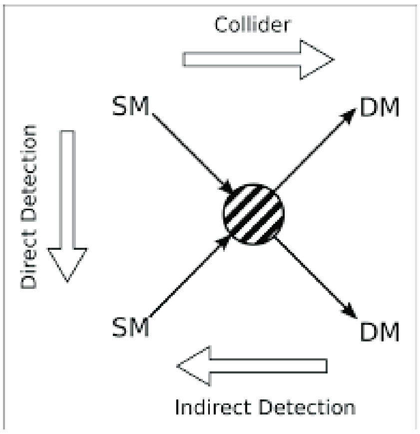

Figure 1.6: *Schematic for detection mechanisms for dark matter [36].*

1.5.4 Indirect detection

In the indirect detection techniques for dark matter, detectors search for the excess of SM high energy particles coming from nearby stellar objects like galaxies, dwarf spheroidal galaxies etc., which can be the outcome of annihilation of dark matter particles [37–40].

In particular there are searches for dark matter through high energy cosmic rays by AMS [41, 42], HAWC [43], AUGER [44–46] and other collaborations. Super-K [47, 48], Ice Cube [49] search for dark matter through excess of SM neutrinos. The Planck [50] and some other telescopes search for dark matter through microwave radiation (CMB). Some indirect detection comes from the X-ray observatories e.g Chandra X-ray observatory, which observe X-ray from gas in Galaxy Cluster. With the help of gravitational lensing, the need for extra mass is confirmed in galaxy clusters. Fermi-LAT looks for the excess of γ-rays from the center of the Milky Way galaxy [51], Galaxy clusters, Dwarf Spheroidal Galaxies [52, 53].DM searches through gamma ray in these astronomical objects are also done in HESS [5] , which is a ground based telescope array. [6]

---

[5] arXiv : 2508.20229

[6] An upcoming successor to HESS is CTA (Cherenkov Telescope Array)

1.5.5 Direct detection

In the direct detection experiments, one looks for recoil of nucleus or SM particle (mainly e^-) due to interaction with dark matter in our galaxy, Milky Way [54–56]. In direct detection experiments, the nuclear recoil rate, nuclear recoil energy, and nuclear recoil direction are measured. Direct detection experiments are mainly designed for detecting the WIMP kind of dark matter via nuclear recoil and for some LDM (Light Dark Matter) via electron recoil. Some of the experiments constraining WIMP and LDM are XENONnT [57–59]. LZ (LUX-ZEPLIN) [60], DarkSide [61, 62], SuperCDMS [63–65], CRESST [66, 67]. DAMA/LIBRA [68] and PICO[69] ADMX [70] looks for ALP (Axion-like particles). PandaX has set constraints for WIMP [71], LDM [72, 73] and ALP [74, 75].

1.5.6 Collider searches

Collider experiments mainly search for dark matter through the missing energy and momentum from DM production after collision of SM particles in collider [22, 76, 77]. If there is a production of DM in detectors, it will not interact with the detector material and the only way to know about the production of such a particle is through the missing energy or momenta. Experiments in this direction are ATLAS [78–80], CMS[81–83] , LHCb[84], FASER[85, 86], SND@LHC[87], MoEDAL-MAPP[88], NA64[89–91] etc. These experiments look for missing transverse momentum in mono-X event (e.g. $pp \rightarrow \chi\overline{\chi} + X$) where X can be single SM particle or a jet, and χ represents dark matter particle. Some future facilities in this direction are HL-LHC, FCC, CEPC,ILC, MuCol, which are proposed and will be looking for dark matter.

1.6 Motivation of the study

The magnetic moment of an electron is most precisely measured quantity in physics till date. Its current value is [92] $-9.2847646917(29) \times 10^{-24}$ J T^{-1}. Its theoretical prediction comes from quantum electrodynamics. In the era of precision physics, physical quantities are getting measured with increasing accuracy. One of the physical quantity getting precisely measured is the relic abundance of dark matter.

In the early Universe, dark matter decouples from the thermal plasma at a temperature depending on the exact mechanism of its interaction. For instance, in the freeze-out scenario, dark matter remains in equilibrium with SM particles (ordinary or baryonic matter) through scattering and decay processes such as $\chi f \to \chi f$ and $\chi\overline{\chi} \leftrightarrow f\overline{f}$. As the Universe cools, the dark matter interaction rate falls below the expansion rate of the Universe at which point the dark matter falls out of equilibrium and its density "freezes out" to a constant value which is the presently observed relic density. For typical DM masses freeze-out occurs in the range $m_\chi/10 \leq T \leq m_\chi/20$. In a typical freeze-in scenario, DM interacts very weakly with SM particles. Moreover, their initial density is very small so that the present relic density is achieved by production of DM via SM interactions. For these scenarios, the DM mass is in the range, $m_\chi \leq T \leq m_\chi/10$.

The value of the DM relic density from several observations currently is $\Omega_c = 0.265(7)$ and is therefore very precisely known. Various models of DM have been used to predict this density. Theoretically, the dark matter relic abundance is obtained by solving the Boltzmann equation which evolves the DM density over time. The resulting relic density n_χ depends on the expansion rate of the Universe as well as the interaction rate of DM, accounting for its production/loss. In the freeze-out scenario, we have

$$\frac{dn_\chi}{dt} + 3Hn_\chi = -\langle \sigma_{\chi\bar{\chi}\to f\bar{f}}\, v_{rel} \rangle_T \left(n_\chi\, n_{\bar{\chi}} n_\chi^{eq}\, n_{\bar{\chi}}^{eq} \right) . \tag{1.5}$$

Here the second term accounts for the expansion of the Universe while the term containing the thermal average of the annihilation cross section, $\sigma_{\chi\bar{\chi}\to f\bar{f}}$, codes for the collision term, where v_{rel} is the relative velocity. Here n_i^{eq} refers to the equilibrium density of the species i. The Boltzmann equation can be recast in terms of the yield, $Y = n/s$ where s is the entropy density, and the ratio $x = m_\chi/T$. The initial condition to solve this equation is that the DM particles are in thermal equilibrium at early times ($x \ll 1$). As the temperature falls below $T \sim m_\chi$, the production of χ will be suppressed exponentially due to the presence of the Boltzmann number density factor. As the Universe further cools, the interaction rate for both the forward and backward processes drops, and the dark matter falls out of equilibrium. The required relic density $\Omega_C h^2 = 0.12$ is obtained if $\langle \sigma v_{rel} \rangle_T \sim 1$ pb, which indicates a DM mass of about 100-1000 GeV.

In the freeze-in scenario, the DM is not in thermal equilibrium and couples weakly to the SM particles; hence the term containing n_i^{eq} in the RHS of Eq. 1.5 can be ignored. Again, the forward process is Boltzmann suppressed when the temperature falls below the mass of χ, and production of DM then stops (since the backward process was anyway negligible). Here the initial condition is that the initial DM yield at the reheating scale, just after inflation, $Y(x_{RH}) = 0$.

The model dependence in either case arises from the calculation of the collision term involving scattering and annihilation cross sections for DM. (Here we ignore decay). It is obvious that, the larger the cross section, the more the annihilation and smaller the DM relic density. The thermal average is given by

$$\langle \sigma_{\chi\bar{\chi}\to ij} v_{rel} \rangle_T = \frac{1}{n_\chi^{eq} n_{\bar{\chi}}^{eq}} \int \frac{d^3\vec{p}_\chi}{(2\pi)^3} \frac{d^3\vec{p}_{\bar{\chi}}}{(2\pi)^3} f_\chi^{eq} f_{\bar{\chi}}^{eq} \, \sigma_{\chi\bar{\chi}\to ij} \, v_{rel} \, , \tag{1.6}$$

where $f_\chi = n_\chi / n_\chi^{eq} \times f_\chi^{eq}$, and the number density is expressed in terms of the phase space distribution function $f(p)$ as

$$n_i(t) = h_i \int \frac{d^3\vec{p}_\chi}{(2\pi)^3} \, f_i(p) \, , \tag{1.7}$$

where h_i represents the number of internal degrees of freedom of the i^{th} particle. The more precisely the dark matter annihilation cross section is computed, the more accurate is the prediction of the relic abundance of dark matter. In addition, note that the thermal average of the *temperature independent* cross section is taken in Eq. 1.6. For the sake of consistency, it is important to compute the cross section in a thermal field theory of DM. In this case, the DM annihilation cross section further gets finite temperature corrections which can be important. These corrections are to be incorporated along with the zero-temperature pure quantum correction to the annihilation cross section since the measurement of relic abundance of dark matter is getting increasingly precise, with elevated state-of-art experimental facilities.

This therefore brings us to the main motivation of this thesis. In order to calculate the finite temperature corrections to DM annihilation cross sections, one has to implement techniques of thermal field theory.

Thermal field theory (TFT) is a generalized framework of quantum field theory which incorporates *statistical fluctuations* alongside with the *quantum fluctuations*.

For our study we take a generic MSSM inspired model with Yukawa coupling [93, 94] described by a Lagrangian of the form

$$\begin{aligned}\mathcal{L} = &-\frac{1}{4}F^{\mu\nu}F_{\mu\nu} + \bar{f}(i\not{D} - m_f)f + \frac{1}{2}\bar{\chi}(i\not{\partial} - m_\chi)\chi \\ &+ (D_\mu\phi)^\dagger(D_\mu\phi) - m_\phi^2\phi^\dagger\phi + (\lambda\bar{\chi}P_L f^- \phi^+ + h.c.)\,. \qquad (1.8)\end{aligned}$$

Here the dark matter candidate is an $SU(2) \times U(1)$ singlet Majorana [7] fermion χ which interacts with SM doublet fermions, $f = (f^0, f^-)^T$, via scalar partners $\phi = (\phi^+, \phi^0)^T$ through a Yukawa coupling, λ. The calculations are performed after electro-weak symmetry breaking, so that the W and Z are heavy and their contributions to the higher order

---

[7] We also included the possibility where DM is Dirac type and which will slightly modify the kinetic term and the mass term for the Dirac DM. Kinetic and mass term in the main Lagrangian (for the Majorana case) will be be modified by the $\overline{\chi}(i\not{\partial} - m_\chi)\chi$ in case of Dirac DM.

corrections can be safely ignored. Hence our study involves a calculation of thermal corrections to the DM annihilation cross section in a thermal bath of SM fermions, photons, and (beyond SM) scalars and dark matter particles.

The present-day experimental determination of the relic abundance of DM is now so precise that these model-based cross sections need to be calculated to next-to-leading order (NLO); for example, the cross sections in various models have been calculated in Refs. [95–101]. Additionally, *thermal corrections* to these cross sections (or decay rates) can become important in the early Universe [94, 102–107], in Quark Gluon Plasma [108]. Some of the processes have also been resummed [109–111]. Other work [112] has also discussed in detail the limitations of the Boltzmann equation.

There are few papers [94, 102] where thermal corrections to cross sections or decay rates have been calculated. In particular, Beneke et al. [94] computed the thermal NLO corrections to the dark matter annihilation cross section in a generic DM model where Majorana dark matter particles interact with SM fermions through charged scalars where they showed that the leading s-wave (non-relativistic) contribution to the thermal cross section for the dark matter annihilation to SM fermion pairs via scalars, *viz.*, $\chi\chi \to f\overline{f}$, of order $O(\alpha T^2)$, vanishes in the massless fermion limit, where T is the temperature of the heat bath in which the interaction occurs.

Our core motive here is to obtain the finite temperature correction to annihilation cross section for dark matter in our model of interest in Eq. 1.8. We will be presenting finite temperature correction to DM annihilation cross section up-to leading order in the QED coupling constant $O(\alpha)$ for DM annihilation process $\chi\overline{\chi} \to f\overline{f}$ and $\chi\overline{\chi} \to f\overline{f}(\gamma)$, where γ codes for real emission and absorption of photon from the heat bath by electrically charged particles.

In the next chapter, we set up the required technology of thermal field theory to perform this computation. At finite temperature, infra-red (IR) divergences are much more severe than at zero temperature (linear rather than log divergence). Hence we use the generalized Grammer and Yennie technique in TFT in order to deal with the IR divergences. In Chapter 3, we discuss details of this technique, as applicable to thermal fields. The expert reader can directly go to Chapter 4 from where the actual calculation of the thermal corrections begins.

Chapter 2

Quantum field theory at finite temperature

In this chapter, we will outline the details of thermal field theory in the real time formulation. The Feynman rules that we list here will be used in Chapters 4 and 5 to calculate the thermal corrections to the dark matter annihilation cross sections at NLO. The key aspect of this formulation is the doubling of fields so that all propagators take on a 2×2 matrix form. Each component of the propagators, and the corresponding phase space factors, can then be represented as a linear sum of temperature-independent and temperature-dependent parts, with the $(1, 1)$ element of the temperature-independent part matching the corresponding zero-temperature propagator for that particle. A detailed review of the field can be found in Refs. [113, 114].

Quantum field theory at finite (non-zero) temperature uses a generalized framework (thermal field theory) to obtain thermal corrections to physical measurables of the system. In our study we will be obtaining the finite temperature corrections to the dark matter annihilation cross section using thermal field theory. Broadly there are three main formalisms of thermal field theory.

- Imaginary time formalism, also known as Matsubara Formalism [115],

- Thermo-field Dynamics, also known as Umezawa TFD [116], which treats time and temperature on an equal footing, paving the way to a more general class of real time thermal field theories,

- Real time formalism, also known as Closed-Time-Path formalism or Schwinger-Keldysh formalism [117, 118].

We focus here on the real time formulation of thermal field theory.

2.1 Real Time formalism of thermal field theory

We start with the example of neutral scalar fields. In the Heisenberg picture, we have

$$\hat{\phi}(x) = e^{it\hat{H}}\hat{\phi}(0)e^{-it\hat{H}} \, . \tag{2.1}$$

Of interest is the N-point Green function, standardly obtained from functional differentiation of the generating functional $Z_C(\beta; j)$ with respect to the sources $j(x)$:

$$G_C(x_1, \cdots, x_N) = \frac{1}{Z(\beta)} \left. \frac{\delta^N Z_C(\beta; j)}{i\delta j(x) \cdots i\delta j(x_N)} \right|_{j=0} \, , \tag{2.2}$$

with

$$Z_C(\beta; j) = \mathrm{Tr}\left[e^{-\beta\hat{H}} T_C \exp\left(i \int_C \mathrm{d}^4 x \, j(x)\hat{\phi}(x) \right) \right] \, , \tag{2.3}$$

where the complex time path C will be defined later, and

$$Z_C(\beta; j = 0) = Z(\beta) = \mathrm{Tr} \exp\left(-\beta\hat{H} \right) \, , \tag{2.4}$$

is the usual zero-temperature partition function. The thermal average of any operator is then defined as

$$\hat{A} = \frac{1}{Z(\beta)}\,\mathrm{Tr}\left(e^{-\beta\hat{H}}\hat{A}\right) . \tag{2.5}$$

The states $\hat{\phi}$ can be used to express the functional integration measure $[\mathcal{D}\phi]$ so that the trace can be re-written as

$$Z[j] = \int [\mathcal{D}\phi']\langle\phi';t_{in}|e^{-\beta\hat{H}}\;T_C \exp\left[i\int_C \mathrm{d}^4x\, j(x)\hat{\phi}(x)\right]|\phi';t_{in}\rangle . \tag{2.6}$$

From Eq. 2.1, we have

$$Z[j] = \int [\mathcal{D}\phi']\langle\phi';t-i\beta|\;T_C \exp\left[i\int_C \mathrm{d}^4x\, j(x)\hat{\phi}(x)\right]|\phi';t_{in}\rangle . \tag{2.7}$$

Since the generating functional is defined as a trace, the initial and final states must be taken at equal times; this gives us the periodicity condition

$$\phi(t_{in}-i\beta,\mathbf{x}) = \pm\phi(t_{in}\mathbf{x}) , \tag{2.8}$$

where the $(+,-)$ signs refer to bosonic and fermionic fields respectively. This is known as the Kubo-Martin-Schwinger (KMS) condition [117, 119] on the fields. Hence the fields are defined over a *closed* time path where the temperature ($\beta = 1/T$) forms the imaginary time axis. The time-ordered propagator on this time path can be defined as

$$\begin{aligned} \mathcal{D}_C(x,x') &= \theta_C(t-t')\mathcal{D}^{>}_C(x,x') + \theta_c(t'-t)\mathcal{D}^{<}_C(x,x') , \\ \text{with } \mathcal{D}^{>}_C(x,x') &= \langle\hat{\phi}(x)\hat{\phi}(x')\rangle_\beta ; \\ \mathcal{D}^{<}_C(x,x') &= \langle\hat{\phi}(x')\hat{\phi}(x)\rangle_\beta = \mathcal{D}^{>}_C(x',x) , \end{aligned} \tag{2.9}$$

where θ_C is suitably defined on the time path C.

2.2 Choice of Contour

We know that the contour C must contain the real time axis, in order to formulate scattering problems. In addition, it must be such that it satisfies the boundary condition in Eq. 2.8. In the real-time formulation of thermal field theories [120–123], the integration in the complex time plane is then defined over a special path shown in Fig. 2.1, from an initial time, t_i to a final time, $t_i - i\beta$, where β is the inverse temperature of the heat bath, $\beta = 1/T$.

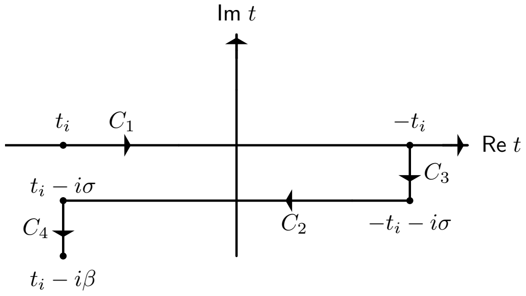

Figure 2.1: *The time path for real time formulation of thermal field theories in the complex t plane, where the y axis corresponds to* $\mathrm{Im}\, t = \beta$*, the inverse temperature, and* $\sigma \in [0, \beta]$.

We choose a specific time path C as follows:

1. Time path C has the initial real value t_i which is taken to be in distant past ($t_i \to -\infty$); further, it is taken along the real axis up to some large positive value $-t_i$. This part of the time path is denoted by C_1 in Fig. 2.1.

2. Then we follow the path from $-t_i$ to $-t_i - i\sigma$, where σ is taken in the interval $[0, \beta]$. This part of the path is indicated by C_3.

3. Next part of the time path C is the straight line taken from $-t_i - i\sigma$ to $t_i - i\sigma$ and is indicated by C_2.

4. The final segment of the contour C is the line starting from $t_i - i\sigma$ and terminating at $t_i - i\beta$. This segment is denoted by C_4.

This path is also known to be Closed Time Path (CTP) or interchangeably Schwinger-Keldysh path due to its developers. We further rewrite the generating functional $\mathcal{Z}_C(\beta; j)$ as products of the free generating functional $\mathcal{Z}^F_C(\beta; j)$ and an interaction term to obtain a perturbation expansion as follows.

$$\mathcal{Z}_C(\beta; j) = \exp\left(- i \int_C d^4x\, \mathcal{V}\left(\frac{\delta}{i\delta j(x)}\right)\right) \mathcal{Z}^F_C(\beta; j) \,, \tag{2.10}$$

where $\mathcal{V}$ describes the potential under which the field interacts, and the free generating functional $\mathcal{Z}^F_C(\beta; j)$ is,

$$\mathcal{Z}^F_C(\beta; j) = \mathcal{N} \exp\left[- \frac{1}{2} \int_C d^4x \int_C d^4x'\, j(x) \mathcal{D}^F_C(x - x') j(x') \right] . \tag{2.11}$$

The correlator, $\mathcal{D}^F_C(x - x')$ on this path is

$$\mathcal{D}^F_C(x - x') = \theta_C(t - t')\mathcal{D}^{>F}_C(x - x') + \theta_C(t' - t)\mathcal{D}^{<F}_C(x - x') \,. \tag{2.12}$$

For systems in thermal equilibrium, it has been shown [124] that the generating functional factorises as

$$\mathcal{Z}^F_C(\beta; j) = \mathcal{N}_1 \mathcal{Z}^F_{C_{12}}(\beta; j) \mathcal{Z}^F_{C_{34}}(\beta; j) \,. \tag{2.13}$$

Here $C_{1,2}$ ($C_{3,4}$) refer to the paths $C_1 \cup C_2$ ($C_3 \cup C_4$). This factorization of generating functional is known to be consistent for the calculations where we have processes with at least one external line in the Feynman graph. Correlators can be obtained from $\mathcal{Z}^F_{C_{12}}$ only and contributions from $\mathcal{Z}^F_{C_{34}}(\beta; j)$ can be absorbed in the normalization coefficient. Then the effective free generating functional is written as

$$\mathcal{Z}^F_C(\beta; j) = \mathcal{N}_2 \exp\left[- \frac{1}{2} \int_{C_{12}} d^4x \int_{C_{12}} d^4x'\, j(x) \mathcal{D}^F_C(x - x') j(x') \right] . \tag{2.14}$$

2.3 The scalar field thermal propagator

For convenience we take $-\infty < x^0(= t), x'^0(= t') < \infty$. The source $j(x)$ is taken along the path C and the relevant part of $j(x)$ in different parts of C are labeled according to the relevant segment of C. For C_1 and C_2 we take j_1 and j_2 respectively as

$$j_1(x) = j(t, \mathbf{x}) \ ; \ j_1(x) = j(t - i\sigma, \mathbf{x}) \ . \tag{2.15}$$

Generalising the functional derivative as

$$\frac{\delta j_a(x)}{\delta j_b(x')} = \delta_{a,b}\delta^{(4)}(x - x') \ , \tag{2.16}$$

we see that $j_a, a = 1, 2$ "live" on different parts of the contour, C, so that

$$\mathcal{Z}_C^F(\beta; j) = \mathcal{N}_2 \exp\Big[-\frac{1}{2}\int_{-\infty}^{\infty} d^4x \int_{-\infty}^{\infty} d^4x' \, j_a(x)\mathcal{D}_{ab}^F(x - x') j_b(x')\Big] \ . \tag{2.17}$$

Here we notice that the degrees of freedom of field ϕ have doubled: we have both fields ϕ_1 and ϕ_2. The extra field ϕ_2 is interpreted as a ghost field since it does not occur on external lines. Only the ϕ_1 fields occur on external lines, but the Feynman rules get modified since the propagators have off-diagonal elements, as we see below.

In other words, the real-time propagator has four components which can be expressed as a 2×2 matrix. We can then obtain the free propagator in momentum space:

$$\begin{aligned}
\mathcal{D}_{11}^F(k) &= \frac{i}{k^2 - m^2 + i\eta} + n_B(|k^0|)2\pi\delta(k^2 - m^2) \\
\mathcal{D}_{22}^F(k) &= (\mathcal{D}_{11}^F(k))^* \\
\mathcal{D}_{12}^F(k) &= e^{\sigma k^0}[n_B(|k^0|) + \theta(-k_0)]2\pi\delta(k^2 - m^2) \\
\mathcal{D}_{21}^F(k) &= e^{-\sigma k^0}[n_B(|k^0|) + \theta(k^0)]2\pi\delta(k^2 - m^2) \ ,
\end{aligned} \tag{2.18}$$

where

$$n_B(|k^0|) = \frac{1}{e^{\beta|k^0|} - 1} , \tag{2.19}$$

is the Bose distribution function.

Here the propagators $\mathcal{D}^F_{12}$ and $\mathcal{D}^F_{21}$ depend on σ which can be chosen appropriately for specific calculations. We use the symmetric choice $\sigma = \beta/2$. The propagator for fermion and photon fields can be similarly obtained. We now collect the Feynman rules for the cases of interest.

2.4 Feynman rules in thermal field theory

The scalar propagator is given by

$$iS^{t_a,t_b}_{\text{scalar}}(p,m) = \begin{pmatrix} \Delta(p) & 0 \\ 0 & \Delta^*(p) \end{pmatrix} + 2\pi\delta(p^2 - m^2)n_{\text{B}}(|p^0|)\begin{pmatrix} 1 & e^{|p^0|/(2T)} \\ e^{|p^0|/(2T)} & 1 \end{pmatrix} , \tag{2.20}$$

where $\Delta(p) = i/(p^2 - m^2 + i\epsilon)$, and t_a, t_b $(= 1, 2)$ refer to the field's thermal type. It can be seen that the scalar propagator is a sum of two terms, one which is *temperature-independent* and the other which contains the explicitly thermal dependence which we call the thermal part. Only the *thermal* parts can convert type-1 to type-2 (ghost) fields, and vice versa; note that these contribute only on mass-shell.

The photon propagator corresponding to a momentum k is given in the Feynman gauge by

$$i\mathcal{D}^{t_a,t_b}_{\mu\nu}(k) = -g_{\mu\nu} iD^{t_a,t_b}(k) = -g_{\mu\nu}\, iS^{t_a,t_b}_{\text{scalar}}(k,0) , \tag{2.21}$$

while the fermion propagator at zero chemical potential is given by

$$
\begin{aligned}
iS^{t_a,t_b}_{\text{fermion}}(p,m) &= \begin{pmatrix} S & 0 \\ 0 & S^* \end{pmatrix} - 2\pi S'\delta(p^2-m^2)n_{\text{F}}(|p^0|)\begin{pmatrix} 1 & \epsilon(p_0)e^{|p^0|/(2T)} \\ -\epsilon(p_0)e^{|p^0|/(2T)} & 1 \end{pmatrix}, \\
&\equiv (\not{p}+m)\begin{pmatrix} F^{-1}_p & G^{-1}_p \\ -G^{-1}_p & F^{*-1}_p \end{pmatrix}, \\
&\equiv (\not{p}+m)\overline{S}^{t_a,t_b}(p,m)\,, \qquad (2.22)
\end{aligned}
$$

where $S = i/(\not{p} - m + i\epsilon)$, and $S' = (\not{p} + m)$. The fermion propagator is proportional to $(\not{p} + m)$, just as at $T = 0$, and the number operator for fermions is given by

$$n_F(|k^0|) = \frac{1}{e^{\beta|k^0|} + 1}\,. \qquad (2.23)$$

It can be seen that all propagators can be expressed as a linear sum of temperature-independent and temperature-dependent parts, with the $(1, 1)$ elements the same as the corresponding zero temperature expressions.

The fermion–photon vertex factor is given by $(-ie\gamma_\mu)(-1)^{t_\mu+1}$, where $t_\mu = 1, 2$ for the type-1 and type-2 vertices. The scalar–photon vertex factor is $[-ie(p_\mu + p'_\mu)](-1)^{t_\mu+1}$ where p_μ (p'_μ) is the 4-momentum of the scalar entering (leaving) the vertex, while the 2-scalar–2-photon *seagull* vertex factor (see Fig. 2.2) is $[+2ie^2 g_{\mu\nu}](-1)^{t_\mu+1}$ (the factor '2' is dropped for a *tadpole* vertex). All fields at a vertex are of the same type, and all external fields are of type-1.

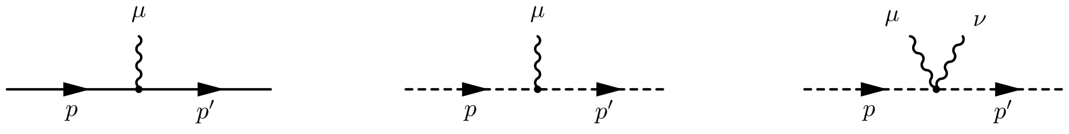

a. Fermion-Photon Vertex b. Scalar-Photon Vertex c. Seagull Vertex

Figure 2.2: *Allowed vertices for fermion–photon and scalar–photon interactions.*

The DM-scalar-fermion vertex factor is $i\lambda P_L$; for details on Feynman rules for Majorana particles at zero temperature, see Ref. [125]. An overall negative sign applies as usual to the type-2 DM vertex.

2.4.1 Some identities at finite temperature

Various identities useful for fermions are given in Ref. [126] and are reproduced here for completeness. Note that Eqs. 2.20, 2.21 and 2.22 lead to

$$(\not{p} - m)\; iS_p^{t_a,t_b} = i(-1)^{t_a+1}\delta_{t_a,t_b}\ , \tag{2.24}$$

where we have used the compressed notation, $iS^{t_a,t_b}(p,m) \equiv iS_p^{t_a,t_b}$.

Consider the insertion of the μ vertex of the additional virtual photon with momentum k between vertices μ_{q+1} and μ_q on the p' fermion leg; see Fig. 3.2. The momentum of the photon at the vertex μ_q is l_q, with Lorentz index μ_q, and thermal type-index t_q. Hence the momentum of the fermion leg to the left of the vertex μ_q is $p' + \sum_{i=1}^{q} l_i$ which we denote as $p' + \sum_q$. Using Eq. 2.24, we have,

$$\overset{t_q,t_\mu}{\underset{p'+\sum\limits_q}{S}}\,\not{k}\,\overset{t_\mu,t_{q+1}}{\underset{p'+\sum\limits_q+k}{S}} = (-1)^{t_\mu+1}\left[\overset{t_q,t_{q+1}}{\underset{p'+\sum\limits_q}{S}}\delta_{t_\mu,t_{q+1}} - \overset{t_q,t_{q+1}}{\underset{p'+\sum\limits_q+k}{S}}\delta_{t_\mu,t_q}\right]. \tag{2.25}$$

If the photon vertex is inserted to the right of the vertex labelled ‘1’ on the fermion leg with momentum p', we have,

$$\overline{u}(p')\not{k}\overset{t_\mu,t_1}{\underset{p'+k}{S}} = \overline{u}(p')(-1)^{t_\mu+1}\delta_{t_\mu,t_1}\ , \tag{2.26}$$

since $\not{p}'u(p') = mu(p')$. Similar relations hold for the insertion of of the virtual K photon at a vertex ν on the (anti-)fermion p leg since $\not{p}\,u(p) = m\,u(p)$ as well.

2.5 Phase space integrals

In thermal field theory apart from the propagator, phase space integrals also get thermal modifications. At finite temperature there are processes with absorption of particles[1] in addition to emission in a scattering process. Consider the dark matter annihilation process $\chi\overline{\chi} \to f\overline{f}(\gamma)$ where (γ) indicates that the photon can be emitted into, or absorbed from the heat bath.

The phase space for photons in thermal field theory will be modified as follows:

$$\begin{aligned}\int \mathrm{d}P_k &\equiv \int \frac{\mathrm{d}^4k}{(2\pi)^4} 2\pi\delta(k^2)\left[\theta(k^0)(1+n_B(|k^0|)) + \theta(-k^0)n_B(|k^0|)\right] , \\ &= \int \frac{\mathrm{d}^4k}{(2\pi)^4}\left(2\pi\delta(k^2)\right)\left[\theta(k^0) + n_B(|k^0|)\right] . \end{aligned} \tag{2.27}$$

Here the term proportional to $n_B(|k^0|) + 1$ is due to emission of photons into the heat bath whereas the term proportional to $n_B(|k^0|)$ is due to absorption of photons into the heat bath.

The phase space integral for fermion/antifermion also gets modified as

$$dP_p = \int \frac{\mathrm{d}^4p}{(2\pi)^4}\left(2\pi\delta(p^2 - m_p^2)\right)\left[\theta(p^0) - n_F(|p^0|)\right] . \tag{2.28}$$

Hence the thermal factor reduces the available phase space for fermions. Since external particles can only be of type-1, an application of the Cutkosky rules show that the definition of the phase space matches (with appropriate cuts) the definition of the (1, 1) element of the corresponding propagators given in Eqs. 2.20, 2.21 and 2.22.

The impact of the presence of the Bose distribution function in the photon phase space and the propagator is deep: in the low energy limit, the fermionic number operator,

$$n_{\mathrm{F}}(|p^0|) \equiv \frac{1}{\exp\{|p^0|/T\} + 1} \overset{p^0\to 0}{\longrightarrow} \frac{1}{2} , \tag{2.29}$$

---

[1] Only emission processes are available in quantum field theory at zero temperature.

is well-defined in the soft limit; however, the bosonic number operator contributes an additional power of k^0 in the denominator to the photon propagator in the soft limit:

$$n_{\rm B}(|k^0|) \equiv \frac{1}{\exp\{|k^0|/T\} - 1} \xrightarrow{k^0 \to 0} \frac{T}{|k^0|} \,, \tag{2.30}$$

so that the leading IR divergence in the finite temperature part is linear rather than logarithmic as was the case at zero temperature. (The cancellation of IR divergences in thermal field theories with photons thus involves cancellation of the leading linear divergence as well as the logarithmic sub-divergence.) We will demonstrate the cancellation of these divergences in Chapter 6.

Note that there are no additional ultra-violet (UV) divergences associated with the thermal parts because of the presence of the same number operators that act like a UV cut-off at large energies/momenta.

We will use these Feynman rules to compute the thermal corrections at NLO to the dark matter annihilation cross sections in the next chapters. Before we begin this calculation, we briefly describe, in the next chapter, the Grammer and Yennie technique that we have used to isolate these IR divergences.

Chapter 3

Infra-red divergences: Grammer and Yennie technique

In the calculation of higher order corrections to tree level processes in QED, we encounter ultra-violet (UV), Infra-red (IR) and collinear divergences. UV divergences are taken care by regularization techniques in QFT at $T = 0$. There are no additional UV divergences in finite temperature field theory due to the presence of the number operator, Eqs. 2.19, 2.23, but there are additional IR and collinear divergences. In this chapter we will be discussing a crucial technique, the Grammer and Yennie technique for dealing with the IR divergences. We first discuss a simple example at $T = 0$ and demonstrate the separation of IR divergent and IR finite pieces in an NLO process with QED vertex. Then we will discuss the cancellation of IR divergences with the Grammer and Yennie technique in the finite temperature field theory. We will apply this technique to the calculation of thermal corrections to the dark matter annihilation cross sections in Chapters 4 and 5.

3.1 Separation of IR divergent and IR safe parts at $T = 0$

We take a simple case for the process $e\gamma^* \to e$ for demonstration of Grammer and Yennie technique at $T = 0$; see Fig. 3.1 and explore its IR behavior. We will see that the soft IR divergence arises when the virtual photon momentum is soft.

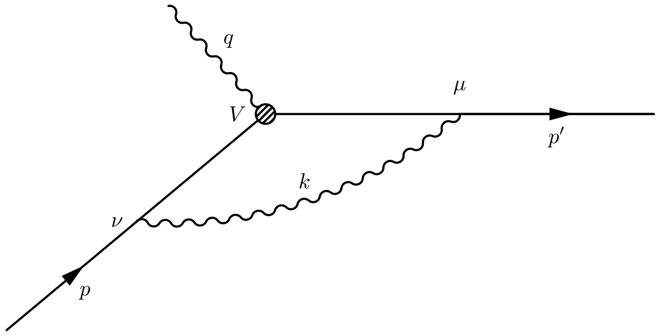

Figure 3.1: *A sample NLO correction to the process $\gamma^* e \to e$; here 'V' is the hard vertex which defines the p and p' leg. See text for details.*

The matrix element for this process can be written as

$$-i\mathcal{M} = \int \frac{d^4k}{(2\pi^4)} \Big[\bar{u}_{p'}(-ie\gamma^\mu) S^0_{p'+k} \Gamma_V S^0_{p+k} (-ie\gamma^\nu) u_p\Big] \left[\frac{-ig_{\mu\nu}}{k^2}\right] , \tag{3.1}$$

where S^0_l stands for the fermion propagator at $T = 0$ with momentum l and we are not interested in the exact structure of the vertex V.

In the Grammer and Yennie technique, the photon propagator is factorised into the soft IR divergent and IR safe part as

$$\begin{aligned} g^{\mu\nu} &= (g^{\mu\nu} - b_k(p_f, p_i) k^\mu k^\nu) + (b_k(p_f, p_i) k^\mu k^\nu) , \\ &= G_k^{\mu\nu} + K_k^{\mu\nu} . \end{aligned} \tag{3.2}$$

The factor b and the terms p_f, p_i will be discussed below. Here the term K contains the

IR divergence while G is finite. Since this is a *sum* over two terms, the cross section (or other physical quantities) can be computed by inserting either a K photon to obtain the IR divergent piece, or by inserting the G photon for the finite part.

Our motive here is to identify the structure of $b_k(p_f, p_i)$ which will be chosen precisely to separate the IR divergent part. We first re-write the matrix element as

$$
\begin{aligned}
-i\mathcal{M} &= \int \frac{d^4k}{(2\pi^4)}\Big[\bar{u}_{p'}(-ie\gamma^\mu)\frac{i(\not{p}' + \not{k} + m)}{(p'+k)^2 - m^2}\Gamma_V \frac{i(\not{p} + \not{k} + m)}{(p+k)^2 - m^2}(-ie\gamma^\nu)u_p\Big]\left(\frac{-ig_{\mu\nu}}{k^2}\right) , \\
&= \frac{-ie^2}{(2\pi)^4}\int d^4k\Big[\bar{u}_{p'}\gamma^\mu \frac{(\not{p}' + \not{k} + m)}{(p'+k)^2 - m^2}\Gamma_V \frac{(\not{p} + \not{k} + m)}{(p+k)^2 - m^2}\gamma^\nu u_p\Big]\frac{g_{\mu\nu}}{k^2} , \\
&= \frac{-ie^2}{(2\pi)^4}\int \frac{d^4k}{k^2}\Big[\bar{u}_{p'}\frac{(2p'^\mu + 2k^\mu - \not{k}\gamma^\mu)}{k^2 + 2p'\cdot k}\Gamma_V \frac{(2p_\mu + 2k_\mu - \gamma_\mu \not{k})}{k^2 + 2p\cdot k}u_p\Big] ,
\end{aligned}
\tag{3.3}
$$

where we have used the standard properties of the gamma matrices and the fermion propagators and the Dirac equation. In the soft limit, this reduces to

$$
-i\mathcal{M} \xrightarrow{k\to 0} \frac{-ie^2}{(2\pi)^4}\int \frac{d^4k}{k^2}\Big[\bar{u}_{p'}\frac{2p'^\mu}{2p'\cdot k}\Gamma_V \frac{2p_\mu}{2p\cdot k}u_p\Big] . \tag{3.4}
$$

In the soft limit $k \to 0$, k^2 goes to zero faster than $2p \cdot k$ (or $2p' \cdot k$) so we can safely ignore k^2 in the denominator. It can be seen that the matrix element with one virtual photon (NLO contribution) can be expressed in terms of the lower order matrix element M_{LO} as

$$
\begin{aligned}
-i\mathcal{M} &\xrightarrow{k\to 0} \left\{\frac{-ie^2}{(2\pi)^4}\int \frac{d^4k}{k^2}\frac{p'\cdot p}{(p'\cdot k)(p\cdot k)}\right\}\left\{\bar{u}_{p'}\Gamma_V u_p\right\} , \\
\text{or } \mathcal{M}_{NLO} &= \left\{\frac{-ie^2}{(2\pi)^4}\int \frac{d^4k}{k^2}\frac{p'\cdot p}{(p'\cdot k)(p\cdot k)}\right\} M_{LO} + \text{IR finite} ,
\end{aligned}
\tag{3.5}
$$

where the coefficient contains the soft divergence. We have separated the soft divergence in Eq. 3.5 and will further show that a special choice of $b_k(p_f, p_i)k_\mu k_\nu$ term in the Grammer and Yennie technique (see Eq. 3.2) can achieve this separation.

The Grammer and Yennie technique [127, 128] requires the definition of a 'hard vertex' which we take to be the vertex ‘V’. Then the fermion leg incoming to this vertex ‘V’ is taken as the ‘p-leg’ and the outgoing one is taken to be the ‘p' leg’. Hence, in our example in Fig. 3.1, we have $p_f = p'$ and $p_i = p$. If both vertices of the virtual photon were on the p' line, $p_f = p_i = p'$, and similarly for the case when both vertices are on the p line, b_k is given by $b_k(p, p)$.

We now show that the K photon insertion contains precisely the IR divergent term shown in Eq. 3.5 with a suitable definition of b_k. For this, we calculate the same matrix element given in Eq. 3.1 but will replace $g^{\mu\nu}$ in the photon propagator by $K^{\mu\nu}$ (i.e., by $b_k k^\mu k^\nu$):

$$\begin{aligned}
-i\mathcal{M}^K &= \frac{-ie^2}{(2\pi)^4}\int d^4k\left[\bar{u}_{p'}\gamma^\mu\frac{(\not{p}'+\not{k}+m)}{(p'+k)^2-m^2}\Gamma_V\frac{(\not{p}+\not{k}+m)}{(p+k)^2-m^2}\gamma^\nu u_p\right]\frac{b_k k_\mu k_\nu}{k^2}\ , \\
&= \frac{-ie^2}{(2\pi)^4}\int d^4k\left[\bar{u}_{p'}\frac{(2p'\cdot k-\not{p}'\not{k}+k^2+m\not{k})}{2p'\cdot k+k^2}\Gamma_V\frac{(2p\cdot k-\not{k}\not{p}+k^2+\not{k}m)}{2p\cdot k+k^2}u_p\right]\frac{b_k}{k^2}\ , \\
&= \frac{-ie^2}{(2\pi)^4}\int d^4k\left[\bar{u}_{p'}\frac{(2p'\cdot k+k^2)}{2p'\cdot k+k^2}\Gamma_V\frac{(2p\cdot k+k^2)}{2p\cdot k+k^2}u_p\right]\frac{b_k}{k^2}\ , \\
&= \left\{\frac{-ie^2}{(2\pi)^4}\int\frac{d^4k}{k^2}b_k\right\}\times\left[\bar{u}_{p'}\Gamma_V u_p\right]\ , \qquad (3.6)
\end{aligned}$$

where we have again simplified using the properties of the gamma matrices and the Dirac equation. Notice that this is a general procedure, independent of the structure of the hard vertex V. Comparing Eqs. 3.5 and 3.6, we identify b_k as

$$b_k(p', p) = \frac{p'\cdot p}{(p'\cdot k)(p\cdot k)}\ . \qquad (3.7)$$

With the choice of ‘b’ in Eq. 3.7 we can see that Eq. 3.6 is exactly the same as Eq. 3.5 which contains the soft IR divergent piece of the full matrix element Eq. 3.1. This example shows that with the precise choice of ‘b_k' we can separate the soft IR divergence by simply factorizing $g^{\mu\nu}$ into the sum of soft IR divergent part $K^{\mu\nu}$ and IR safe part $G^{\mu\nu}$. A complete calculation of all possible photon insertions in Fig. 3.1 will yield the general expressions for $b_k(p_f, p_i)$. The separation of IR divergent and IR safe parts is found to hold to all orders in perturbation theory [127, 128] at $T = 0$. Instead of proceeding in this direction, we use this zero temperature example to determine the corresponding K and G photon propagators in the thermal case of interest.

This separation of IR divergent and IR finite piece is found to be valid at finite temperature with QED vertex [126, 129]. In the next section we will discuss the details of this separation at finite temperature with the generalized Grammer and Yennie technique in thermal field theory for use in later chapters.

3.2 The Grammer and Yennie technique at finite temperature

We have used the Grammer and Yennie (GY) technique to calculate the IR finite part of the *thermal* dark matter annihilation cross section for both the virtual and real photon cases in the next two chapters. We now summarise this approach which helps simplify the separation of the soft infra-red (IR) divergences[1]. The GY technique as described in the previous section [127, 128] was used to factorize the infra-red (IR) divergences in a zero temperature quantum field theory. There are additional *linear* IR divergences due to photons in a thermal field theory. Hence the demonstration of cancellation of IR divergences includes demonstrating the cancellation of both the linear and (sub-leading) logarithmic divergences in the thermal theory.

Note that there are no additional ultra-violet (UV) divergences because the number operator in both the thermal propagators and phase space acts as a damping factor. The GY technique was extended to the case of thermal field theory, first for fermionic thermal QED [129], and later for charged thermal scalars and fermions interacting with dark matter particles with thermal QED corrections [126, 130], where it was shown that the infra-red divergences cancel between virtual and real photon insertions, order by order, to

---

[1] We shall see that the technique fails to factorise out the collinear divergences. However, the technique is still useful because cancellations occur at the integrand level and hence there is no need to compute divergent integrals.

all orders. The technique uses the fact that only the photon contributions are IR divergent, while fermion insertions do not lead to additional IR divergences. The IR divergences cancel between virtual and real photon insertions as briefly discussed below.

3.2.1 Insertion of virtual K photons

Consider first the insertion of a *virtual photon* with momentum k into a lower order graph. While the technique generically holds for an arbitrary n^{th} graph, we use, for clarity, the graph shown in Fig. 4.1 since this corresponds to the dark matter annihilation process of interest. The procedure starts with writing the virtual photon propagator as the sum of two parts, the K and G photons, exactly as in the case of the zero-temperature case; only the definition of $b_k(p_f, p_i)$ (see Eq. 3.2) will be somewhat modified:

$$\begin{aligned} -ig^{\mu\nu} &\to -i\left\{\left[g^{\mu\nu} - b_k(p_f, p_i)\, k^\mu k^\nu\right] + \left[b_k(p_f, p_i) k^\mu k^\nu\right]\right\} \;, \\ &\equiv -i\left\{\left[G_k^{\mu\nu}\right] + \left[K_k^{\mu\nu}\right]\right\} \;. \end{aligned} \tag{3.8}$$

The IR divergence is completely contained in the K photon contribution while the G photon contribution is IR finite. The notation p_f and p_i is used as before to separate the final and initial "legs" (where the photon is inserted at vertices μ, ν) which are defined as being to the right or left of the special vertex V (see Fig. 4.1) at which the momentum q' is guaranteed to be hard (not soft). Hence, for the t-channel diagram in Fig. 4.1, the fermion line with $p_f = p'$ is defined as the final "leg" while the anti-fermion and scalar lines together form the initial leg with $p_i = p$; for the u-channel diagrams, the scalar forms a part of the p' leg instead. Then the factor b_k given by

$$b_k(p_f, p_i) = \frac{1}{2}\left[\frac{(2p_f - k)\cdot(2p_i - k)}{((p_f - k)^2 - m^2)((p_i - k)^2 - m^2)} + (k \leftrightarrow -k)\right] \;, \tag{3.9}$$

is defined symmetrically in $k \to -k$ for the thermal case (in contrast to the original definition at $T = 0$ in Ref. [127]), and is a function of k as well as the momenta, p_f, p_i. It can then be shown that the K photon insertions contain the IR divergent pieces while the G photon contribution is IR finite. We demonstrate this for the NLO case when the thermal K photon is inserted with both its vertices, μ, ν, on the p' fermion line. The relevant part of the matrix element can be expressed using the Feynman rules presented in the previous chapter (note that there is an integration measure over the photon momentum, k) as

$$\begin{aligned} M_{NLO}^{p'p',K\text{photon}} &\propto b_k(p',p') k^\mu k^\nu \left[\overline{u}(p',m_f)\gamma_\mu \mathcal{S}^{t_\mu,t_\nu}_{\text{fermion}}(p'+k,m_f)\gamma_\nu \mathcal{S}^{t_\nu,t_V}_{\text{fermion}}(p',m_f) P_R\, u(q',m_\chi)\right] \cdots , \\ &= b_k(p',p') \left[\overline{u}_{p'}\, \not{k}\, \mathcal{S}^{\mu,\nu}_{p'+k}\, \not{k}\, \mathcal{S}^{\nu,V}_{p'} P_R\, u_{q'}\right] \cdots , \end{aligned} \tag{3.10}$$

where the ellipsis refer to terms independent of k and we have lightened the notation for convenience in the second line, with the superscripts on $\mathcal{S}$ referring to the thermal type. The term in the square brackets can be simplified, using the identities given in Section 2.4.1 as

$$\begin{aligned} [\quad] &= \left[\overline{u}_{p'}\, \not{k} \left\{\mathcal{S}^{\mu,\nu}_{p'+k}\, \not{k} \mathcal{S}^{\nu,V}_{p'}\right\} P_R\, u_{q'}\right] , \\ &= (-1)^{t_\nu+1} \left[\overline{u}_{p'}\, \not{k} \left\{\mathcal{S}^{\mu,V}_{p'}\, \delta_{t_\nu,t_V} - \mathcal{S}^{\mu,V}_{p'+k}\, \delta_{t_\nu,t_\mu}\right\} P_R\, u_{q'}\right] , \\ &= (-1)^{t_\nu+1} \left[\overline{u}_{p'} \left\{0 - \left[(-1)^{t_\mu+1}\, \delta_{t_\nu,t_\mu}\right]\right\} P_R\, u_{q'}\right] , \end{aligned} \tag{3.11}$$

where the first term vanishes since the integrand is odd in $k \to -k$ while both b_k and the measure are even under this exchange. The crucial step is seen in the second line of Eq. 3.11, where the Feynman identities (see Eq. 2.26) are used to reduce the portions with $\not{k}$ insertions to a *difference* of two terms. Hence the matrix element factorises into the product of two terms, one that is proportional to the lower order matrix element, *viz.*,

$$M_{NLO}^{p'p',K\text{photon}} \propto b_k(p',p')\, M_{LO} , \tag{3.12}$$

and the other containing the IR divergence. The contribution to the cross section from virtual photon insertions at a given order is obtained by adding all the matrix elements up-to that order and squaring the sum to obtain $|\mathcal{M}|^2$, integrating over the appropriate phase space, and dividing by the initial flux, as usual. Again, this can be repeated for different insertions of the virtual thermal photon.

3.2.1.1 Insertion into a general n^{th} order graph

Consider an n^{th} order graph with n virtual/real photon vertices; for specificity, we consider higher order corrections to the t-channel diagram. When an additional virtual K-photon is inserted into this graph, there are several possible locations where the additional photon vertices can be inserted. Adding all the contributions gives differences of two terms as seen above, with, more importantly, sets of terms canceling against each other until only one term, that is proportional to the lower order matrix element, is left.

A similar result is obtained when the photon vertices are inserted so that one vertex μ is on the p' leg and the other ν vertex is on the p leg; that is, either on the scalar line or the anti-fermion line. Here again, it turns out that the K photon contribution is proportional[2] to the lower order matrix element:

$$M_{n+1}^{p'p,K\text{photon}} \propto b_k(p', p)\, M_n\ , \tag{3.13}$$

In fact, such an insertion is the sum of contributions when the second ν vertex of the virtual photon is inserted on the scalar, and when it is inserted on the anti-fermion line. These contributions separately cancel among themselves, leaving one term in the former and two in the latter. These cancel across the vertex V, leaving behind a contribution that is again proportional to the lower order graph, as seen in Eq. 3.13 above. In short, it is found [126] that the total matrix element due to insertion of the virtual K photon into an

---

[2] Technically, a virtual photon insertion leads to the number of vertices increasing by 2; we have used the index $(n + 1)$ to indicate that it is an n^{th} order graph with an additional virtual photon.

n^{th} order diagram is given by

$$\mathcal{M}_{n+1}^{K\text{photon,tot}} = \Bigg[\frac{ie^2}{2}\int\frac{\mathrm{d}^4k}{(2\pi)^4}\Bigg\{\delta_{t_\mu,t_1}\,\delta_{t_\nu,t_1}\,D^{t_\mu,t_\nu}(k)\Big[b_k(p',p')+b_k(p,p)\Big]$$
$$+\;\delta_{t_\mu,t_V}\,\delta_{t_\nu,t_V}\,D^{t_\mu,t_\nu}(k)\Big[-2b_k(p',p)\Big]\Bigg\}\Bigg]\mathcal{M}_n\,,$$
$$\equiv [B]\,\mathcal{M}_n\,, \tag{3.14}$$

where the prefactor containing the IR divergence can be expressed as,

$$\begin{aligned} B &= \frac{ie^2}{2}\int\frac{\mathrm{d}^4k}{(2\pi)^4}\,D^{11}(k)\Big[b_k(p',p')-2b_k(p',p)+b_k(p,p)\Big]\,,\\ &\equiv \frac{ie^2}{2}\int\frac{\mathrm{d}^4k}{(2\pi)^4}\,D^{11}(k)\Big[J^2(k)\Big]\,, \end{aligned}\tag{3.15}$$

since the thermal types of the hard/external vertices must be type-1. We see that each term is proportional to the (11) component of the photon contribution and this is crucial for achieving the cancellation between virtual and real photon insertions.

When the contributions are summed over all orders in perturbation theory and squared, the relevant IR divergent factor $(B + B^*)$ exponentiates and cancels a similar IR divergent factor arising from real soft photon insertions; for details please refer to Ref. [126].

3.2.1.2 Insertion of the photon into a thermal fermion line

We already know that the presence of the bosonic number operator, $n_B(|k^0|)$, makes the IR contribution to the cross section potentially IR divergent while the nature of the fermionic number operator, $n_F(|p^0|)$, results in a finite IR contribution to the cross section. In particular, we shall see below that the K-photon contribution when the additional photon is inserted into a thermal fermion (that is, when the second, temperature-dependent term in the fermionic propagator contributes; see Eq. 2.22), is zero. We will use this result later in the computation of the NLO cross section of interest. In order to show this, we begin with the insertion of one of the vertices of the additional K photon on any thermal fermion line at the vertex μ, lying between vertices μ_{q+1} and μ_q; see Fig. 3.2.

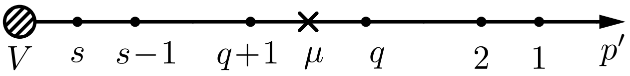

Figure 3.2: *Sample insertion of vertex μ of virtual photon between vertices μ_q and μ_{q+1} on the p' fermion line. The labels have been simplified ($\mu_i \to i$) for the sake of clarity. Only a portion of the diagram containing the p' leg to the right of vertex V has been shown here.*

There are now two fermion propagators, one between vertices μ_q and μ and the other between vertices μ and μ_{q+1}. The relevant part of the matrix element is given by (where we have chosen to insert into the p' fermion line for specificity),

$$\begin{aligned} M_{NLO}^{\text{thermal f},K\gamma} &\propto b(p_f, p_i) k^\mu k^\nu \left[\overline{u}_{p'} \gamma_{\mu_1} \cdots \gamma_{\mu_q} \, S^{q,\mu}_{p'+\Sigma_q} \gamma_\mu \, S^{\mu,q+1}_{p'+\Sigma_q+k} \, \gamma_{\mu_{q+1}} \right] \cdots \,, \\ &= b(p_f, p_i) k^\nu \left[\overline{u}_{p'} \gamma_{\mu_1} \cdots \gamma_{\mu_q} \, \left\{ S^{q,\mu}_{p'+\Sigma_q} \not{k} \, S^{\mu,q+1}_{p'+\Sigma_q+k} \right\} \gamma_{\mu_{q+1}} \right] \cdots \,, \end{aligned} \tag{3.16}$$

where the momentum flowing in the fermion line between vertices q and $(q+1)$ into which the additional photon was inserted is $p' + l_1 + \cdots + l_q \equiv p' + \Sigma_q$. The term in curly braces can be simplified using the property of the fermion propagator shown in Eq. 2.22 where $\overline{S}$ is also defined:

$$\begin{aligned} \{\cdots\} &= \left[(\not{p}' + \not{\Sigma}_q + m_f) \not{k} (\not{p}' + \not{\Sigma}_q + \not{k} + m_f) \right] \overline{S}^{q,\mu}_{p'+\Sigma_q} \overline{S}^{\mu,q+1}_{p'+\Sigma_q+k} \,, \\ &= \left[(2(p' + \Sigma_q) \cdot k + k^2) \, (\not{p}' + \not{\Sigma}_q + m_f) - ((p' + \Sigma_q)^2 - m_f^2) \not{k} \right] \,, \\ &= 0 \;\; \text{for thermal fermions.} \end{aligned} \tag{3.17}$$

In particular, if both the fermion propagators on either side of the K-photon insertion at the vertex μ are thermal, then both terms in Eq. 3.17 vanish due to the delta function terms $\delta((p' + \Sigma_q)^2 - m_f^2)$ and $\delta((p' + \Sigma_q + k)^2 - m_f^2)$ in the thermal part of the respective propagators. We will use this result in the next Chapter when we compute the NLO virtual thermal cross section.

3.2.2 Insertion of real $\widetilde{K}$ photons

While the factorization of the IR divergent part occurs in the *matrix element* for virtual photon insertions, it occurs in the *square* of the matrix elements for the real photon case. Note that both emission and absorption of real photons into/from the heat bath are possible in the thermal case; in fact, this is essential in order to show the IR divergence cancellation between virtual and real photon contributions. When a real photon with momentum k is inserted into a lower order diagram at a vertex μ, the polarization sum in the squared matrix element can be re-written in terms of the $\widetilde{K}$ and $\widetilde{G}$ contributions:

$$\begin{aligned} \sum_{\mathrm{pol}} \epsilon^{\mu *}(k)\, \epsilon^{\nu}(k) = -g^{\mu\nu} &= -\left\{ \left[g^{\mu\nu} - \tilde{b}_k(p_f, p_i) k^\mu k^\nu \right] + \left[\tilde{b}_k(p_f, p_i) k^\mu k^\nu \right] \right\} , \\ &\equiv -\left\{ \left[\widetilde{G}_k^{\mu\nu} \right] + \left[\widetilde{K}_k^{\mu\nu} \right] \right\} , \end{aligned} \tag{3.18}$$

with $\tilde{b}_k(p_f, p_i) = b_k(p_f, p_i)|_{k^2=0}$ for real photons. Again, p_i (p_f) is the momentum p' or p depending on whether the real photon insertion was on the p' or p leg in the n^{th} order matrix element $\mathcal{M}_{n+1}$ (or its conjugate $\mathcal{M}_{n+1}^{\dagger}$). As in the case for virtual K photon insertion, the insertion of a $\widetilde{K}$ real photon into an n^{th} order graph leads to a cross section that is proportional to the lower order one by an overall factor analogous to that in Eq. 3.14 for virtual photon insertion:

$$\left| \mathcal{M}_{n+1}^{\widetilde{K}\gamma,\mathrm{tot}} \right|^2 \propto -e^2 \left[\tilde{b}_k(p,p) - 2\tilde{b}_k(p',p) + \tilde{b}_k(p',p') \right] \left| \mathcal{M}_n^{\mathrm{tot}} \right|^2 .$$

Since we are dealing with real photon insertions, recall that the phase space factor which accounts for both emission and absorption also contains k dependence; see Eq. 2.27. Then the total k-dependent part that factorises out of the expression can be written as [126, 130],

$$\widetilde{B}(x) = -e^2 \int \mathrm{d}P_k \left[\tilde{b}_k(p,p) - 2\tilde{b}_k(p',p) + \tilde{b}_k(p',p') \right] \exp\left[\pm i\, k \cdot x \right] , \tag{3.19}$$

where the ± sign depends on whether the photon with momentum k is emitted/absorbed.

3.2.3 The factorised cross section

After some simplification, and including the finite contributions from the G and $\widetilde{G}$ insertions, the total cross section can be expressed as

$$\sigma^{\text{tot}} = \int \mathrm{d}^4x\, e^{-i(q'+q-p'-p)\cdot x}\, \mathrm{d}P_{p'} \mathrm{d}P_p \exp\left[B + B^* + \widetilde{B}\right] \sigma^{\text{finite}}(x)\,. \tag{3.20}$$

Here σ^{finite} contains the finite G and $\widetilde{G}$ photon contributions from the virtual and real thermal photons respectively, as well as the (finite) thermal fermion contributions. In the limit $k \to 0$, the exponential IR divergent parts of both the virtual and real photon contributions can be seen to cancel:

$$(B + B^*) + \widetilde{B} \overset{k\to 0}{\longrightarrow} 0 + O(k^2)\,. \tag{3.21}$$

Hence the total cross section is IR finite to all orders, with the IR divergent part of the real photon cross section cancelling against the corresponding IR divergent part of the virtual contribution.

In the next chapters, we will therefore compute the finite remainder at $O(\alpha)$ arising from the finite combination, $[(B + B^*) + \widetilde{B}]$, which we shall label, for convenience, as $(K + \widetilde{K})$, and the finite contribution, $\widetilde{G}$. With this summary explanation of the GY technique for thermal field theories, we now go on to the main results of our work.

Chapter 4

Virtual Thermal Corrections to the DM Annihilation Cross Section

In this chapter, we will present the virtual thermal corrections to the dark matter annihilation cross section into SM fermions, viz., $\chi\chi \to f\overline{f}$. The contents of this chapter are largely found in Ref. [131]. We first present details of the leading order (LO) cross section, for reference.

4.1 The dark matter annihilation cross section at LO

We use the Feynman rules and the Lagrangian for Majorana-type dark matter interactions described in the previous chapters to compute the leading order (LO) contribution to the annihilation process $\chi\overline{\chi} \to f\overline{f}$. Contributions arise from both the t- and u-channel processes shown in Fig. 4.1. Note that the LO contribution is temperature independent; we comment on the reasons below.

We work in the center-of-momentum (CM) frame where the momenta of the particles are

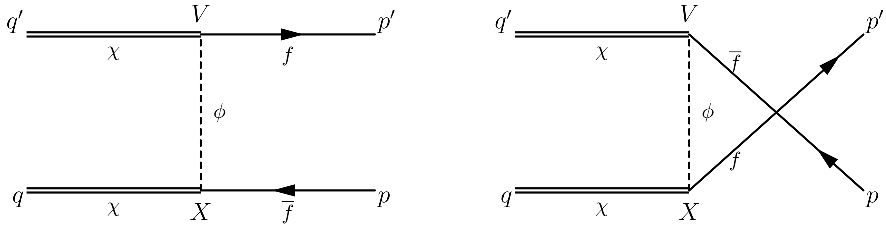

Figure 4.1: *The t-channel and u-channel dark matter annihilation processes at leading order (LO).*

given by $(q', q \to p', p)$, with the choices,

$$q'^{\mu} = (H, 0, 0, Q)\,, \qquad q^{\mu} = (H, 0, 0, -Q)\,,$$
$$p'^{\mu} = (H, P\sin\theta, 0, P\cos\theta)\,, \qquad p^{\mu} = (H, -P\sin\theta, 0, -P\cos\theta)\,, \tag{4.1}$$

where the center of momentum energy, $s = 4H^2$, and θ is the angle between the initial and final momenta $(\vec{q}\,', \vec{p}\,')$. At leading order, the cross section is given by,

$$\begin{aligned}\sigma_{LO} &= \frac{1}{64\pi^2 s}\frac{|\vec{p}\,'|}{|\vec{q}\,'|}\int \mathrm{d}\Omega \left[\sum_{spins} |\mathcal{M}^t_{LO} - \mathcal{M}^u_{LO}|^2\right]\,, \\ &= \frac{1}{32\pi s}\frac{P}{Q}\int \mathrm{d}\cos\theta \left[\sum_{spins} |\mathcal{M}^t_{LO} - \mathcal{M}^u_{LO}|^2\right]\,,\end{aligned} \tag{4.2}$$

where the integration over the azimuth ϕ is trivial, and a summation over both final state and initial state spins is to be performed since all helicity configurations contribute to the total cross section. The t-, u-channel matrix elements at LO are given by,

$$\begin{aligned}\mathcal{M}^t_{LO} &= i\lambda^2 \left(\overline{v}(q, m_\chi) P_L\, v(p, m_f)\right)\, \Delta(l)\, \left(\overline{u}(p', m_f) P_R\, u(q', m_\chi)\right)\,, \\ \mathcal{M}^u_{LO} &= i\lambda^2 \left(\overline{v}(q', m_\chi) P_L\, v(p, m_f)\right)\, \Delta(l')\, \left(\overline{u}(p', m_f) P_R\, u(q, m_\chi)\right)\,,\end{aligned} \tag{4.3}$$

where $P_{R,L} \equiv (1 \pm \gamma_5)/2$, and $\Delta(l) = i/(l^2 - m_\phi^2)$ is the scalar propagator with $l = q - p \equiv p' - q'$ and $l' = q' - p \equiv p' - q$ referring to the momentum of the intermediate scalar for the t and u channels respectively, with the scalar assumed to be heavy, $m_\phi \gg m_\chi, m_f$.

The cross section can therefore be expressed in terms of the three contributions:

$$\begin{aligned}\int \mathrm{d}\cos\theta \sum_{spins} |\mathcal{M}^t_{LO} - \mathcal{M}^u_{LO}|^2 &\equiv Int^t_{LO} + Int^u_{LO} - Int^{tu}_{LO} \,, \\ &\equiv Int^{tot}_{LO} \,, \end{aligned} \tag{4.4}$$

where the subscript *LO* denotes the LO contribution and the three terms on the right hand side refer to the square of the t-channel matrix element, the square of the u-channel matrix element, and the tu cross terms respectively. Only the t-channel contributes for Dirac-type dark matter particles. Adding all the contributions, we find,

$$\begin{aligned} Int_{LO} = \frac{2\lambda^4}{QP(2H^2 - m^2_\Phi)} \Bigg\{ &- \left[H^2\left(m^2_\chi - 2m^2_\Phi\right) + m^2_\chi P^2 + m^4_\Phi\right] \log\frac{\left(2H^2 - m^2_\Phi + 2QP\right)}{\left(2H^2 - m^2_\Phi - 2QP\right)} \\ &+ \frac{4QP\left(2H^2 - m^2_\Phi\right)\left(2H^4 - 2H^2 m^2_\Phi + m^4_\Phi - 2Q^2P^2\right)}{4H^4 - 4H^2 m^2_\Phi + m^4_\Phi - 4Q^2P^2} \Bigg\} \,, \end{aligned} \tag{4.5}$$

where $m^2_\Phi \equiv m^2_\chi + m^2_f - m^2_\phi$. The logarithmic terms arise when either of p, p' are collinear with one of q, q'; however, these are not divergent; they contribute at a single phase space point and are well-behaved. Then the invariant cross section at LO can be written as

$$\sigma_{LO}(s) = \frac{1}{32\pi s}\frac{P}{Q} Int_{LO} \,, \tag{4.6}$$

where $P^2 = H^2 - m^2_f$, $Q^2 = H^2 - m^2_\chi$, and $4H^2 = s$, the usual Mandelstam variable.

4.1.0.0.1 LO cross section in the non-relativistic limit : In the non-relativistic limit, when the velocity v of the dark matter particles is small, we can write $Q = m_\chi v$ and $H^2 \approx m^2_\chi(1 + v^2)$. Since $Q \ll H, m_\Phi$, we can expand the log term as

$$\log\frac{\left(2H^2 - m^2_\Phi + 2QP\right)}{2H^2 - m^2_\Phi - 2QP} \xrightarrow{Q\ small} 2\left[\frac{2QP}{2H^2 - m^2_\Phi} + \frac{2}{3}\left(\frac{2QP}{2H^2 - m^2_\Phi}\right)^3 + \cdots\right] \,, \tag{4.7}$$

to get

$$Int_{LO} \xrightarrow{v\ small} \frac{8\lambda^4 m_\chi^2 m_f^2}{(m_\chi^2 + m_\phi^2 - m_f^2)^2} + O(v^2)\,, \tag{4.8}$$

Notice that the cross section is proportional to the square of the fermion mass, which is a well-known result [94]. Hence, the LO cross section can be written as

$$\begin{aligned} \sigma_{LO}(s) = & \frac{1}{32\pi s}\frac{P}{Q} Int_{LO}\,, \\ \xrightarrow{v\ small} & \frac{\lambda^4}{4\pi s}\frac{P}{Q}\left[\frac{m_\chi^2 m_f^2}{(m_\chi^2 + m_\phi^2 - m_f^2)^2} + O(v^2)\right]. \end{aligned} \tag{4.9}$$

In the non-relativistic case, the annihilation cross section is usually expressed as a series expansion in v^2: $s\,\sigma(s)v_{rel} = a + bv^2 + cv^4 + \cdots$ [94], with the relative velocity between the two dark matter particles given by $v_{rel} = 2v$, where v is the CM velocity of either of the particles. Hence Eq. 4.9 represents the velocity-independent "a" term in this series. Terms of higher order in $O(v^2)$ can be calculated by retaining higher orders in the expansion of Eq. 4.5.

We can repeat the calculation in the limit when the scalar is much heavier than the other particles, *viz.*, $m_\phi^2 \gg m_\chi^2 \gtrsim m_f^2$. Then $l^2 \equiv (q-p)^2 \ll m_\phi^2$ (where we have implicitly assumed that $\sqrt{s} \ll m_\phi$) and the scalar propagator can be approximated by $iD_\phi = i/(l^2 - m_\phi^2) \to -i/m_\phi^2$, so that we get

$$\begin{aligned} Int_{LO}^{\text{heavy-scalar}} &= \frac{8\lambda^4}{3m_\phi^4}\left[6H^4 - 3H^2 m_\chi^2 + P^2(2Q^2 - 3m_\chi^2)\right], \\ &= \frac{8\lambda^4}{3m_\phi^4}\left[8H^2(H^2 - m_\chi^2) + m_f^2(5m_\chi^2 - 2H^2)\right], \end{aligned} \tag{4.10}$$

where we have substituted for Q, P in the last line. This gives us a cross section,

$$\sigma_{LO}^{\text{Majorana}} = \frac{1}{12\pi s}\frac{P}{Q}\frac{\lambda^4}{m_\phi^4}\left[8H^2(H^2 - m_\chi^2) + m_f^2(5m_\chi^2 - 2H^2)\right]. \tag{4.11}$$

The first term in the square brackets is proportional to $H^2 - m_\chi^2 \equiv Q^2 \approx m_\chi^2 v^2$ and vanishes in the non-relativistic limit. The second term is proportional to m_f^2 and is therefore helicity suppressed because of the nature of the coupling; see Eq. 1.8. In contrast, the purely t-channel contribution (relevant for a Dirac-type dark matter particle) is not helicity suppressed; we have,

$$\sigma_{LO}^{\text{Dirac}} = \frac{1}{96\pi s}\frac{P}{Q}\frac{\lambda^4}{m_\phi^4}\left[H^2(4H^2 - m_\chi^2) - m_f^2(H^2 - m_\chi^2)\right] . \tag{4.12}$$

In the non-relativistic limit, with $H^2 = m_\chi^2(1 + v^2)$, $Q = m_\chi v$, this matches the expression given in Eq. 4.9, with the further approximation, $(m_\chi^2 + m_\phi^2 - m_f^2) \to m_\phi^2$, which is valid in the heavy scalar limit. Then, the LO cross section can be written as

$$\sigma_{LO}^{\text{Majorana}} v_{rel} \xrightarrow{Heavy\ Scalar} \frac{\lambda^4}{48\pi}\left[\frac{1}{m_\phi^4}\right]\left[6m_f^2 + v^2\left(16m_\chi^2 - 7m_f^2\right)\right]\left[1 - \frac{m_f^2}{2m_\chi^2}\right] , \tag{4.13}$$

where we have retained terms up to order $O(v^2)$.

The thermal average of the cross section is the collision term of interest in the Boltzmann equation to compute the dark matter relic density: to leading order we have[1]

$$\langle\sigma_{LO}^{\text{Majorana}} v_{rel}\rangle_T \xrightarrow{Heavy\ Scalar} \frac{\lambda^4}{48\pi}\left[\frac{1}{m_\phi^4}\right]\left[6m_f^2 + \frac{3T}{2m_\chi}\left(16m_\chi^2 - 7m_f^2\right)\right]\left[1 - \frac{m_f^2}{2m_\chi^2}\right] , \tag{4.14}$$

where we have used the non-relativistic Maxwell-Boltzmann distribution function [132] for the dark matter particles so that $\langle v^2\rangle_T = 3T/(2m_\chi)$.

4.1.1 Thermal corrections to the cross section at LO

As seen in Chapter 2, thermal corrections to cross sections arise from thermal terms in the propagator and in the phase space of final state particles. For the LO contributions shown

---

[1] This is the thermally averaged center-of-momentum cross section; a further multiplying factor is required to convert it to the actual lab-frame collision term; however, here we are primarily interested in the powers of temperature of the various terms, or rather, powers of $x^{-1} = T/m_\chi$.

in Fig. 4.1, these then arise from the scalar propagator and from the fermion phase space factors.

Since the scalar is heavy, the thermal component of its propagator is suppressed by $n_B(E) \sim \exp[-\beta E]$. Since $E \gtrsim m_\phi$, we can ignore this contribution.

As for the phase space thermal contribution, in a $2 \rightarrow 2$ process, the energies of the final state fermions are fixed, $E' = E = H \equiv \sqrt{s}/2$; hence the thermal contribution is proportional to $n_F(E_f) = n_F(H)$. Again, since $\beta H \gg 1$, this contribution can be ignored. Hence, there is no thermal contribution to the dark matter annihilation at LO.

4.2 Virtual thermal corrections to the cross section at NLO

We are interested in the cross section in as much as it contributes to the collision term in the Boltzmann equation for the dark matter relic densities. We therefore are in a regime where electro-weak symmetry breaking has already occurred and hence the $W^\pm$ and Z^0 are massive. We therefore consider corrections at NLO due to photons alone.

There are two sets of contributions at higher order: insertions of a virtual photon in the LO diagrams shown in Fig. 4.1, as well as insertions of real photons which can be both emitted into or absorbed from the heat bath at temperature T. Each of these contributions can be factorised into K and G (or $\widetilde{K}$ and $\widetilde{G}$) parts for virtual (or real) photon insertions respectively, by applying the Grammer and Yennie technique [126, 127] as described in the previous Chapter. As a consequence, the IR divergences are contained in the K ($\widetilde{K}$) contributions respectively and furthermore, were shown earlier to cancel not only at NLO [94], but at all orders [126] in perturbation theory.

The various sets of virtual diagrams contributing at this order are shown in Figs. 4.2, 4.3 and 4.4. Again, since these are $2 \rightarrow 2$ processes, there is no thermal contribution from the phase space factors, and the only thermal contributions arise from the propagator terms.

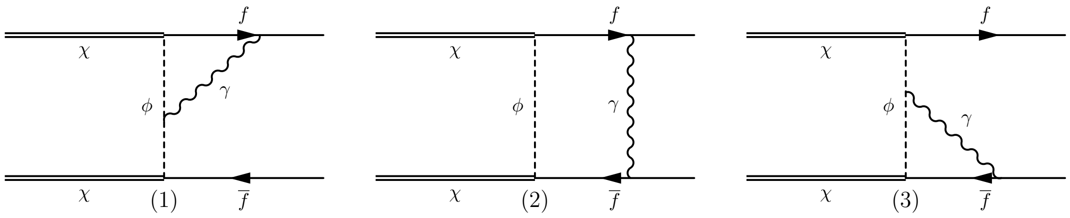

Figure 4.2: *A set of t-channel virtual photon corrections to the dark matter annihilation process at next to leading order (NLO). Diagrams are labelled from 1–3. Analogous contributions from the u-channel diagrams exist.*

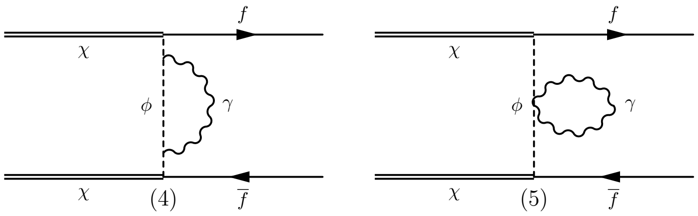

Figure 4.3: *The set of t-channel virtual photon corrections to the dark matter annihilation process at next to leading order (NLO). Diagrams labelled 4, 5 correspond to scalar self-energy corrections. Analogous contributions from the u-channel diagrams exist.*

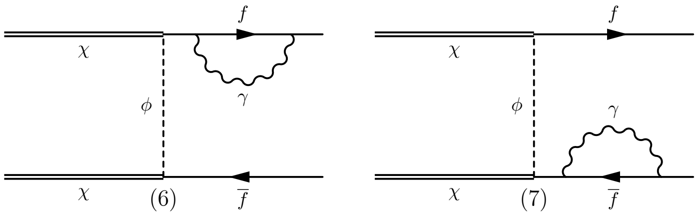

Figure 4.4: *The set of t-channel virtual photon corrections to the dark matter annihilation process at next to leading order (NLO). Diagrams labelled 6, 7 correspond to fermion, anti-fermion self energy corrections. Analogous contributions from the u-channel exist.*

In contrast, the sets of real photon diagrams contributing at this order are shown in Fig. 5.1 where the thermal phase space factors are important. Note that both t- and u-channel (and the cross tu-channel) processes contribute to the virtual and real photon diagrams. In addition, in the real photon case, both emission into, and absorption from the heat bath are possible, in contrast to the zero temperature case. As described in Chapter 3, the IR divergences cancel between the virtual and real contributions. We discuss the real photon case in detail in the next chapter where we explicitly demonstrate this cancellation for both soft IR and collinear divergences.

Analogous to the LO cross section, we can write the next-to-leading order (NLO) virtual contribution as the coefficient of the $\mathcal{O}(\alpha)$ term in,

$$\sigma_{NLO}^{Virtual} \propto \int \left|\mathcal{M}_{LO}^{t} - \mathcal{M}_{LO}^{u} + \mathcal{M}_{NLO}^{1-7,t} - \mathcal{M}_{NLO}^{1-7,u}\right|_{\alpha}^{2} , \tag{4.15}$$

where the subscript α denotes the NLO contribution. Here we have suppressed the phase space and other factors in the interest of clarity. Each of the higher order t-channel matrix elements in Eq. 4.15 gets contributions from the t-channel diagrams shown in Figs. 4.2, 4.3 and 4.4 (and similarly, their u-channel counterparts). Furthermore, throughout this calculation, we will approximate the scalar propagator by $iD_\phi = i/(l^2 - m_\phi^2) \to -i/m_\phi^2$, as discussed at LO. In each instance, we will compute the following sets:

1. the (soft) IR divergent K photon contribution, that will cancel against similar terms from the real photon case,
2. the IR finite contribution, which arises from the finite G photon contribution as well as the (finite) fermion contribution,
3. the collinearly divergent terms. These will arise diagram by diagram for all diagrams and we will again show that these cancel against similar terms from the real photon calculation.

We will discuss the details of the calculation using Diagram 1 as an example, before we list the contributions from the remaining diagrams.

4.2.1 The NLO thermal virtual contribution from Diagram 1

We start by discussing the pure t-channel NLO contribution from the first diagram in Fig. 4.2. This arises from the cross between the t-channel LO diagram shown in Fig. 4.1 and the t-channel NLO contribution from Diagram 1, i.e.,

$$\sigma^t_{NLO}(\text{Diagram1}) \ \propto \ \int \left[\mathcal{M}^t_{LO} \mathcal{M}^{1,t\ \dagger}_{NLO} + \mathcal{M}^{t\ \dagger}_{LO} \mathcal{M}^{1,t}_{NLO} \right] . \qquad (4.16)$$

Since the scalar is very heavy, the thermal contribution from the scalar propagators, which contain a factor $n_\phi = 1/(\exp\left[\beta E_\phi\right] - 1)$, can be dropped since $E_\phi \gtrsim m_\phi \gg m_\chi$ and $\beta m_\chi \equiv x \sim 20$ near freeze-out. Hence the scalar propagators can only be of (11) or (22) type; see Chapter 2 for details on the thermal and temperature independent parts of various propagators. Since all external lines can only be of type-1 [123], and scalar propagators of (12) or (21) type can be neglected, it can be seen that *all* propagators are of type (11) and all vertices are of type-1 alone. In fact, we will find that this holds for all the contributions at NLO, for all the diagrams shown in Figs. 4.2, 4.3 and 4.4.

Therefore, there are three possibilities for Diagram 1, *viz.*,

1. the photon propagator (with momentum k) is thermal,
2. the fermion propagator (with momentum $p' + k$) is thermal,
3. or both are thermal,

where, by thermal, we refer to the explicitly T-dependent second term in the propagators as defined in Eq. 2.9 of Chapter 2. Since the thermal part of all propagators puts the particle on mass-shell, the last option yields a term depending on the product $\delta(k^2)\,\delta((p' +$

$k)^2 - m_f^2)$. Since the external fermion is on-shell, $p'^2 = m_f^2$; hence this product of delta functions requires $p' \cdot k = 0$. But $\delta(k^2)$ implies $k^0 = \pm|\vec{k}|$ or the angle between k and p' should satisfy $\cos\theta_{kp'} = \pm p'^0/|\vec{p}'|$ or $|\cos\theta_{kp'}| > 1$, which is impossible, so there is no phase space available in the case that both propagators are on-shell. Hence we only need to consider the contribution of the first diagram when either one of the photon or the fermion propagator is thermal and add the contributions.

Since the virtual photon vertices in Diagram 1, Fig. 4.2, are on the final fermion leg and the scalar, we have $p_f = p'$, $p_i = p$, with $b_k(p_f, p_i)$ defined in Eq. 3.9. We consider in turn, the contribution from the thermal parts of the photon and fermion propagators respectively to the cross section for the process shown in Diagram 1 of Fig. 4.2. We present the purely t-channel contribution in detail in order to highlight some technicalities, and then go on to the other contributions.

4.2.1.1 NLO thermal photon contributions to Diagram 1

When thermal photons are inserted into the LO diagram to obtain Diagram 1, there are two contributions, from the K and G photon terms respectively. The matrix element at NLO from the (t-channel) Diagram 1 in Fig. 4.2 when the G-photon propagator is thermal, is given by,

$$\begin{aligned}\mathcal{M}^t_{NLO}(\text{Diagram }1, G\gamma) = &-\int \frac{\mathrm{d}^4k}{(2\pi)^4} \frac{ie^2\lambda^2}{2k \cdot p'} \left(2\pi\delta(k^2) n_B(|k^0|)\right) \Delta(l)\Delta(l+k) \\ &\quad \Big[\left(\overline{u}(p', m_f)\gamma_\mu \left(\not{k} + \not{p}' + m_f\right) P_R\, u(q', m_\chi)\right) \\ &\quad\quad (k - 2p + 2q)_\nu \left(\overline{v}(q, m_\chi) P_L\, v(p, m_f)\right)\Big]\; G_k^{\mu\nu}(p', p)\,, \\ \equiv &\int \frac{\mathrm{d}^4k}{(2\pi)^4} \left(2\pi\delta(k^2) n_B(|k^0|)\right) F^{t,1\gamma}_{NLO}(k)\,, \end{aligned} \tag{4.17}$$

where n_B is the Bose distribution function given in Eq. 2.19 and we have used the index (Diagram $1, G\gamma$) to indicate that this is the G photon contribution from Diagram 1 of Fig. 4.2 when the photon is thermal. At this point, we are in a position to justify the simplification of the scalar propagator in the heavy-scalar approximation. The scalar propagator for the t-channel diagrams contains either the inverse of $(l^2 - m_\phi^2)$, or $((l+k)^2 - m_\phi^2)$, with $l \equiv q - p \equiv p' - q'$. Since $m_\chi \ll m_\phi$, we have $l^2 < m_\phi^2$. Since the photon propagator is thermal, $k^2 = 0$ and $l \cdot k \propto |k^0|$ is small since a large $k^0 = |\vec{k}|$ will suppress the contribution due to the presence of the $n_B(|k^0|)$ term. Hence either of the scalar propagators can be approximated by just the $(-i(m_\phi^2)^{-1})$ terms.

A similar reasoning will hold in the next Section 4.2.1.2 when we consider the fermion propagator to be thermal. Then we can write $(l + k)^2 = ((p' + k) - q')^2 \equiv (t - q')^2$ (see Eq. 4.28). Now $(p' + k)^2 \equiv t^2 = m_f^2$ since the fermion propagator is thermal and $t \cdot q$ should be small, otherwise the contribution will be killed by the $n_F(|t^0|)$ term; see Eq. 2.23. A similar argument holds for Diagrams 2 and 3 in Fig. 4.2 when the anti-fermion is thermal, where we can write $(l + k)^2 = (q - p + k)^2 \equiv (q - t)^2$. For the u-channel matrix elements, the scalar momentum is $l' = q' - p$ and the same reasoning applies. Hence we will replace $\Delta(l) = i/(l^2 - m_\phi^2) \to i/(-m_\phi^2)$, etc., in this section. When the scalar is heavy, but not much heavier than the dark matter particle or the scale of the interaction ($\sqrt{s}$), we can expand the denominator of the scalar propagator, since $l \cdot k, k^2 \ll m_\phi^2$ as

$$\begin{aligned} \frac{1}{(l+k)^2 - m_\phi^2} &= \frac{1}{(l^2 - m_\phi^2) + (2l \cdot k + k^2)} \\ &\approx \frac{1}{(l^2 - m_\phi^2)} \left[1 - \frac{(2l \cdot k + k^2)}{(l^2 - m_\phi^2)} \right] . \end{aligned} \tag{4.18}$$

Similar expansions can be obtained for the u-channel scalar propagators as well. This enables us to get analytic expressions for the NLO cross section. The results are rather cumbersome and opaque; they are available as Mathematica [133] Notebooks in Ref. [134]. However, the core of the results, viz., that the NLO contribution is also helicity suppressed for Majorana-type DM, etc., holds good here as well. Hence we will remain within the heavy scalar approximation throughout this thesis.

The integration over the photon momentum k can be partly completed using the delta function:

$$\begin{aligned}
\int \mathrm{d}^4k \left(2\pi\delta(k^2)\right) F(k) &= 2\pi \int_{-\infty}^{\infty} \mathrm{d}k^0 \int_0^{\infty} K^2 \mathrm{d}K \int \mathrm{d}\Omega_k \left[\delta((k^0)^2 - K^2)\right] F(k^0, K, \Omega_k)\ , \\
&= 2\pi \int \mathrm{d}k^0 \int \mathrm{d}\Omega_k \int K^2 \mathrm{d}K \frac{\left[\delta(k^0 - K) + \delta(k^0 + K)\right]}{|2k^0|} F(k^0, K, \Omega_k)\ , \\
&= \pi \int \mathrm{d}\Omega_k \left[\int_0^{\infty} |k^0| \mathrm{d}k^0 F(k^0, k^0, \Omega_k) + \int_{-\infty}^{0} |k^0| \mathrm{d}k^0 F(k^0, -k^0, \Omega_k)\right]\ , \\
&\equiv \pi \int_0^{\infty} \omega \mathrm{d}\omega \left[\int \mathrm{d}\Omega_k F_+(\omega, \omega, \Omega_k) + \int \mathrm{d}\Omega_k F_-(-\omega, \omega, \Omega_k)\right]\ ,
\end{aligned} \tag{4.19}$$

where $K \equiv |\vec{k}|$. Hence there are two contributions to $\mathcal{M}^t_{NLO}(\text{Diagram } 1, G\gamma)$ (and to each such matrix element), one where $K \to k^0 \equiv \omega$, and the other where $K \to -k^0 \equiv -\omega$, as can be seen from Eq. 4.19. (We have suppressed the other dependences of the functions $F_\pm$.) Note that the lower limit ($\omega \to 0$) can be safely taken precisely because the G photon contribution is guaranteed to be IR-finite. The purely t-channel thermal G-photon contribution from Diagram 1 is therefore given according to Eq. 4.15 as

$$\begin{aligned}
\sigma^t_{NLO}(\text{Diagram } 1, G\gamma) &= \frac{1}{32\pi s(2\pi)^4} \frac{|\vec{p}'|}{|\vec{q}'|} \int \mathrm{d}\cos\theta \left[\sum_{spins} \left(\mathcal{M}^t_{LO}\right)^\dagger \mathcal{M}^{t,1\gamma}_{NLO} + h.c.\right]\ , \\
&= \frac{1}{32 s(2\pi)^4} \frac{|\vec{p}'|}{|\vec{q}'|} \int \omega \mathrm{d}\omega\, n_B(\omega) \left[\int \mathrm{d}\cos\theta \int \mathrm{d}\Omega_k \left[F^{t,1,\gamma}_+ + F^{t,1,\gamma}_-\right]\right]\ , \\
&\equiv \frac{1}{32 s(2\pi)^4} \frac{|\vec{p}'|}{|\vec{q}'|} \int \omega \mathrm{d}\omega\, n_B(\omega) Int^t_{\text{Diagram } 1, G\gamma}\ .
\end{aligned} \tag{4.20}$$

On performing the angular integrations (using Mathematica [133]), the contribution of this term to the NLO cross section is given by,

$$Int^t_{\text{Diagram } 1, G\gamma} = \frac{64\pi e^2 \lambda^4}{3 m_\phi{}^6 P} \left[4P\left(3H^4 + Q^2P^2\right) + 3H\left(H^2 + Q^2\right)\left(H^2 + P^2\right) \log \frac{H - P}{H + P}\right]\ . \tag{4.21}$$

Note that the result in Eq. 4.21 is independent of ω; in fact, the individual F_+ and F_- contributions to $Int^t_{\text{Diagram } 1, \gamma}$ contain some apparent logarithmic sub-divergent terms of the order of $1/\omega$ (Note the presence of the multiplying factor ω in Eq. 4.20.) When the two terms are added, these cancel, leaving behind IR finite terms that are integrable in ω. This is a reflection of the fact that the G photon insertion was tailored precisely to yield such an IR-finite result. The logarithmic terms in Eq. 4.21 arise when $\vec{p}\,'$ or $\vec{p}$ are collinear with $\vec{q}\,'$ or $\vec{q}$. These will drop out of the final calculation; in the next chapter we will show that these collinear terms cancel between the virtual and real photon contributions [94].

Similarly, the u-channel and crossed tu-channel NLO contributions from Diagram 1 of Fig. 4.2 when the G photon propagator is thermal can be calculated from the corresponding u-channel NLO matrix element as

$$\begin{aligned}\mathcal{M}^{u}_{NLO}(\text{Diagram 1}, G\gamma) = -\int \frac{\mathrm{d}^4 k}{(2\pi)^4} \frac{ie^2\lambda^2}{2k\cdot p'} \left(2\pi\delta(k^2) n_B(|k^0|)\right) \Delta(l')\Delta(l'+k) \\ \left[\left(\overline{u}(p', m_f)\gamma_\mu \left(\not{k} + \not{p}' + m_f\right) P_R\, u(q, m_\chi)\right) (k - 2p + 2q')_\nu \right. \\ \left. \left(\overline{v}(q', m_\chi) P_L\, v(p, m_f)\right)\right] G^{\mu\nu}_k(p', p')\,. \qquad (4.22)\end{aligned}$$

Notice that the t-channel contribution in Eq. 4.17 contains the factor $G^{\mu\nu}_k(p', p)$ while the u-channel contribution in Eq. 4.22 contains the factor $G^{\mu\nu}_k(p', p')$. This is because of the definition of the p' and p legs which are different for t- and u-channel diagrams since the hard vertex V is kept fixed as the vertex where the momentum q' enters the graph. (Hence the p' leg includes just the final state fermion line for the t-channel but includes both the final state fermion and the scalar line for the u-channel case; see Fig. 4.1.)

Then the total NLO contribution from (the t-, u and cross tu channels of) Diagram 1,

Fig. 4.2, with thermal G photon propagator, is given by,

$$\begin{aligned}
Int^{tt+uu-tu}_{\text{Diagram}\,1,G\gamma} &= \frac{64\pi e^2\lambda^4}{3m_\phi^6 P}\Big[24H^4P - 6H^2m_\chi^2P - 6m_\chi^2P\left(m_f^2+3P^2\right) + 8Q^2P^3 \\
&\qquad + \log\frac{H-P}{H+P}\left(6H^5 + H^3\left(6\left(Q^2+P^2\right) - 3m_\chi^2\right) + 3HP^2\left(2Q^2 - 3m_\chi^2\right)\right)\Big]\ , \\
&= \frac{64\pi e^2\lambda^4}{3m_\phi^6 P}\Big[4P\left(8H^4 - 2\,H^2\left(4m_\chi^2+m_f^2\right) + 5m_\chi^2m_f^2\right) \\
&\qquad + 3\log\frac{H-P}{H+P}\left(8H^5 - 4H^3\left(2m_\chi^2+m_f^2\right) + 5Hm_\chi^2m_f^2\right)\Big]\ , \\
&\xrightarrow{\text{non-coll}} \frac{256\pi e^2\lambda^4}{3m_\phi^6}\left(8H^4 - 2\,H^2\left(4m_\chi^2+m_f^2\right) + 5m_\chi^2m_f^2\right)\ ,
\end{aligned} \tag{4.23}$$

where we have substituted for $P^2 = H^2 - m_f^2$, $Q^2 = H^2 - m_\chi^2$ and dropped the collinear logarithmic terms in the last line (and will discuss them in the next Chapter). It can be seen that $Int^{tt+uu-tu}_{\text{Diagram}\,1,G\gamma}$ given in Eq. 4.23 is independent of ω; hence the final contribution from thermal photons to Diagram 1, Fig. 4.2 is

$$\begin{aligned}
\sigma^{tt+uu-tu}_{NLO}(\text{Diagram}\,1, G\gamma) &= \frac{1}{32s(2\pi)^4}\,\frac{P}{Q}\int \omega\,\mathrm{d}\omega\, n_B(\omega)\, Int^{tt+uu-tu}_{\text{Diagram}\,1,G\gamma}\ , \\
&= \frac{1}{32s(2\pi)^4}\,\frac{P}{Q}\,\frac{\pi^2T^2}{6} \times Int^{tt+uu-tu}_{\text{Diagram}\,1,G\gamma}\ ,
\end{aligned} \tag{4.24}$$

which is not only IR finite, as guaranteed by the Grammer and Yennie technique, but has a T^2 temperature dependence of the cross section due to the ω-independence of $Int^{tt+uu-tu}_{\text{Diagram}\,1,\gamma}$, with

$$\int_0^\infty \omega\,\mathrm{d}\omega\, n_B(\omega) = \frac{\pi^2T^2}{6}\ . \tag{4.25}$$

We now discuss the contribution at NLO from Diagram 1, Fig. 4.2, when the fermion propagator is thermal. We will see that not only this, but each contribution from the various Diagrams in Fig. 4.2 are IR finite, as a result of applying the Grammer and Yennie technique.

A similar calculation can be performed when the virtual photon that is inserted is instead a K thermal photon. Then the factor $G_k^{\mu\nu}(p', p)$ ($G_k^{\mu\nu}(p', p')$ in Eq. 4.17 (Eq. 4.22) is replaced by $K_k^{\mu\nu}(p', p)$ ($K_k^{\mu\nu}(p', p')$) respectively. We have, for the t-, u- and cross tu-channel contributions,

$$\begin{aligned}
&\mathcal{M}^t_{NLO}(\text{Diagram 1}, K\gamma) = 0 \, , \\
&\mathcal{M}^u_{NLO}(\text{Diagram 1}, K\gamma) = 0 \, , \\
&\mathcal{M}^{tu}_{NLO}(\text{Diagram 1}, K\gamma) = 0 \, . \qquad (4.26)
\end{aligned}$$

In each case, it turns out that cancellations occur between the contributions of F_+ and F_- so that the total contribution vanishes.

4.2.1.2 NLO thermal fermion contributions to Diagram 1

As mentioned earlier, the thermal contributions from Diagram 1 only arise when either the photon or fermion propagator is thermal, that is, the explicitly T-dependent second term of the propagators in Eqs. 2.21 and 2.22 contribute; the contribution when both are thermal vanishes. We now consider the contribution at NLO of the t-channel Diagram 1, Fig. 4.2, when the photon propagator is non-thermal, but the fermion propagator is thermal. Recall that only the photon contributions give rise to IR divergences (both at $T = 0$ and finite temperature). This is because of their differing thermal distributions; see Eqs. 2.19 and 2.23. In addition, we have shown in Section 3.2.1.2 that the K-photon contribution when the photon is inserted into a thermal fermion vanishes; see Eq. 3.17. Hence in the G photon insertion, which arises from $G^{\mu\nu} = (g^{\mu\nu} - b_k k^\mu k^\nu)$, the second term, which is the K photon piece, vanishes and we therefore need consider just the $g^{\mu\nu}$ contribution (or in other words, since the K contribution vanishes, the G term contains the entire $g^{\mu\nu}$ contribution). The corresponding matrix element is then given by

$$
\begin{aligned}
\mathcal{M}^t_{NLO}(\text{Diagram } 1, f) = -\int \frac{\mathrm{d}^4 k}{(2\pi)^4} \frac{ie^2\lambda^2\, g^{\mu\nu}}{k^2} & \left(-2\pi\delta((p'+k)^2 - m_f^2) n_F(|(p'+k)^0|)\right) \\
& \Delta(l)\Delta(l+k)\left[\left(\overline{u}(p', m_f)\gamma_\mu \left(\not{k} + \not{p}' + m_f\right) P_R\, u(q', m_\chi)\right)\right. \\
& \left.(k + 2p' - 2q')_\nu \left(\overline{v}(q, m_\chi) P_L\, v(p, m_f)\right)\right] , \qquad (4.27)
\end{aligned}
$$

where n_F is the fermion number operator defined in Eq. 2.23, the $1/k^2$ term arises from the temperature-independent part of the photon propagator, and the delta-function from the thermal fermion propagator. As before, the index (Diagram 1, f) refers to the contribution arising from Diagram 1, Fig. 4.2, when the thermal part of the fermion propagator contributes. The sign difference in the definitions of n_F and n_B is what dictates the IR finite nature of the fermionic contributions. It is convenient to define $p' + k \equiv t$, and change the variable of integration to t, so that

$$
\begin{aligned}
\mathcal{M}^t_{NLO}(\text{Diagram } 1, f) = \int \frac{\mathrm{d}^4 t}{(2\pi)^4} \frac{ie^2\lambda^2}{2} \frac{g^{\mu\nu}}{m_f^2 - t\cdot p'} & \left(2\pi\delta(t^2 - m_f^2) n_F(|t^0|)\right) \\
& \Delta(l)\Delta(l+k)\left[\left(\overline{u}(p', m_f)\gamma_\mu \left(\not{t} + m_f\right) P_R\, u(q', m_\chi)\right)\right. \\
& \left.(t + p' - 2q')_\nu \left(\overline{v}(q, m_\chi) P_L\, v(p, m_f)\right)\right] , \qquad (4.28)
\end{aligned}
$$

so that the same simplification can be done using the delta-function as discussed in Eq. 4.19, to obtain

$$
\begin{aligned}
\int \mathrm{d}^4 t \left[2\pi\delta(t^2 - m_f^2)\right] F(t) &= 2\pi \int \mathrm{d}^4 t\, \delta(t_0^2 - |\vec{t}|^2 - m_f^2) F(t) \equiv 2\pi \int \mathrm{d}^4 t\, \delta(t_0^2 - \omega_t^2) F(t) , \\
&= \pi \int_{m_f}^{\infty} K_t\, \mathrm{d}\omega_t \left[\int \mathrm{d}\Omega_t F^f_+(\omega_t, K_t, \Omega_t) + \int \mathrm{d}\Omega_t F^f_-(-\omega_t, K_t, \Omega_t)\right],
\end{aligned}
\qquad (4.29)
$$

where $\omega_t^2 = |\vec{t}|^2 + m_f^2 \equiv K_t^2 + m_f^2$ and we have expressions for $F^f_\pm(t)$ analogous to that in Eq. 4.19. Then the thermal fermion contribution to the purely t-channel Diagram 1 is given analogously to that for thermal photons in Eq. 4.20 by

$$\begin{aligned}\sigma^t_{NLO}(\text{Diagram }1,f) &= \frac{1}{32\pi s(2\pi)^4}\frac{|\vec{p}'|}{|\vec{q}'|}\int \mathrm{d}\cos\theta\left[\sum_{spins}(\mathcal{M}^t_{LO})^\dagger\,\mathcal{M}^{t,1f}_{NLO}+h.c.\right],\\ &= \frac{1}{32s(2\pi)^4}\frac{|\vec{p}'|}{|\vec{q}'|}\int K_t\mathrm{d}\omega_t\,n_F(\omega_t)\left[\int\mathrm{d}\cos\theta\int\mathrm{d}\Omega_t\left[F^{t,1,f}_+ + F^{t,1,f}_-\right]\right],\\ &\equiv \frac{1}{32s(2\pi)^4}\frac{|\vec{p}'|}{|\vec{q}'|}\int K_t\mathrm{d}\omega_t\,n_F(\omega_t)Int^t_{\text{Diagram }1,f}\,. \end{aligned} \tag{4.30}$$

Again, on completing the angular integration, we find the t-channel thermal fermion contribution to Diagram 1, Fig. 4.2, to be

$$\begin{aligned}Int^t_{\text{Diagram }1,f} = \frac{32\pi e^2\lambda^4}{3K_t m_\phi^6 P}&\Big[4K_tP\left(3H^2m_\chi^2+Q^2\left(4H^2-m_f^2\right)\right)-\Big(6H^5\omega_t-3H^4m_f^2+\\ &H^3\omega_t\left(4Q^2-3m_f^2\right)-4H^2m_f^2Q^2-H\omega_tQ^2\left(m_f^2-2P^2\right)\\ &-m_f^2Q^2(P^2-m_f^2)\Big)\log\frac{H\omega_t+K_tP-m_f^2}{H\omega_t-K_tP-m_f^2}\\ &+\Big(6H^5\omega_t+3H^4m_f^2+H^3\omega_t\left(4Q^2-3m_f^2\right)+4H^2m_f^2Q^2-\\ &H\omega_tQ^2\left(m_f^2-2P^2\right)+\,m_f^2Q^2\left(P^2-m_f^2\right)\Big)\log\frac{H\omega_t-K_tP+m_f^2}{H\omega_t+K_tP+m_f^2}\Big]\,. \end{aligned}\tag{4.31}$$

While the non-logarithmic terms are (as in the case of thermal photons) independent of ω_t, the logarithmic terms have a complicated dependence on ω_t through K_t and it is not possible to analytically integrate these terms. A simplification is achieved in the limit that the fermion masses can be neglected in comparison to ω_t, so that $K_t \to \omega_t$. Then the contribution simplifies[2] to

$$\begin{aligned}Int^t_{\text{Diagram }1,f} \xrightarrow{K_t\to\omega_t} \frac{64\pi e^2H\lambda^4}{3{m_\phi}^6P}&\Big[2HP\left(3{m_\chi}^2+4Q^2\right)\\ &-2\left(3H^4+2H^2Q^2+Q^2P^2\right)\log\frac{H+P}{H-P}\Big]\,, \end{aligned}\tag{4.32}$$

---

[2] Note that no approximations have been made in the non-logarithmic term.

with

$$\frac{\log[H\omega_t + K_t P \pm m_f^2]}{\log[H\omega_t - K_t P \pm m_f^2]} \xrightarrow{K_t \to \omega_t} \frac{\log[H + P]}{\log[H - P]} \,, \tag{4.33}$$

where we have dropped terms of order $O(m_f^2/(H\omega_t))$, so that these logarithmic terms are of the same form as before, independent of ω_t, yielding again a T^2 temperature dependence from this contribution, using[3]

$$\int_{m_f}^{\infty} K_t \mathrm{d}\omega_t \, n_F(\omega_t) \approx \int_0^{\infty} \omega_t \mathrm{d}\omega_t \, n_F(\omega_t) = \frac{\pi^2 T^2}{12} \,. \tag{4.34}$$

In the next chapter, we will discuss the logarithmic collinearly divergent terms in more detail.

Similarly, the u-channel matrix element for thermal fermions is given by:

$$\begin{aligned} \mathcal{M}^u_{NLO}(\text{Diagram 1}, f) = - \int \frac{\mathrm{d}^4 t}{(2\pi)^4} \frac{i e^2 \lambda^2 g^{\mu\nu}}{2(m_f^2 - t \cdot p')} & \left(-2\pi\delta(t^2 - m_f^2) n_F(|t^0|)\right) \\ \Delta(l')\Delta(l' + k) & \Big[\left(\overline{u}(p', m_f)\gamma_\mu \left(\not{t} + m_f\right) P_R \, u(q, m_\chi)\right) \\ & (t + p' - 2q)_\nu \left(\overline{v}(q', m_\chi) P_L \, v(p, m_f)\right) \Big] \,. \end{aligned} \tag{4.35}$$

Using the LO matrix elements given in Eq. 4.3, the NLO matrix element for the t-channel contribution given in Eqs. 4.27 and 4.28 and that for the u-channel contribution in Eq. 4.35, the total thermal fermion contribution from Diagram 1, Fig. 4.2, that is, from

---

[3] Expanding $K_t = \sqrt{\omega_t^2 - m_f^2}$ as $K_t \approx \omega_t - m_f^2/(2\omega_t) + \cdots$ is not a possible choice since $\int (\mathrm{d}\omega_t/\omega_t) n_F$ is not convergent; it is of course possible to integrate this numerically if more precise results are required.

the combined t-channel, u-channel, and the crossed tu-channel, is found to be

$$
\begin{aligned}
Int^{tt+uu-tu}_{\text{Diagram}\,1,f} = \frac{32\pi e^2\lambda^4}{3m_\phi^6 K_t P}\Big[&4K_tP\left(3m_\chi^2 m_f^2 + 2Q^2(4H^2 - m_f^2)\right)\\
&+ 3m_\chi^2 \log\frac{H\omega_t + K_tP - m_f^2}{H\omega_t - K_tP - m_f^2}\left(3H^3\omega_t - 2H^2m_f^2 + H\omega_t(P^2 - 2m_f^2) + m_f^4 - P^2m_f^2\right)\\
&- 3m_\chi^2 \log\frac{H\omega_t + K_tP + m_f^2}{H\omega_t - K_tP + m_f^2}\left(3H^3\omega_t + 2H^2m_f^2 + H\omega_t(P^2 - 2m_f^2) - m_f^4 + P^2m_f^2\right)\\
&- 2\log\frac{H\omega_t + K_tP - m_f^2}{H\omega_t - K_tP - m_f^2}\Big(6H^5\omega_t - 3H^4m_f^2 + H^3\omega_t(4Q^2 - 3m_f^2) - 4H^2Q^2m_f^2\\
&\qquad -H\omega_tQ^2(m_f^2 - 2P^2) - Q^2m_f^2(P^2 - m_f^2)\Big)\\
&- 2\log\frac{H\omega_t + K_tP + m_f^2}{H\omega_t - K_tP + m_f^2}\Big(6H^5\omega_t + 3H^4m_f^2 + H^3\omega_t(4Q^2 - 3m_f^2) + 4H^2Q^2m_f^2\\
&\qquad -H\omega_tQ^2(m_f^2 - 2P^2) + Q^2m_f^2(P^2 - m_f^2)\Big)\Big]\ . \qquad (4.36)
\end{aligned}
$$

As in the case of the t-channel contribution alone, we can again use the approximation given in Eq. 4.33, so that

$$
\begin{aligned}
Int^{tt+uu-tu}_{\text{Diagram}\,1,f} \xrightarrow{K_t\to\omega_t} \frac{128\pi e^2\lambda^4}{3m_\phi^6}\Big[&\left(3m_\chi^2 m_f^2 + 2Q^2(4H^2 - m_f^2)\right) - \frac{3H}{2P}\log\frac{H+P}{H-P}\Big\{4H^4 +\\
&2H^2\left(8Q^2 - 2m_\chi^2 - m_f^2\right) + m_f^2\left(3m_\chi^2 - 2Q^2\right)\Big\}\Big]\ . \qquad (4.37)
\end{aligned}
$$

Again $Int_{NLO}^{1,tt+uu-tu,f}$ is independent of ω_t; hence, the ω_t integral (see Eq. 4.34) gives a T^2 temperature dependence to the cross section (analogue of Eq. 4.30 for all channels) from the thermal fermions in Diagram 1, Fig. 4.2, as well.

4.2.2 Thermal contribution to the cross section from Diagrams 1–3

Now that we have demonstrated details of the calculation of the cross section from Diagram 1, Fig. 4.2, we present the detailed results from all Diagrams in Fig. 4.2. The cross sections at NLO are defined analogous to Eq. 4.16. Diagram 3 is similar to Diagram 1;

here also, it is clear from an analysis similar to that for Diagram 1 in Section 4.2.1 that only one of the photon and fermion propagators can be thermal at a time. Diagram 2 has three propagators (excluding that of the scalar) and can in principle have contributions from any one, any two, or all three propagators being thermal (where by thermal we mean the contribution from the explicitly T-dependent second term in the expressions for the photon and fermion propagators given in Eqs. 2.21 and 2.22). As argued for Diagrams 1 and 3, there is no consistent available kinematic phase space when the photon propagator and either one of the fermion or anti-fermion propagators are both thermal. Hence there is no contribution from the case when all three propagators in Diagram 2 are thermal (all three propagators contribute on-shell) as well as when the photon propagator and either the fermion or anti-fermion propagator is thermal. In the case when the fermion and anti-fermion propagators are thermal, but not the photon one, we find that the delta function constraint $\delta((p'+k)^2 - m_f^2)\delta((p-k)^2 - m_f^2)$ is satisfied for the single phase space point, $k^0 = 0$. Therefore, for all the diagrams, as long as we discard the negligible contribution from scalar thermal propagators, we only have thermal contributions when exactly one of the propagators in the diagram is thermal and the others contribute through their non-thermal or temperature-independent parts. In addition, all vertices are of type-1 only, as was the case for Diagram 1.

4.2.2.1 Thermal photon contributions

The NLO matrix elements for the Diagrams 2 and 3 in Fig. 4.2, when the thermal part of the G photon propagator is taken into account are analogous to the expression given in Eq. 4.20 and are given by

$$\begin{aligned}\mathcal{M}^t_{NLO}(\text{Diagram}\,2, G\gamma) = \int \frac{\mathrm{d}^4k}{(2\pi)^4}\frac{ie^2\lambda^2}{4k\cdot p'k\cdot p}&\left(2\pi\delta(k^2)n_B(|k^0|)\right)(i\Delta(l+k))\\ &\left[\left(\bar{u}(p',m_f)\gamma_\mu\left(\not{k}+\not{p}'+m_f\right)P_R\,u(q',m_\chi)\right)\right.\\ &\left.\left(\bar{v}(q,m_\chi)P_L\left(\not{k}-\not{p}+m_f\right)\gamma_\nu\,v(p,m_f)\right)\right]G^{\mu\nu}_k(p',p)\,,\end{aligned} \tag{4.38}$$

$$
\begin{aligned}
\mathcal{M}^t_{NLO}(\text{Diagram}\,3, G\gamma) = \int \frac{\mathrm{d}^4k}{(2\pi)^4}\, \frac{ie^2\lambda^2}{2k\cdot p} &\left(2\pi\delta(k^2) n_B(|k^0|)\right) \Delta(l)\Delta(l+k) \\
&\left[\left(\bar{u}(p', m_f) P_R\, u(q', m_\chi)\right)(k - 2p + 2q)_\mu\right. \\
&\left.\left(\bar{v}(q, m_\chi) P_L \left(\not{k} - \not{p} + m_f\right)\gamma_\nu\, v(p, m_f)\right)\right] G_k^{\mu\nu}(p,p)\,, \qquad (4.39)
\end{aligned}
$$

for the t-channel, and appropriately crossed ones for the u-channel, for example, as shown in Eq. 4.22 for the contribution from the first diagram.

Combining all contributions from t-, u-, and cross tu-channels, the corresponding contributions from Diagrams 2 and 3 to the cross section in the heavy scalar limit (corresponding to Eqs. 4.20, 4.23, 4.24 from Diagram 1) are given, for the thermal photon case, by

$$
Int^{tt+uu-tu}_{\text{Diagram}\,2,G\gamma} = \frac{64\pi e^2\lambda^4}{3m_\phi^4}\left[\left(6H^2 - 6m_\chi^2 + 2Q^2\right) + \frac{1}{HP}\log\frac{H-P}{H+P}\left(3H^2 - Q^2\right)\left(H^2 - P^2\right)\right], \qquad (4.40)
$$

$$
\begin{aligned}
Int^{tt+uu-tu}_{\text{Diagram}\,3,G\gamma} = \frac{64\pi e^2\lambda^4}{3m_\phi^6 P} &\left[2P\left(6H^4 + H^2\left(8Q^2 - 3m_\chi^2\right) + \left(3m_\chi^2 - 2Q^2\right)\left(m_f^2 - P^2\right)\right)\right. \\
&+ H\log\frac{H-P}{H+P}\left(12H^4 + H^2\left(-9m_\chi^2 - 6m_f^2 + 8Q^2\right)\right. \\
&\left.\left. + m_\chi^2\left(6m_f^2 - 3P^2\right) - 2P^2\left(m_f^2 - 2P^2\right)\right)\right]. \qquad (4.41)
\end{aligned}
$$

The K photon contributions can be similarly calculated; we will simply tabulate them for later reference; see Table 4.1. In all tables that follow, we have re-defined $(Int^{G\gamma}_{i,j})' \equiv \omega(P/\sqrt{s})Int^{G\gamma}_{i,j}$ where $Int^{G\gamma}_{i,j}$ has been defined in the expression for the cross section in Eq. 4.20; we do this in order to have common overall factors in the virtual and real photon contributions, the latter of which we will compute in the next chapter. A similar definition holds for $(Int^{K\gamma}_{i,j})'$, etc. In addition, in all the tables, we have listed only the s-wave contribution corresponding to $Q, v = 0$. Note that the K-photon contribution has the ω dependence, $n_B(\omega)/\omega$, which leads to linear divergences in the IR. It appears that the

Diagrams 1–3 from Fig. 4.2 are IR finite; however, this is because the K photon contributions in all these cases are simultaneously also collinearly divergent and we have dropped such terms for now. We will discuss them later. We have also added a new definition of the contributions in terms of "Diagram (i, j)". Such a re-labelling helps to make the virtual–real photon correspondence explicit and ease the demonstration of cancellation of IR and collinear divergences in the next chapter. The power of the Grammer and Yennie technique is that the IR divergent pieces collected in the K photon terms cancel between virtual and real photon contributions at the integrand level itself. However, it will turn out that the collinear divergences do not factor out so easily. Again, we will discuss this in detail later. Henceforth, we shall simply list the soft IR divergent and log terms and discuss them in the next chapter.

Diagram	Diagram (i, j)	$(Int^{G\gamma}_{i,j})'$	$(Int^{K\gamma}_{i,j})'$
$1, t$	$1, 2$	$\omega\frac{64m_\chi^2(2m_\chi^2-m_f^2)}{m_\phi^6}$	0
$2, t$	$1, 3$	$\omega\frac{16(2m_\chi^2-m_f^2)}{m_\phi^4}$	0
$3, t$	$2, 3$	$\omega\frac{64m_\chi^2(2m_\chi^2-m_f^2)}{m_\phi^6}$	0
$1, u$	$4, 5$	$\omega\frac{64m_\chi^2(2m_\chi^2-m_f^2)}{m_\phi^6}$	0
$2, u$	$4, 6$	$\omega\frac{16(2m_\chi^2-m_f^2)}{m_\phi^4}$	0
$3, u$	$5, 6$	$\omega\frac{64m_\chi^2(2m_\chi^2-m_f^2)}{m_\phi^6}$	0
$1, tu$	$1, 5 + 2, 4$	$\omega\frac{256m_\chi^2\left(m_\chi^2-m_f^2\right)}{m_\phi^6}$	0
$2, tu$	$1, 6 + 3, 4$	$\omega\frac{32\left(2m_\chi^2-m_f^2\right)}{m_\phi^4}$	0
$3, tu$	$2, 6 + 3, 5$	$\omega\frac{256m_\chi^2\left(m_\chi^2-m_f^2\right)}{m_\phi^6}$	0

Table 4.1: *Thermal virtual photon contributions from G and K for all Diagrams 1–3 as shown in Fig. 4.2. Here* $(Int^{G\gamma}_{i,j})' \equiv \omega(P/\sqrt{s})Int^{G\gamma}_{i,j}$ *where* $Int^{G\gamma}_{i,j}$ *has been defined in Eq. 4.20;* $Int^{K\gamma}_{i,j}$ *has an analogous definition. The second column re-labels the diagrams for ease of comparison with the real photon contributions; these are defined and discussed in the next chapter. Note that the collinear divergences have not been included and are separately discussed.*

4.2.2.2 Thermal fermion contributions

The matrix elements for the case when the fermion (or anti-fermion) is thermal arise from Diagrams 1 and 2 (and 2 and 3). Again, these are IR finite and hence the entire photon (non-thermal) propagator is used. Replacing $k \to t = p' + k$ for the thermal fermion case as described in Eq. 4.28, and $k \to t = p - k$ for the thermal anti-fermions, we have

$$\begin{aligned} \mathcal{M}^t_{NLO}(\text{Diagram}\,2, f) = \int \frac{\mathrm{d}^4 t}{(2\pi)^4} & \frac{i e^2 \lambda^2 \, g^{\mu\nu}}{4(m_f^2 - p' \cdot t)\,(p \cdot p' + m_f^2 - t \cdot (p + p'))} \\ & \left(-2\pi\delta(t^2 - m_f^2) n_F(|t^0|)\right) i\Delta(l + k) \left[\left(\overline{u}(p', m_f)\gamma_\mu \left(\not{t} + m_f\right)\right.\right. \\ & \left.\left. P_R \, u(q', m_\chi)\right) \left(\overline{v}(q, m_\chi) P_L \left(\not{t} - \not{p}' - \not{p}\right) \gamma_\nu v(p, m_f)\right)\right] , \end{aligned} \tag{4.42}$$

$$\begin{aligned} \mathcal{M}^t_{NLO}(\text{Diagram}\,2, \overline{f}) = \int \frac{\mathrm{d}^4 t}{(2\pi)^4} & \frac{i e^2 \lambda^2 \, g^{\mu\nu}}{4(m_f^2 - p \cdot t)\,(p \cdot p' + m_f^2 - t \cdot (p + p'))} \\ & \left(-2\pi\delta(t^2 - m_f^2) n_F(|t^0|)\right) i\Delta(l + k) \left[\left(\overline{u}(p', m_f)\gamma_\mu \left(-\not{t} + \not{p}' + \not{p} + m_f\right)\right.\right. \\ & \left.\left. P_R \, u(q', m_\chi)\right) \left(\overline{v}(q, m_\chi) P_L \left(-\not{t} + m_f\right) \gamma_\nu v(p, m_f)\right)\right] , \end{aligned} \tag{4.43}$$

$$\begin{aligned} \mathcal{M}^t_{NLO}(\text{Diagram}\,3, \overline{f}) = \int \frac{\mathrm{d}^4 t}{(2\pi)^4} \frac{i e^2 \lambda^2 \, g^{\mu\nu}}{2(m_f^2 - t \cdot p)} & \left(-2\pi\delta(t^2 - m_f^2) n_F(|t^0|)\right) \Delta(l)\Delta(l + k) \\ & \left[\left(\overline{u}(p', m_f) P_R \, u(q', m_\chi)\right) (-t - p + 2q)_\mu \right. \\ & \left. \left(\overline{v}(q, m_\chi) P_L \left(-\not{t} + m_f\right) v(p, m_f)\right)\right] . \end{aligned} \tag{4.44}$$

Here f corresponds to the fermion being thermal in Diagram 2 and $\overline{f}$ corresponds to the anti-fermion being thermal in Diagrams 2 and 3 respectively. We use the same replacement technique here as explained in Eqs. 4.28 and 4.29 for the thermal fermion contribution to Diagram 1. For the matrix element of Diagram 2, we have substituted $t = p' + k$ as for Diagram 1; and we have substituted $t = p - k$ when the anti-fermion is thermal. Analogous expressions hold for the u-channel matrix elements.

The contributions to the NLO cross section from the thermal fermion or anti-fermion terms are given by (where we have substituted for P and dropped the logarithmic terms which have the same form as for Diagram 1),

$$
\begin{aligned}
Int^{tt+uu-tu}_{\text{Diagram}\,2,f} &= -\frac{32\pi e^2\lambda^4}{3m_\phi^4\left(H^2-\omega_t^2\right)}\left(12H^2(H^2-m_\chi^2)+4H^2Q^2+2\omega_t^2(3(H^2-m_\chi^2)+Q^2)\right)\,, \\
Int^{tt+uu-tu}_{\text{Diagram}\,2,\bar{f}} &= Int^{tt+uu-tu}_{\text{Diagram}\,2,f}\,, \\
Int^{tt+uu-tu}_{\text{Diagram}\,3,\bar{f}} &= \frac{128\pi e^2\lambda^4}{3m_\phi^6}\left(3m_\chi^2m_f^2+2Q^2(4H^2-m_f^2)\right)\,. \qquad (4.45)
\end{aligned}
$$

Notice that the contribution of the thermal fermion from Diagram 3 is the same as that from Diagram 1, as can be seen[4] from Eq. 4.37. Furthermore, the contribution of the thermal fermion from Diagram 2, Fig. 4.2, has non-trivial ω_t dependences both in the numerator and denominator. Recognising that large values of ω_t will lead to vanishing of the corresponding distribution function, $n_F(|\omega_t|)$, we expand the denominator for $\omega_t < H$ (recall that $H \geq m_\chi$ and $\beta m_\chi = x \sim 20$ at freeze-out) to obtain the total thermal fermion contribution from Diagram 2 to be

$$
Int^{tt+uu-tu}_{\text{Diagram}\,2,f+\bar{f}} = -\frac{64\pi e^2\lambda^4}{3m_\phi^4H^2}\left(12H^2(H^2-m_\chi^2)+4H^2Q^2+6\omega_t^2(3(H^2-m_\chi^2)+Q^2)\right)\,. \qquad (4.46)
$$

The presence of the ω_t^2 terms in the numerator will lead to T^4 temperature dependence in the cross section[5]. The contributions from both thermal fermion and anti-fermion terms from Diagrams 1–3 of Fig. 4.2 in the s-wave limit are listed in Table 4.2.

4.2.3 Thermal contribution to the cross section from Diagrams 4–5

Note that Diagrams 4 and 5 in Fig. 4.3 have no fermion propagators and hence have only thermal photon contributions (since we are neglecting the thermal contribution from the

---

[4] Note the absence of odd powers of ω_t due to the symmetry explicit in Eq. 3.14.

[5] Since $H^2 - m_\chi^2 = Q^2$, both the ω_t^0 and the ω_t^2 terms are small in the non-relativistic limit.

Diagram	Diagram (i, j)	$(Int^{f}_{i,j})'$	$(Int^{\bar{f}}_{i,j})'$
$1, t$	$1, 2$	$\omega\frac{32m_\chi^2(2m_\chi^2-m_f^2)}{m_\phi^6}$	–
$2, t$	$1, 3$	$-\omega\frac{16(2m_\chi^2-m_f^2)}{m_\phi^4}$	$-\omega\frac{16(2m_\chi^2-m_f^2)}{m_\phi^4}$
$3, t$	$2, 3$	–	$\omega\frac{32m_\chi^2(2m_\chi^2-m_f^2)}{m_\phi^6}$
$1, u$	$4, 5$	$\omega\frac{32m_\chi^2(2m_\chi^2-m_f^2)}{m_\phi^6}$	–
$2, u$	$4, 6$	$-\omega\frac{16(2m_\chi^2-m_f^2)}{m_\phi^4}$	$-\omega\frac{16(2m_\chi^2-m_f^2)}{m_\phi^4}$
$3, u$	$5, 6$	–	$\omega\frac{32m_\chi^2(2m_\chi^2-m_f^2)}{m_\phi^6}$
$1, tu$	$1, 5 + 2, 4$	$\omega\frac{128m_\chi^2\left(m_\chi^2-m_f^2\right)}{m_\phi^6}$	–
$2, tu$	$1, 6 + 3, 4$	$-\omega\frac{32(2m_\chi^2-m_f^2)}{m_\phi^4}$	$-\omega\frac{32(2m_\chi^2-m_f^2)}{m_\phi^6}$
$3, tu$	$2, 6 + 3, 5$	–	$\frac{128m_\chi^2\left(m_\chi^2-m_f^2\right)}{m_\phi^6}$

Table 4.2: *Thermal fermion and anti-fermion contributions from Diagrams 1–3 in Fig. 4.2. All are finite; collinear terms have been suppressed.*

scalar propagator). In addition, as was pointed out in Ref. [126], these contributions are also IR finite. Moreover, the contribution from Diagram 4 is suppressed by several powers of the scalar propagator, as can be seen from the expressions below (where the collinear log terms have been dropped):

$$
\begin{aligned}
Int^{tt+uu-tu}_{\text{Diagram}\,4,G\gamma} &= \frac{512\pi e^2\lambda^4}{15m_\phi^8 P(H^2-P^2)}\Big[P\Big\{60H^8 - 30H^6\left(2m_\chi^2 - m_f^2 + 2P^2\right) \\
&\quad + 15H^4\left(m_\chi^4 - m_\chi^2\left(m_f^2 - 2P^2\right) + 2Q^2\left(3m_f^2 + 2P^2\right)\right) \\
&\quad - H^2\Big[5m_\chi^2\left(m_f^2\left(Q^2 + 3P^2\right) + 2P^2\left(Q^2 - 3P^2\right)\right) \\
&\quad +2Q^2\left(m_f^2\left(15P^2 - 4Q^2\right) + 30P^4\right)\Big] \\
&\quad -P^2\left(15m_\chi^4P^2 + 5m_\chi^2Q^2\left(m_f^2 - 2P^2\right) + 2m_f^2Q^4\right)\Big\}\Big] \; , \\
Int^{tt+uu-tu}_{\text{Diagram}\,5,G\gamma} &= \frac{512\pi e^2\lambda^4}{3m_\phi^6}\left(-6H^4 + 3H^2m_\chi^2 + P^2\left(3m_\chi^2 - 2Q^2\right)\right) \; . \qquad (4.47)
\end{aligned}
$$

Again, we tabulate the K thermal photon contributions and the collinear log terms, and discuss them in the next chapter; see Table 4.3 where the contributions have been listed in the s-wave limit. It can be seen that the K photon contributions are IR finite. However, these contributions were necessary to obtain the factorisation and subsequent exponentiation of the K photon contributions into the B term as described in the previous chapter; see Ref. [126].

Diagram	$(Int^G_{i,j})'$	$(Int^K_{i,j})'$
$4, t$	$\omega\frac{256m_\chi^4(2m_\chi^2-m_f^2)}{m_\phi^8}$	$-\omega\frac{128m_\chi^4(2m_\chi^2+m_f^2)}{m_\phi^8}$
$4, u$	$\omega\frac{256m_\chi^4(2m_\chi^2-m_f^2)}{m_\phi^8}$	$-\omega\frac{128m_\chi^4(2m_\chi^2+m_f^2)}{m_\phi^8}$
$4, tu$	$\omega\frac{1024m_\chi^4\left(m_\chi^2-m_f^2\right)}{m_\phi^8}$	$-\omega\frac{512m_\chi^6}{m_\phi^8}$
$5, t$	$-\omega\frac{128m_\chi^2(2m_\chi^2-m_f^2)}{m_\phi^6}$	0
$5, u$	$-\omega\frac{128m_\chi^2(2m_\chi^2-m_f^2)}{m_\phi^6}$	0
$5, tu$	$-\omega\frac{512m_\chi^2\left(m_\chi^2-m_f^2\right)}{m_\phi^6}$	0

Table 4.3: *Contributions from Diagrams 4–5 from Fig. 4.3 with thermal photons attached on the scalar line. Note that the K photon contributions are finite.*

Having computed all the contributions from the Diagrams 1–5 in Figs. 4.2 and 4.3, we now go on to consider the self-energy contributions from Fig. 4.4.

4.2.4 Thermal contribution to the cross section from Diagrams 6–7

We now consider the contributions from thermal corrections to fermion self-energy corrections shown in Diagrams 6–7 in Fig. 4.4. These are normally considered as NLO corrections to the LO diagrams in Fig. 4.1; in particular, through NLO corrections to the fermion (or anti-fermion) propagator (we neglect thermal effects for the heavy scalar). We have [94, 102] therefore three sources of thermal correction to the fermion propagator:

$$S^{NLO}(p) = Z_2^T \frac{\sum u_T^s(p)\overline{u}_T^s(p)}{p^2 - m_f^2 - \Delta m_T^2}\,, \tag{4.48}$$

with the fermion spin sum being thermally corrected to NLO as

$$\sum_s u_T^s(p)\overline{u}_T^s(p) = \not{p}(1 - \hat{C}_B) - \not{K}_B - \not{K}_F + m_f(1 - 2\hat{C}_B + 2\hat{C}_F)\,, \tag{4.49}$$

the (finite) wave function renormalisation at temperature T being given by

$$Z_2^T = (1 + \hat{C}_B - \hat{C}_F - 2m_f^2(\hat{C}'_B - \hat{C}'_F)) , \tag{4.50}$$

while the thermal mass correction is given by

$$\Delta m_T^2 = \delta m_B^2 + \delta m_F^2 + 2m_f^2 \hat{C}_F , \tag{4.51}$$

where the circumflex indicates that the various terms are to be computed on-shell at $p^2 = m_f^2$, and are given by

$$\begin{aligned} C_B &= \frac{2e^2}{(2\pi)^3} \int \mathrm{d}^4k \frac{\delta(k^2) n_B(|k^0|)}{(p+k)^2 - m_f^2} , \\ K_B^\mu &= \frac{2e^2}{(2\pi)^3} \int \mathrm{d}^4k \frac{\delta(k^2) n_B(|k^0|) k^\mu}{(p+k)^2 - m_f^2} , \\ \delta m_B^2 &= \frac{2e^2}{(2\pi)^3} \int \mathrm{d}^4k \delta(k^2) n_B(|k^0|) , \end{aligned} \tag{4.52}$$

for the thermal photon contributions, and

$$\begin{aligned} C_F &= \frac{2e^2}{(2\pi)^3} \int \mathrm{d}^4t \frac{\delta(t^2 - m_f^2) n_F(|t^0|)}{(p-t)^2} , \\ K_F^\mu &= -\frac{2e^2}{(2\pi)^3} \int \mathrm{d}^4t \frac{\delta(t^2 - m_f^2) n_F(|t^0|) t^\mu}{(p-t)^2} , \\ \delta m_F^2 &= \frac{2e^2}{(2\pi)^3} \int \mathrm{d}^4t \delta(t^2 - m_f^2) n_F(|t^0|) , \end{aligned} \tag{4.53}$$

for the thermal fermion contribution[6]. Here the terms are expanded around $p^2 = m_f^2$ as

$$C_{B,F} = \hat{C}_{B,F} + (p^2 - m_f^2)\hat{C}'_{B,F} . \tag{4.54}$$

Due to the presence of the delta function, it can be seen that the contribution in each of these cases again involves a sum of two functions as in Eqs. 4.19 and 4.29 for thermal

---

[6] We differ in the definition of K_F from that in Ref. [94] by a sign.

photons and fermions respectively.

The contributions to the thermal part of the virtual NLO annihilation cross section from the spinor spin sum, the wave function renormalisation and the mass corrections in Eqs. 4.49, 4.50 and 4.51 (in effect, the NLO thermal corrections arising from the contributions of the fermion self-energy diagram shown in Fig. 4.4, and an analogous contribution from the anti-fermion self-energy diagram shown in the same figure) are labelled by (B_1, B_2, B_3) and (F_1, F_2, F_3) for the *thermal photon* and *thermal fermion* contributions respectively. The total contribution is the sum of all six terms.

In order to determine the divergent K photon contribution (see Eq. 3.2), the thermal K photon virtual contribution from Diagram 6 (and similarly from Diagram 7) of Fig. 4.4 is calculated as per the definition in Eq. 4.15. A straightforward calculation of this term and comparison with the contributions listed above shows that this matches exactly with the B_2 contribution and contains within it all the soft IR divergences. (Since the fermions are known not to contribute to the IR divergence, F_2 is finite).

Hence the soft divergent parts are only contained in the term B_2 (and constitute the K photon contribution), while collinear divergences appear in the remaining terms. The (mass correction) contribution from B_3 and F_3 are incorporated as usual via

$$\begin{aligned} \delta\sigma &= \frac{\partial \sigma^{LO}}{\partial m_f^2} \Delta m^2 \, , \\ &\equiv B_3 + F_3 \, . \end{aligned} \tag{4.55}$$

Since σ^{LO} is analytic in m_f^2 as seen from Eq. 4.11, with no soft-divergences.

The total contribution to the cross section from the B_1 and B_3 thermal photon terms for the fermion, and from the F_1 and F_3 thermal fermion terms are given by

$$Int^{tt+uu-tu}_{\text{Diagram}\,6,G\gamma} = -\frac{32\pi e^2 \lambda^4}{3 m_\phi^4 (H^2 - m_f^2)} \left(6H^4 + H^2(2Q^2 - 6m_\chi^2) + m_f^2(3m_\chi^2 - 2Q^2) \right) \, , \tag{4.56}$$

$$Int^{tt+uu-tu}_{\text{Diagram}\,6,f} = -\frac{32\pi e^2\lambda^4}{3m_\phi^4(H^2 - m_f^2)}\left(6H^4 + H^2(2Q^2 - 6m_\chi^2) + m_f^2(3m_\chi^2 - 2Q^2)\right)\;; \qquad (4.57)$$

note that these appear identical to the thermal photon contributions but will differ in their contribution to the cross section due to the differing integrals in Eqs. 4.25 and 4.34 respectively. Identical contributions will hold when the anti-fermion is thermal (see Diagram 7 of Fig. 4.4). As usual, we list the K photon contribution in the s-wave limit in Table 4.4 and discuss them in the next chapter. Note that the self-energy G photon contributions, *viz.*, $(1,1), (3,3), (4,4), (6,6), (1,4)$ and $(3,6)$, are a sum of the B_1 and B_3 terms, while the corresponding K photon contributions arise from the B_2 term.

Diagram	Diagram (i, j)	$(Int^{G\gamma}_{i,j})'$	$(Int^{K\gamma}_{i,j})'$
$6, t$	$1, 1$	$-\omega\frac{8m_\chi^2(2m_\chi^2-m_f^2)}{m_\phi^4(m_\chi^2-m_f^2)}$	$\frac{m_\chi^2(32m_\chi^2-8m_f^2)}{\omega m_\phi^4}$
$7, t$	$3, 3$	$-\omega\frac{8m_\chi^2(2m_\chi^2-m_f^2)}{m_\phi^4(m_\chi^2-m_f^2)}$	$\frac{m_\chi^2(32m_\chi^2-8m_f^2)}{\omega m_\phi^4}$
$6, u$	$4, 4$	$-\omega\frac{8m_\chi^2(2m_\chi^2-m_f^2)}{m_\phi^4(m_\chi^2-m_f^2)}$	$\frac{m_\chi^2(32m_\chi^2-8m_f^2)}{\omega m_\phi^4}$
$7, u$	$6, 6$	$-\omega\frac{8m_\chi^2(2m_\chi^2-m_f^2)}{m_\phi^4(m_\chi^2-m_f^2)}$	$\frac{m_\chi^2(32m_\chi^2-8m_f^2)}{\omega m_\phi^4}$
$6, tu$	$1, 4$	$-\omega\frac{32m_\chi^2}{m_\phi^4}$	$\frac{16m_\chi^2(64m_\chi^2-48m_f^2)}{\omega m_\phi^4}$
$7, tu$	$3, 6$	$-\omega\frac{32m_\chi^2}{m_\phi^4}$	$\frac{16m_\chi^2(64m_\chi^2-48m_f^2)}{\omega m_\phi^4}$

Table 4.4: *As in Table 4.1 for the thermal photon contributions to the fermion self energy diagrams shown in Fig. 4.4. Note that all K photon contributions are linearly divergent.*

The thermal fermion contributions in the s-wave limit are listed in Table 4.5. Again, these are finite and hence the contributions shown are the sum of the $F_1 + F_3$ terms. Note that the collinear divergent terms have not been included here and will be discussed in the next chapter.

We have now computed all possible thermal virtual photon corrections at NLO to the dark matter annihilation cross section, $\chi\chi \to f\overline{f}$. In the next chapter, we will discuss the soft and collinear divergences that occur in the problem, and show how they cancel against similar contributions from thermal real photon processes involving $\chi\chi \to f\overline{f}(\gamma)$. Here (γ) indicates that the photon can be both emitted into, and absorbed from, the heat

Diagram	Diagram (i, j)	$(Int^{f}_{i,j})'$	$(Int^{\overline{f}}_{i,j})'$
$6, t$	$1, 1$	$-\omega \frac{8m_\chi^2(2m_\chi^2 - m_f^2)}{m_\phi^4(m_\chi^2 - m_f^2)}$	0
$7, t$	$3, 3$	–	$-\omega \frac{8m_\chi^2(2m_\chi^2 - m_f^2)}{m_\phi^4(m_\chi^2 - m_f^2)}$
$6, u$	$4, 4$	0	$-\omega \frac{8m_\chi^2(2m_\chi^2 - m_f^2)}{m_\phi^4(m_\chi^2 - m_f^2)}$
$7, u$	$6, 6$	$-\omega \frac{8m_\chi^2(2m_\chi^2 - m_f^2)}{m_\phi^4(m_\chi^2 - m_f^2)}$	0
$6, tu$	$1, 4$	$-\omega \frac{32m_\chi^2}{m_\phi^4}$	0
$7, tu$	$3, 6$	0	$-\omega \frac{32m_\chi^2}{m_\phi^4}$

Table 4.5: *As in Table 4.1 for the thermal fermion contributions to the fermion self energy diagrams shown in Fig. 4.4.*

bath at temperature T. For now, we will simply list the finite remainder, and discuss the cancellation of the divergences later.

4.3 Total thermal NLO contributions to the cross section

The thermal virtual contribution at NLO is given by the sum of the thermal photon, thermal fermion, and thermal anti-fermion contributions. Since the thermal contribution is already at order $O(T^2)$, we compute only the s-wave terms since the p-wave ones contribute one more power of temperature to the collision term; see Eq. 4.14; hence, the s-wave terms have the most significant contribution at freeze-out when $m_\chi/T \sim 20$. The full expressions are available on-line as Mathematica files in Ref. [134].

It is clear that Diagrams 2, 6, and 7 from Figs. 4.2 and 4.4 contribute at order $O(1/m_\phi^4)$ in the scalar mass while Diagrams 1, 3 (from Fig. 4.2), and 5 (from Fig. 4.3) contribute at order $O(1/m_\phi^6)$ while Diagram 4 (from Fig. 4.3) is highly suppressed, at order $O(1/m_\phi^8)$.

Although we show the cancellation of the soft IR and collinear divergences in the next chapter, here we will assume the cancellation and go on to compute the finite remainder. The finite total invariant NLO cross section is then given by the sum of the thermal photon (both finite G and finite part of the K photon terms) and thermal fermion and anti-fermion contributions[7],

$$\begin{aligned}\sigma_{NLO}^{Virtual}(s\text{-wave}) &= \frac{1}{32s(2\pi)^4}\,\frac{P}{Q}\left[\int \omega\,\mathrm{d}\omega\, n_B Int_{1-7,\gamma}^{tt+uu-tu} + \int K_t\,\mathrm{d}\omega_t\, n_F Int_{1-7,(f+\bar{f})}^{tt+uu-tu}\right],\\ &= \frac{\alpha\lambda^4}{128}\,\frac{m_f^2 T^2}{\sqrt{s}Q}\left[-\frac{8}{m_\phi^4}+\frac{32m_\chi^2}{3m_\phi^6}+\frac{128m_\chi^4}{3m_\phi^8}\right]+\mathcal{O}(v^2)\,,\\ &= \frac{\alpha\lambda^4}{128}\,\frac{m_f^2 T^2}{m_\chi^2 v_{rel}}\left[-\frac{8}{m_\phi^4}+\frac{32m_\chi^2}{3m_\phi^6}+\frac{128m_\chi^4}{3m_\phi^8}\right]+\mathcal{O}(v^2)\,,\end{aligned} \tag{4.58}$$

where we have used $\alpha = e^2/(4\pi)$. The NLO virtual thermal cross section was computed in Ref. [131]; the leading NLO contribution was also calculated earlier by Ref. [94] who explicitly showed the cancellation of soft and collinear divergences at NLO. The NLO thermal cross section was found to vanish in Ref. [94] in the massless limit; this was subsequently explained by them using the Operator Product Expansion approach in Ref. [135] where the cross section for annihilation of Dirac-type dark matter particles was also computed. In our work, we have used the heavy scalar approximation to compute not just the leading $1/m_\phi^4$ contribution, but the $1/m_\phi^6$ and $1/m_\phi^8$ contributions as well. Also, we have used the GY technique to directly calculate the IR finite G photon contribution which greatly simplifies the calculation, leaving only type-1 thermal vertices. However, the Grammer and Yennie technique does not effect a neat separation of collinear divergences. We will comment on this in the next chapter.

Notice the factor m_f^2 in all terms due to helicity suppression of the Majorana dark matter annihilation channel; in contrast, we see below that the Dirac dark matter annihilation cross section (purely t-channel contribution) is not helicity suppressed:

$$\begin{aligned}\sigma_{NLO}^{Dirac,Virtual}(s\text{-wave}) = \frac{\alpha\lambda^4}{128v_{rel}}\,\frac{T^2}{m_\chi^2}\Bigg[&-\frac{4(2m_\chi^2+m_f^2)}{m_\phi^4}+\frac{16m_\chi^2(2m_\chi^2-m_f^2)}{3m_\phi^6}\\ &+\frac{64m_\chi^4(2m_\chi^2-3m_f^2)}{3m_\phi^8}\Bigg]+\mathcal{O}(v^2)\,.\end{aligned} \tag{4.59}$$

---

[7] Here γ denotes the sum of the *finite* contributions from G and K terms. Note that only Diagram 4 of Fig. 4.3 contributes to the finite part of the K photon term.

It can be seen that the NLO cross section for Majorana DM is proportional to m_f^2 as $v \to 0$, just as the LO cross section; see Eq. 4.8. This can be understood from helicity conservation: just as in the LO case, the NLO diagrams (with an additional virtual photon) that we have computed are planar $2 \to 2$ processes. The Majorana coupling then forces the final states into the "wrong" chirality so that the cross section is proportional to the fermion mass squared. At early times in the evolution of the Universe, the dark matter particles are relativistic, $\sqrt{s}$ can be large, and there is less suppression in the annihilation into the lighter fermions. This also holds for freeze-in scenarios where $m_\chi/T \sim \mathcal{O}(1)$.

4.4 Collinear divergences

So far, we have not discussed the collinear divergences in detail. Some of the terms have been presented in the calculation of the thermal photon and thermal fermion contributions in Diagram 1 of Fig. 4.2; see Eqs. 4.23 and 4.36 in Section 4.2.1. It turns out that the collinear log terms do not cancel between the K virtual photon and $\widetilde{K}$ real photon contributions; instead, the cancellation occurs, diagram by diagram, between the *total* virtual and real contributions. This implies that the Grammer and Yennie technique, while factorising and isolating the soft IR divergences into the K (or $\widetilde{K}$) contributions, does not achieve the same factorisation for collinear terms. Hence, in what follows we use the sum of the G and K photon contributions to the collinear terms and compare this sum with the sum of the contributions from the real photon calculation that we will present in the next chapter.

There are three sets of contributing terms:

1. when the photon is thermal (both G and K photon terms) which has contributions from all Diagrams 1–7 in Figs. 4.2, 4.3 and 4.4,

2. when the fermion is thermal, with contributions from Diagrams 1, 2 and 6 in

Figs. 4.2 and 4.4, and

3. when the anti-fermion is thermal, with contributions from Diagrams 2, 3 and 7 in Figs. 4.2 and 4.4.

These are listed in Tables 4.6, 4.7, and 4.8 respectively. Since we will demonstrate the cancellation of these terms against the real photon contributions in the next chapter, we have used the (i, j) notation for the various terms; see any of the earlier tables for the correspondence between the (i, j) notation and the t-, u-, and tu-terms from Diagrams 1–7.

The collinear log term that arises in the thermal photon contributions is given by

$$L_V = \log\left[\frac{H-P}{H+P}\right] \approx \log\left[\frac{m_f^2}{4H^2-m_f^2}\right] \equiv L_\gamma \,, \tag{4.60}$$

where we define L_γ, the logarithmic term appearing in the thermal photon calculation, for future reference. As we have mentioned earlier, there are terms that are simultaneously soft IR divergent (proportional to $1/\omega$) as well as collinearly divergent (proportional to L_V). Obviously, the terms that are soft IR divergent only occur in the K photon terms; the G thermal photon, and the fermion and anti-fermion contributions are all soft IR finite, as expected.

For the virtual *thermal fermion* contribution we have the log terms L_{V_f} and L'_{V_f}, where

$$\begin{aligned} L_{V_f} &= \frac{1}{2}\left(\log\left[\frac{H\omega_t - K_tP - m_f^2}{H\omega_t + K_tP - m_f^2}\right] + \log\left[\frac{H\omega_t - K_tP + m_f^2}{H\omega_t + K_tP + m_f^2}\right]\right) \,, \\ L'_{V_f} &= \frac{1}{2}\left(\log\left[\frac{H\omega_t - K_tP - m_f^2}{H\omega_t + K_tP - m_f^2}\right] - \log\left[\frac{H\omega_t - K_tP + m_f^2}{H\omega_t + K_tP + m_f^2}\right]\right) \,. \end{aligned} \tag{4.61}$$

It can be seen that the coefficient of L'_{V_f} in all terms of Tables 4.7 and 4.8 is proportional to m_f^2 and hence this term vanishes in the collinear limit, $m_f \to 0$. Hence the collinear divergences are contained in L_V and L_{V_f} alone. Note that collinear divergent terms have

Diagram	**Thermal Photon Collinear Contributions**
(i, j)	$(Int_{i,j}^{G+K})'$ (Collinear terms)
$1, 1$	$\omega \frac{16m_\chi^2}{m_\phi^4} L_V$
$3, 3(= 1, 1)$	$\omega \frac{16m_\chi^2}{m_\phi^4} L_V$
$4, 4(= 1, 1)$	$\omega \frac{16m_\chi^2}{m_\phi^4} L_V$
$6, 6(= 1, 1)$	$\omega \frac{16m_\chi^2}{m_\phi^4} L_V$
$1, 2$	$\omega \frac{32m_\chi^2}{m_\phi^6} (2m_\chi^2 - m_f^2) L_V$
$1, 3$	$\frac{16m_\chi^2}{\omega m_\phi^4} (4m_\chi^2 - 2m_f^2) L_V + \omega \frac{16m_f^2}{m_\phi^4} L_V$
$1, 4$	$\omega \frac{32m_\chi^2}{m_\phi^4} L_V$
$1, 5 + 2, 4$	$\omega \frac{32m_\chi^2}{m_\phi^6} (4m_\chi^2 - 3m_f^2) L_V$
$1, 6 + 3, 4$	$\frac{32}{\omega m_\phi^4} (2m_\chi^2 - m_f^2)^2 L_V$
$2, 3$	$\omega \frac{32m_\chi^2}{m_\phi^6} (2m_\chi^2 - m_f^2) L_V$
$2, 6 + 3, 5$	$\omega \frac{32m_\chi^2}{m_\phi^6} (4m_\chi^2 - 3m_\chi^2) L_V$
$3, 6$	$\omega \frac{32m_\chi^2}{m_\phi^4} L_V$
$4, 5(= 1, 2)$	$\omega \frac{32m_\chi^2}{m_\phi^6} (2m_\chi^4 - m_\chi^2 m_f^2) L_V$
$4, 6(= 1, 3)$	$\frac{16m_\chi^2}{\omega m_\phi^4} (4m_\chi^2 - 2m_f^2) L_V + \omega \frac{16m_f^2}{m_\phi^4} L_V$
$5, 6(= 2, 3)$	$\omega \frac{32m_\chi^2}{m_\phi^6} (2m_\chi^2 - m_f^2) L_V$

Table 4.6: *Collinear divergences in various terms of the virtual* $K + G$ thermal photon *contributions. See text for the definition of the log term* L_V*. Contributions such as* $(1, 3)$ *(from Diagram 2) etc., have terms that are simultaneously soft and collinear divergent, having both linear divergence from the* $1/\omega$ *factor and the collinear log term,* L_V*.*

not been included here and will be discussed in the next chapter.

Diagram	**Thermal Fermion Collinear Contributions**
(i,j)	$(Int^f_{i,j})'$ (Collinear terms)
$1,1$	$\omega_t \frac{16m_\chi^2}{m_\phi^4} L_{V_f} - \frac{8m_\chi}{m_\phi^6}(4m_\chi^2 - m_f^2)L'_{V_f}$
$3,3$	0
$4,4(=1,1)$	$\omega_t \frac{16m_\chi^2}{m_\phi^4} L_{V_f} - \frac{8m_\chi}{m_\phi^6}(4m_\chi^2 - m_f^2)L'_{V_f}$
$6,6$	0
$1,2$	$\omega_t \frac{32m_\chi^2}{m_\phi^6}(2m_\chi^2 - m_f^2)L_{V_f} - \frac{32m_\chi}{m_\phi^6}(m_f^2)L'_{V_f}$
$1,3$	$-\omega_t \frac{8}{m_\phi^4}(4m_\chi^2 - 3m_f^2)L_{V_f} + \frac{8m_\chi}{m_\phi^4}(m_f^2)L'_{V_f}$
$1,4$	$\omega_t \frac{32m_\chi^2}{m_\phi^4} L_{V_f} - \frac{16m_\chi}{m_\phi^4}(4m_\chi^2 + m_f^2)L'_{V_f}$
$1,5+2,4$	$\omega_t \frac{32m_\chi^2}{m_\phi^6}(4m_\chi^2 - 3m_f^2)L_{V_f} - \frac{96m_\chi^3 m_f^2}{m_\phi^6} L'_{V_f}$
$1,6+3,4$	$-\omega_t \frac{16}{m_\chi^2 m_\phi^4}(2m_\chi^2 - m_f^2)^2 L_{V_f} + \frac{16m_f^2}{m_\chi m_\phi^4}(3m_\chi^2 - m_f^2)L'_{V_f}$
$2,3$	0
$2,6+3,5$	0
$3,6$	0
$4,5(=1,2)$	$\omega_t \frac{32m_\chi^2}{m_\phi^6}(2m_\chi^2 - m_f^2)L_{V_f} - \frac{32m_\chi}{m_\phi^6}(m_f^2)L'_{V_f}$
$4,6(=1,3)$	$-\omega_t \frac{8}{m_\phi^4}(4m_\chi^2 - 3m_f^2)L_{V_f} + \frac{8m_\chi}{m_\phi^4}(m_f^2)L'_{V_f}$
$5,6$	0

Table 4.7: *As in Table 4.6 for collinear divergences from* thermal virtual fermions. *See text for a definition of the log terms L_{V_f} and L'_{V_f}. Note that all contributions are soft-IR finite.*

Expanding the logarithms in Eq. 4.61, we have

$$\log\left[\frac{H\omega_t - K_tP - m_f^2}{H\omega_t + K_tP - m_f^2}\right] = \log\left[\frac{\omega_t - K_tP}{\omega_t + K_tP}\right] + \log[1 - \epsilon_{--}] - \log[1 - \epsilon_{-+}]\,,$$
$$\log\left[\frac{H\omega_t - K_tP + m_f^2}{H\omega_t + K_tP + m_f^2}\right] = \log\left[\frac{\omega_t - K_tP}{\omega_t + K_tP}\right] + \log[1 + \epsilon_{+-}] - \log[1 + \epsilon_{++}]\,, \qquad (4.62)$$

Diagram	**Thermal Anti-Fermion Collinear Contributions**
(i, j)	$(Int^{\overline{f}}_{i,j})'$ (Collinear terms)
$1, 1$	0
$3, 3$	$\omega_t \frac{16m_\chi^2}{m_\phi^4} L_{V_f} - \frac{8m_\chi}{m_\phi^4}(4m_\chi^2 + m_f^2) L'_{V_f}$
$4, 4$	0
$6, 6 (= 3, 3)$	$\omega_t \frac{16m_\chi^2}{m_\phi^4} L_{V_f} - \frac{8m_\chi}{m_\phi^4}(4m_\chi^2 + m_f^2) L'_{V_f}$
$1, 2$	0
$1, 3$	$-\omega_t \frac{8}{m_\phi^4}(4m_\chi^2 - 3m_f^2) L_{V_f} + \frac{8m_\chi}{m_\phi^4}(m_f^2) L'_{V_f}$
$1, 4$	0
$1, 5 + 2, 4$	0
$1, 6 + 3, 4$	$-\omega_t \frac{16}{m_\chi^2 m_\phi^4}(2m_\chi^2 - m_f^2)^2 L_{V_f} + \frac{48m_\chi}{m_\phi^4}(m_f^2) L'_{V_f}$
$2, 3$	$\omega_t \frac{32m_\chi^2}{m_\phi^6}(2m_\chi^2 - m_f^2) L_{V_f} - \frac{32m_\chi^3}{m_\phi^6}(m_f^2) L'_{V_f}$
$2, 6 + 3, 5$	$\omega_t \frac{32m_\chi^2}{m_\phi^6}(4m_\chi^2 - 3m_f^2) L_{V_f} - \frac{96m_\chi^3}{m_\phi^6}(m_f^2) L'_{V_f}$
$3, 6$	$\omega_t \frac{32m_\chi^2}{m_\phi^4} L_{V_f} - \frac{16m_\chi}{m_\phi^4}(4m_\chi^2 + m_f^2) L'_{V_f}$
$4, 5$	0
$4, 6 (= 1, 3)$	$-\omega_t \frac{8}{m_\phi^4}(4m_\chi^2 - 3m_f^2) L_{V_f} + \frac{8m_\chi}{m_\phi^4}(m_f^2) L'_{V_f}$
$5, 6 (= 2, 3)$	$\omega_t \frac{32m_\chi^2}{m_\phi^6}(2m_\chi^2 - m_f^2) L_{V_f} - \frac{32m_\chi^3}{m_\phi^6}(m_f^2) L'_{V_f}$

Table 4.8: *As in Table 4.7 for collinear divergences from* thermal anti-fermions.

where the ϵ_{ij} are small quantities, given to order $O(m_f^2)$ by

$$\begin{aligned}
\epsilon_{--} &= \frac{(\omega_t + K_t)(2H - \omega_t + \epsilon(4H - 3\omega_t)}{2H^2} \,, \\
\epsilon_{-+} &= \frac{(\omega_t - K_t)(2H - \omega_t + \epsilon(4H - 3\omega_t)}{2H^2} \,, \\
\epsilon_{+-} &= \frac{(\omega_t + K_t)(2H + \omega_t + \epsilon(4H + 3\omega_t)}{2H^2} \,, \\
\epsilon_{++} &= \frac{(\omega_t - K_t)(2H + \omega_t + \epsilon(4H + 3\omega_t)}{2H^2} \,,
\end{aligned} \tag{4.63}$$

where $\epsilon = m_f^2/(4H^2)$. Substituting, we get

$$\begin{aligned}
L_{V_f} &= \log\left[\frac{\omega_t - K_t P}{\omega_t + K_t P}\right] - \frac{4H^2 + m_f^2}{4H^4}\omega_t K_t \equiv L_f + O(\omega_t)^2 \,, \\
L'_{V_f} &= -\frac{6H^2 + m_f^2}{3H^3} K_t + O(\omega_t)^3 \,.
\end{aligned} \tag{4.64}$$

Notice that the collinear divergence is contained in the rather unusual term, L_f, the logarithmic term appearing in the thermal fermion calculations. We discuss these terms and their cancellation in the next chapter.

4.5 Additional virtual diagrams

Examiner[8] of thesis pointed out that there can be additional diagrams as shown in Fig. 4.5. We have computed the contributions from these diagrams. The s-wave contribution from Diagram 8 in Fig. 4.5 vanishes at both order $O(T^2)$ and order $O(T^4)$ for Majorana dark matter.

In the case of Dirac dark matter, the contribution from these diagrams is non-zero, but helicity suppressed at order $O(T^2)$ and is therefore a negligible addition to the result in Eq. 5.28. In either case, there can be no contribution from thermal photons since this will lead to the delta-function $\delta(s)$ which cannot be satisfied. Hence only thermal fermion and

---

[8] Thanks to Prof. Priyotosh Bandyopadhyay for pointing NLO correction due to scalar-fermion loop.

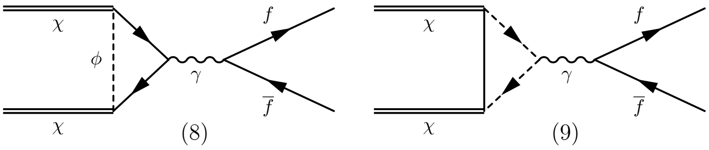

Figure 4.5: *Additional virtual photon t-channel diagrams that contribute to the dark matter annihilation cross section. Analogous u-channel diagrams also exist. See text for details.*

thermal anti-fermion contributions occur. We have

$$\begin{aligned}
\sigma_{NLO}^{\text{fig 8,Majorana}} &= 0\,, \\
\sigma_{NLO}^{\text{fig 9,Majorana}} &= 0\,, \\
\sigma_{NLO}^{\text{fig 8,Dirac}} &= \frac{\alpha|\lambda|^4}{128 v_{rel}}\frac{T^2}{m_\chi^2}\frac{8}{9m_\phi^4}\left[m_f^2 + \frac{7\pi^2}{10}\frac{T^2}{m_\chi^2}\left(2m_\chi^2 + m_f^2\right)\right]\;; \\
\sigma_{NLO}^{\text{fig 9,Dirac}} &= -\frac{\alpha|\lambda|^4}{128 v_{rel}}\frac{T^2}{m_\chi^2}\frac{16m_\chi^2}{9m_\phi^6}\left[m_f^2 - \frac{7\pi^2}{10}\frac{T^2}{m_\chi^2}\left(m_\chi^2\right)\right]\,. \qquad (4.65)
\end{aligned}$$

Thermal correction to annihilation cross section at $O(T^2)$ in Eq. 4.59 will be slightly modified due to additional processes in Fig. 4.5 for Dirac case and will be unaltered for Majorana DM,

$$\begin{aligned}
\sigma_{NLO}^{Dirac,Virtual}(s\text{-wave})\Big|_{Diag.1-9} = \frac{\alpha\lambda^4}{128 v_{rel}}\frac{T^2}{m_\chi^2}\Bigg[-\frac{4(2m_\chi^2 + (7/9)m_f^2)}{m_\phi^4} + \frac{16m_\chi^2(2m_\chi^2 - (4/3)m_f^2)}{3m_\phi^6} \\
+\frac{64m_\chi^4(2m_\chi^2 - 3m_f^2)}{3m_\phi^8}\Bigg] + O(v^2)\,. \qquad (4.66)
\end{aligned}$$

Note that there are no soft IR divergences (as expected since only thermal photons give rise to such divergences) as well as no collinear divergences from these diagrams.

Chapter 5

Real Photon Thermal Corrections to the Dark Matter Annihilation Cross Section

In order to obtain the complete annihilation cross section for DM to leading order in the QED coupling constant with the model Lagrangian shown in Eq. 1.8, we need to incorporate real photon emission and absorption processes. In fact, Grammer and Yennie technique can be only implemented if one takes thermal corrections due to real photons too. In Chapter 4 we saw that the thermal part of the propagators were used to obtain the finite temperature corrections to the DM annihilation cross section due to virtual photon insertions. But in the case when we take real photon emission and absorption into account, finite temperature correction will arise due to the phase space integrals. This chapter will give the details of the finite temperature corrections due to real photon emission and absorption and is based on our work in Ref. [136]. Now we will discuss the details.

5.1 Real thermal corrections to the cross section at NLO

The thermal contributions to $\chi\chi \to f\overline{f}(\gamma)$ arise from insertions of real photons into the set of LO diagrams shown in Fig. 4.1, which can be both emitted into or absorbed from the heat bath at temperature T. The relevant t-channel diagrams $R1, R2, R3$ are shown in Fig. 5.1 while the corresponding u-channel diagrams $R4, R5, R6$ are obtained by crossing these diagrams.

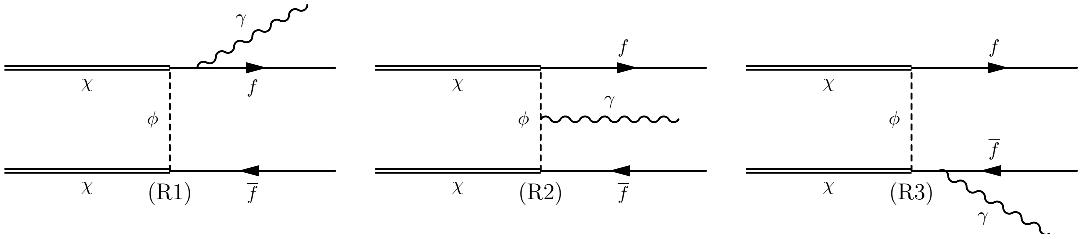

Figure 5.1: *The t-channel real photon emission diagrams contributing to the dark matter annihilation process at next to leading order (NLO). Diagrams are labelled from $R1$–$R3$. Similar terms contribute when the photon is instead absorbed from the heat bath. Analogous contributions from the u-channel diagrams also exist.*

In contrast to the virtual photon case where the thermal $O(\alpha)$ contribution arose from the product of the NLO (virtual) matrix elements of the diagrams in Fig. 4.2 with the LO matrix elements in Fig. 4.1, the $O(\alpha)$ thermal contribution in the real case arises from the *square* of the matrix elements corresponding to the t- and u-channel diagrams.

A quick look at the diagrams in Fig. 5.1 is sufficient to realise that all particles contribute through their type-1 thermal fields at every vertex. As defined in Chapter 2, propagators (for photons, scalars and fermions) are given as the sum of a temperature-independent part and a temperature dependent part, the latter of which is on-shell and weighted by the appropriate (Fermi Dirac or Bose Einstein) distribution function given in Eqs. 2.19, 2.23. It can be seen that neither of the fermion or anti-fermion propagators can contribute through their thermal parts since three particles at a vertex are kinematically forbidden to be all on-shell. Hence, all thermal contributions to the dark matter annihilation process with real photon emission/absorption arise from the corresponding phase space elements; see Eqs. 2.27 and 2.28 for the photon and fermion phase space respectively. The second term in these expressions is the thermal contribution, proportional to $n \equiv n_B\,(n_F)$, the Bose (Fermi) distribution function, for bosons and fermions respectively. In the calculation that follows, only one of the particles (photon, fermion, anti-fermion) at a time is taken to contribute via its thermal part, since the cross section is otherwise suppressed by products of distribution functions.

We therefore have three contributions from each diagram in Fig. 5.1 (and its *u*-channel counterparts): when each of the real photon, fermion, or anti-fermion contributes via the thermal part of its phase space. We shall refer to them as the *real thermal photon*, *real thermal fermion*, and *real thermal anti-fermion* contributions respectively.

We apply the Grammer and Yennie technique [127] as explained in Section 3.2 of Chapter 3. Hence each of the thermal photon contributions can be separated into $\widetilde{K}$ and $\widetilde{G}$ parts by applying the GY technique. However, it turns out that while the GY technique isolates the *soft* IR divergence into the $\widetilde{K}$ (and K) photon contribution, it fails to separate the *collinear* divergence the same way. Hence, in what follows, we shall first demonstrate the cancellation of the soft IR divergences between the $\widetilde{K}$ and K photon contributions, while suppressing the collinear terms, and deal with the collinear divergences separately, in a different section, Section 5.2.4, where we show explicitly that these logarithmic terms cancel between real and virtual contributions. It therefore appears that the use of the GY technique is restricted to those processes where the collinear divergences are independently known to factorise and cancel between virtual and real contributions, order by order in the theory. Even so, there is an advantage in using the GY technique since the divergences cancel at the *integrand* level and simplify the calculation.

5.1.1 Kinematics of $\chi\chi \to f\overline{f}(\gamma)$

We consider the real photon emission/absorption process in the center of momentum frame where the dark matter particles have common energy-momentum $q', q = (H, 0, 0, \pm Q)$. We use the same kinematics as in the virtual case, except for the fact that physical momentum k is gained or lost in the real photon process, so that the fermion (with momentum p') and anti-fermion (with momentum p) no longer have the same energy or momentum (magnitude). The real photon cross section is given by the sum of 21 contributions as follows:

$$\sigma_{NLO}^{Real} = \left[\sum_{i=1}^{6} \sigma_{i,i}^{Real} + (-1)^{S_p} \sum_{i<j}^{6} \sigma_{i,j}^{Real}\right] , \tag{5.1}$$

where the individual terms are defined in terms of the squares of various matrix elements:

$$\begin{aligned}
\sigma_{i,i}^{Real} &= \frac{1}{4\sqrt{s}Q} \int \mathrm{d}P_{p'}\mathrm{d}P_{p}\mathrm{d}P_{k}(2\pi)^4\delta^4(q'+q-p'-p-k)\left|M_{R_i}\right|^2 , \\
\sigma_{i,j}^{Real} &= \frac{1}{4\sqrt{s}Q} \int \mathrm{d}P_{p'}\mathrm{d}P_{p}\mathrm{d}P_{k}(2\pi)^4\delta^4(q'+q-p'-p-k)\left|M_{R_i}M_{R_j}^{\dagger} + h.c.\right|^2 ,
\end{aligned} \tag{5.2}$$

with $-\infty \leq k^0 \leq \infty$, thus allowing for both emission and absorption of the real photon, and

$$\begin{aligned}
S_p &= 0 \; ; \quad i, j \in \{1, 2, 3\} \text{ or } \{4, 5, 6\} , \\
&= 1 \; ; \quad i \in \{1, 2, 3\} \text{ and } j \in \{4, 5, 6\} .
\end{aligned} \tag{5.3}$$

Here the phase space factors dP_i are defined in Eqs. 2.27 and 2.28 for the photon and fermion phase space respectively, and the matrix elements correspond to the three t-channel diagrams $R1, R2, R3$ as seen in Fig. 5.1 and $R4, R5, R6$ are their u-channel counterparts. Therefore $\sigma_{i,j}$, $i, j \in$ 1–3, are from the t-channel diagrams, $\sigma_{i,j}$, $i, j \in$ 4–6, are from the u-channel diagrams, and the remaining from the crossed tu-channel diagrams. In addition, each of these have contributions from three distinct sets of terms: when the photon is thermal, when the fermion is thermal, and when the anti-fermion is thermal. That is, we can write

$$\sigma_{i,j}^{Real} = \sigma_{i,j}^{\gamma,Real} + \sigma_{i,j}^{f,Real} + \sigma_{i,j}^{\bar{f},Real} , \tag{5.4}$$

for all values of (i, j), where the contributions correspond to including the thermal part of the phase space in Eq. 5.2 for the photon, fermion and anti-fermion respectively.

The frame used for the computation is as follows: of the two non-thermal particles, one is integrated out using the energy-momentum conserving delta function shown in Eq. 5.2. The other one is rotated into the z-direction with energy-momentum $(E', 0, 0, P')$, while the thermal particle is arbitrarily aligned in the direction $\hat{n}'(\Omega')$ defined by the angular coordinates (θ', ϕ'). This allows for the simplest kinematics, and yields, for instance, when the *photon is thermal* with momentum $k^\mu = (k^0, K\hat{n}')$, the anti-fermion momentum is integrated out, and the fermion is rotated into the z-axis:

$$\begin{aligned}\sigma_{i,j}^{\gamma,Real} = \frac{1}{32\sqrt{s}Q}\frac{1}{(2\pi)^4}\int_0^{\omega_{max}} \mathrm{d}\omega \int_{E'_{min}}^{E'_{max}} \mathrm{d}E' \int_{-1}^{1} \mathrm{d}\cos\theta \int_0^{2\pi} \mathrm{d}\phi' \\ \times\ n_B(\omega)\left[F_{i,j}^{+}(\omega,\omega,\Omega') + F_{i,j}^{-}(-\omega,\omega,\Omega')\right] ,\end{aligned} \tag{5.5}$$

where $\omega = |k^0|$, the factor $n_B(\omega)$ has been taken out of the integrand to show the dependence on the distribution function, and only the k^μ dependence of the integrand, $F_{i,j}^{\pm}(k^0, K, \Omega')$, has been indicated. Here θ is the angle between the (rotated) z-axis and the dark matter momentum direction; while the thermal photon angle θ' is given by

$$\cos\theta' = \frac{(s - 2\sqrt{s}(E' \pm \omega) \pm 2E'\omega)}{2P'\omega} . \tag{5.6}$$

The ± signs correspond to the case of emission/absorption of the photon. The limits on E' are obtained from constraints on $|\cos\theta'| < 1$ while $\omega_{max} = (s - m_f^2)/(2\sqrt{s})$.

Considering photon to be thermal, for F^+, the limits on E' are given by

$$\begin{aligned}E'^{+}_{min} &= H - \omega + \frac{\mathrm{mf}^2\omega}{4H(H-\omega)} , \\ E'^{+}_{max} &= H - \frac{\mathrm{mf}^2\omega}{4H(H-\omega)} ,\end{aligned} \tag{5.7}$$

whereas for F^-, the limits on E' are

$$\begin{aligned} E'^{-}_{min} &= H + \frac{\mathrm{mf}^2\omega}{4H(H+\omega)} \,, \\ E'^{-}_{max} &= H + \omega - \frac{\mathrm{mf}^2\omega}{4H(H+\omega)} \,, \end{aligned} \tag{5.8}$$

where we have truncated the solution to order $O(m_f^2)$.

When the *thermal fermion* contribution is under consideration, the anti-fermion momentum is integrated out as in the thermal photon case, and the photon is rotated into the z-axis, so that $k^\mu = (E', 0, 0, E')$. In this case, the fermion has momentum $p'^\mu = (p'^0, K_t\hat{n}')$, and we get an expression analogous to Eq. 5.5 for $\sigma^{f,Real}_{i,j}$, while also accounting for the fact that the distribution function $n_B(\omega)$ in Eq. 5.5 is to be replaced by $(-n_F(\omega_t))$ as per the phase space definition in Eq. 2.28; furthermore, the fermion has non-zero mass so that the thermal fermion angle θ' is given by

$$\cos\theta' = \frac{(s - 2\sqrt{s}(E' \pm \omega_t) \pm 2E'\omega_t)}{2E'K_t} \,, \tag{5.9}$$

where the thermal fermion energy and momentum magnitude are represented by $\omega_t = |p'^0|$, and K_t with $\omega_t^2 = K_t^2 + m_f^2$ to distinguish them from the massless photon contribution. The limits on E' are now given by

$$\begin{aligned} E'^{+}_{min} &= \frac{2H(H-\omega_t)(2H-\omega_t-K_t)}{(4H^2-4H\omega_t+m_f^2)} \,; \\ E'^{+}_{max} &= \frac{2H(H-\omega_t)(2H-\omega_t+K_t)}{(4H^2-4H\omega_t+m_f^2)} \,; \\ E'^{-}_{min} &= \frac{2H(H+\omega_t)(2H+\omega_t-K_t)}{(4H^2+4H\omega_t+m_f^2)} \,; \\ E'^{-}_{max} &= \frac{2H(H+\omega_t)(2H+\omega_t+K_t)}{(4H^2+4H\omega_t+m_f^2)} \,. \end{aligned} \tag{5.10}$$

for F^+ and F^- respectively. The case for thermal anti-fermion merely exchanges the fermion and anti-fermion momenta and is straightforward.

In all cases, it can be seen from Eq. 5.5 that high energy contributions are suppressed due to the presence of the appropriate distribution functions, $n_B(\omega)$ and $n_F(\omega_t)$; see Eqs. 2.19 and 2.23. Hence, the upper limit on ω (ω_t) can be taken to be infinity so that these integrals can be analytically performed. The leading thermal contribution of order $O(T^2)$ then arises from the integrals:

$$\begin{aligned} \int_0^\infty \omega\, \mathrm{d}\omega\, n_B(\omega) &= \frac{\pi^2 T^2}{6}\,, \\ \int_0^\infty \omega_t\, \mathrm{d}\omega_t\, n_F(\omega_t) &= \frac{\pi^2 T^2}{12}\,, \end{aligned} \tag{5.11}$$

where we have assumed the massless limit for the thermal fermion integration. (The exact expressions are available as Mathematica notebooks on-line [2].)

5.2 The real photon matrix elements

The relevant matrix elements for the real photon emission/absorption process $\chi\chi \to f\overline{f}(\gamma)$ corresponding to the diagrams $R1$–$R3$ shown in Fig. 5.1 are

$$\begin{aligned} M_{R1} &= \frac{ie|\lambda|^2}{2k\cdot p'\; l_\Phi}\left[\overline{v}(q,m_\chi)P_L\, v(p,m_f)\right]\left[\overline{u}(p',m_f)\gamma_\mu\left(\slashed{k}+\slashed{p}'+m_f\right)P_R\, u(q',m_\chi)\right]\epsilon_k^{*\mu}\,; \\ M_{R2} &= \frac{ie|\lambda|^2}{lk_\Phi\; l_\Phi}\,(2l-k)_\mu\left[\overline{v}(q,m_\chi)P_L v(p,m_f)\right]\left[\overline{u}(p',m_f)P_R\, u(q',m_\chi)\right]\epsilon_k^{*\mu}\,; \\ M_{R3} &= \frac{ie|\lambda|^2}{2k\cdot p\; lk_\Phi}\left[\overline{v}(q,m_\chi)P_L\left(-\slashed{k}-\slashed{p}+m_f\right)\gamma_\mu\, v(p,m_f)\right]\left[\overline{u}(p',m_f)P_R\, u(q',m_\chi)\right]\epsilon_k^{*\mu}\,. \end{aligned} \tag{5.12}$$

Here $P_{R,L} = (1 \pm \gamma_5)/2$, $l_\Phi \equiv (l^2 - m_\phi^2)$ arises from the propagator of the scalar with momentum $l = q - p$. Similarly, $lk_\Phi = (l-k)^2 - m_\phi^2$. The u-channel matrix elements can be obtained by crossing, with momentum $l' = q' - p$ replacing l.

It can be seen from Eq. 5.12 that the squared matrix elements contain products of the photon polarisation tensor, ϵ_k^μ, to which the GY-defined polarisation sum shown in Eq. 3.18

can be applied in order to separate the $\widetilde{K}$ and $\widetilde{G}$ contributions in the thermal photon case. Since there are known to be no IR divergences [126, 130] in the thermal fermion contributions, the standard polarisation sum,

$$\sum_{\text{pol}} \epsilon_k^{\mu *} \, \epsilon_k^{\nu} = -g^{\mu\nu} \, , \tag{5.13}$$

is used in this case.

The angular integrals were performed using FeynCalc 10.0.0 [137, 138] software with Mathematica 13.1 [133]. We will first discuss the soft IR and collinear divergences in the next sections, before we consider the finite contribution. The soft IR divergences arise from the $\widetilde{K}$ photon contributions. Since only thermal photons contribute to these terms, we now consider the case where the thermal part of the photon phase space (see Eq. 2.27 contributes.

5.2.1 The thermal photon contribution and IR divergences

The soft IR divergences are known to cancel between the real and virtual thermal photon contributions. These are contained in the *thermal photon* contributions while the *thermal fermion* contributions are IR finite due to the nature of the Fermi distribution function; see Eq. 2. As shown in Refs. [126, 130], the soft IR divergences can be isolated into the virtual K and real $\widetilde{K}$ photon contributions as defined in Eqs. 3.2, 3.18. The sum of these two contributions is finite (this was first shown to NLO in Ref. [94]); we will explicitly show below the cancellation of the soft IR divergences between these two contributions, and also compute the finite remainder. Details of the NLO virtual thermal correction to $\chi\chi \to f\overline{f}$ are discussed in Chapter 4; for more details, see our earlier work, Ref. [131].

The soft divergence lies in the ω integrals of the *thermal photon* contribution to the real photon cross section which we label $\sigma_{i,j}^{\gamma,Real}$ (see Eq. 5.5); hence we integrate out the angular variables (using Mathematica [133]), leaving only the ω dependence. The $\widetilde{K}$

part of the thermal real photon cross section can be obtained by taking the $\widetilde{K}$ part of the polarisation sum (see Eq. 3.18) in the expressions for $\sigma_{i,j}^{\gamma,Real}$. We have

$$\sigma_{i,j}^{\gamma,Real} = \frac{e^2\pi|\lambda|^4}{32\sqrt{s}Q}\frac{1}{(2\pi)^4}\int \mathrm{d}\omega\, n_B(\omega)\, Int_{i,j}^{\gamma}\,,$$

$$Int_{i,j}^{\gamma} = Int_{i,j}^{\widetilde{K}} + Int_{i,j}^{\widetilde{G}}\,, \tag{5.14}$$

where $Int_{i,j}^{\widetilde{K}}$ is listed for all (i,j) contributions in Table 5.1. Here we have retained only terms up to order $O(\omega, m_f^2)$ since the term linear in ω will give rise to order $O(T^2)$ corrections to the cross section. Hence the terms proportional to $1/\omega$ in Table 5.1 are linearly divergent in the IR. These are expected to cancel against the corresponding contributions from the virtual NLO terms. In order to show this diagram-by-diagram cancellation, we first discuss the virtual–real photon correspondence.

5.2.2 The virtual–real photon correspondence

In order to determine which are the virtual terms corresponding to the real ones, we return to the definition of the real cross section in Eqs. 5.1 and 5.2. The correspondence is as follows. Consider, for example, the $\sigma_{1,1}^{Real}$ term which arises from the square of the diagram $R1$ shown in Fig. 5.1 and can be represented by the cut diagram on the left in Fig. 5.2. The corresponding virtual contribution is then found by shifting the cut on this diagram such that the photon is virtual, as shown on the right side of Fig. 5.2. We label this contribution as $\sigma_{i,j}^{Virtual}$, $(i,j) = (1,1)$, which is given by (see Eq. 4.15)

$$\sigma_{1,1}^{Virtual} \propto \int \left[(\mathcal{M}_{LO}^{t})^{\dagger}\, \mathcal{M}_{NLO}^{6,t} + h.c. \right] . \tag{5.15}$$

This arises from the fermion self-energy term shown as Diagram 6 in Fig. 4.4 multiplied by the conjugate of the the LO t-channel diagram in Fig. 4.1. (The $h.c.$ term is obtained by moving the cut to the left of the self energy insertion.)

(i, j)	**Real** $Int^{\widetilde{K}}_{i,j}$ from $Int^{\gamma}_{i,j}$	**Virtual** $(Int^{K_{div}}_{i,j})'$	$Int^{\widetilde{K}_{fin}}_{i,j} = Int^{\widetilde{K}}_{i,j} + Int^{K_{div}}_{i,j}$
$1, 1$	$-m_\chi^2(\frac{32m_\chi^2-8m_f^2}{\omega m_\phi^4}) - \omega(\frac{32m_\chi^2-8m_f^2}{m_\phi^4})$	$m_\chi^2(\frac{32m_\chi^2-8m_f^2}{\omega m_\phi^4})$	$-\omega(\frac{32m_\chi^2-8m_f^2}{m_\phi^4})$
$2, 2$	$-\omega m_\chi^4(\frac{128m_\chi^2+96m_f^2}{m_\phi^8})$	$-$	$-\omega m_\chi^4(\frac{128m_\chi^2+96m_f^2}{m_\phi^8})$
$3, 3$	$-m_\chi^2(\frac{32m_\chi^2-8m_f^2}{\omega m_\phi^4}) - \omega(\frac{32m_\chi^2-8m_f^2}{m_\phi^4})$	$m_\chi^2(\frac{32m_\chi^2-8m_f^2}{\omega m_\phi^4})$	$-\omega(\frac{32m_\chi^2-8m_f^2}{m_\phi^4})$
$4, 4$	$-m_\chi^2(\frac{32m_\chi^2-8m_f^2}{\omega m_\phi^4}) - \omega(\frac{32m_\chi^2-8m_f^2}{m_\phi^4})$	$m_\chi^2(\frac{32m_\chi^2-8m_f^2}{\omega m_\phi^4})$	$-\omega(\frac{32m_\chi^2-8m_f^2}{m_\phi^4})$
$5, 5$	$-\omega m_\chi^4(\frac{128m_\chi^2+96m_f^2}{m_\phi^8})$	$-$	$-\omega m_\chi^4(\frac{128m_\chi^2+96m_f^2}{m_\phi^8})$
$6, 6$	$-m_\chi^2(\frac{32m_\chi^2-8m_f^2}{\omega m_\phi^4}) - \omega(\frac{32m_\chi^2-8m_f^2}{m_\phi^4})$	$m_\chi^2(\frac{32m_\chi^2-8m_f^2}{\omega m_\phi^4})$	$-\omega(\frac{32m_\chi^2-8m_f^2}{m_\phi^4})$
$1, 2$	0	0	0
$1, 3$	$\omega(\frac{32m_\chi^2-32m_f^2}{m_\phi^4})$	0	$\omega(\frac{32m_\chi^2-32m_f^2}{m_\phi^4})$
$1, 4$	$-m_\chi^2(\frac{64m_\chi^2-48m_f^2}{\omega m_\phi^4}) - \omega(\frac{64m_\chi^2}{m_\phi^4})$	$m_\chi^2(\frac{64m_\chi^2-48m_f^2}{\omega m_\phi^4})$	$-\omega(\frac{64m_\chi^2}{m_\phi^4})$
$1, 5 + 2, 4$	$\omega m_\chi^2(\frac{256m_\chi^2-96m_f^2}{m_\phi^6})$	$-$	$\omega m_\chi^2(\frac{256m_\chi^2-96m_f^2}{m_\phi^6})$
$1, 6 + 3, 4$	0	0	0
$2, 3$	$\omega m_\chi^2(\frac{256m_\chi^2-32m_f^2}{m_\phi^6})$	0	$\omega m_\chi^2(\frac{256m_\chi^2-32m_f^2}{m_\phi^6})$
$2, 5$	$\omega m_\chi^4(\frac{512m_\chi^2-768m_f^2}{m_\phi^8})$	$-$	$\omega m_\chi^4(\frac{512m_\chi^2-768m_f^2}{m_\phi^8})$
$2, 6 + 3, 5$	$\omega m_\chi^2(\frac{256m_\chi^2-96m_f^2}{m_\phi^6})$	0	$\omega m_\chi^2(\frac{256m_\chi^2-96m_f^2}{m_\phi^6})$
$3, 6$	$-m_\chi^2(\frac{64m_\chi^2-48m_f^2}{\omega m_\phi^4}) - \omega(\frac{64m_\chi^2}{m_\phi^4})$	$m_\chi^2(\frac{64m_\chi^2-48m_f^2}{\omega m_\phi^4})$	$-\omega(\frac{64m_\chi^2}{m_\phi^4})$
$4, 5$	$\omega m_\chi^2(\frac{256m_\chi^2-32m_f^2}{m_\phi^6})$	0	$\omega m_\chi^2(\frac{256m_\chi^2-32m_f^2}{m_\phi^6})$
$4, 6$	$\omega(\frac{32m_\chi^2-32m_f^2}{m_\phi^4})$	0	$\omega(\frac{32m_\chi^2-32m_f^2}{m_\phi^4})$
$5, 6$	0	0	0

Table 5.1: *The $\widetilde{K}$ real photon contribution $Int^{\widetilde{K}}_{i,j}$ (see Eq. 5.14) from various diagrams when the* photon is thermal *is listed for all contributions (i, j), along with the* divergent part *of the virtual K photon contribution; the collinear divergences are ignored for now. It can be seen that the IR divergent part of the $\widetilde{K}$ contribution exactly cancels against the divergent part of the corresponding K virtual thermal photon contribution, $(Int^{K_{div}}_{i,j})'$, leaving a finite remainder, which we label as $Int^{\widetilde{K}_{fin}}_{i,j}$. See text for details.*

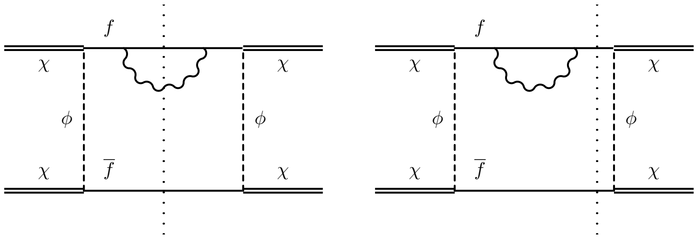

Figure 5.2: *The correspondence between* $\sigma^{Real}_{1,1}$ *(L) and* $\sigma^{Virtual}_{1,1}$ *(R) shown diagrammatically through cut diagrams.*

Similarly, the virtual counterparts of the $(1,2)$ and $(1,3)$ terms arise from the contributions of the NLO diagrams labelled (1) and (2) respectively in Fig. 4.2 multiplied by the conjugate of the LO t-channel diagram in Fig. 4.1, etc. The $(1,2)$ correspondence is shown in Fig. 5.3.

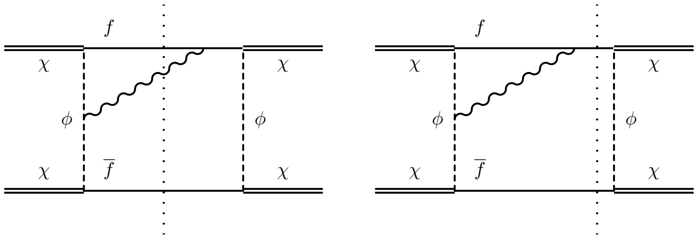

Figure 5.3: *As in Fig.* 5.2 *to demonstrate the* $(1,2)$ *real–virtual correspondence through cut diagrams.*

We use the results from Tables 4.1, 4.4 of the previous chapter to obtain the K photon IR divergent parts of the various virtual thermal photon diagrams. (Note that the Diagrams 4–5 (from photon vertices on the scalar line; see Fig. 4.3) do not have divergent K photon contributions.) These are listed as $(Int^{K_{div}}_{i,j})'$ in the second column of Table 5.1. The change from $Int^{K}_{i,j}$ to $(Int^{K}_{i,j})'$ is now clear: both the virtual and real photon contributions now have the same overall factor removed— see Eq. 5.14—and can be easily compared.

It can be seen from Table 5.1 that the divergent parts of $\widetilde{K}$ and K cancel, leaving behind a finite remainder. Contributions such as from Diagrams $(2,2)$ and $(5,5)$ from the square of matrix elements $R2$ and its u-channel counterpart $R5$ as well as the $(2,5)$ crossed tu-channel contribution must necessarily have no divergent terms as *the virtual counterpart does not exist*. (The same is true for the virtual Diagrams 4–5 in Fig. 4.3 which have no real-photon counterparts.) This is indeed seen to hold.

5.2.3 The collinear divergences

In Table 5.1 we have dropped terms that are collinearly divergent as the fermion mass goes to zero; we will now discuss these terms. For example, it appears from Table 5.1 that there is no soft divergent contribution from the $(1, 3)$ term; however, there is indeed a soft divergent contribution which is also collinear divergent. *All* soft IR divergent terms are correctly factored into the $\widetilde{K}$ contributions for the real terms, so that the $\widetilde{G}$ contributions are IR finite. However, some of the *soft IR finite terms* which are collinear divergent are seen to be partially contained in the $\widetilde{K}$ and partially in the $\widetilde{G}$ contributions so that the GY separation for collinear divergences is imperfect. The collinear divergences from real thermal photon insertions (sum of $\widetilde{G} + \widetilde{K}$ contributions) is shown in Table 5.2.

In the case of *thermal photons*, the structure of the logarithms that contribute in the real case is given by

$$\begin{aligned}
L_R &= \frac{1}{2}\left(\log\left[\frac{m_f^2}{4H^2 - 4H\omega - m_f^2}\right] + \log\left[\frac{m_f^2}{4H^2 + 4H\omega - m_f^2}\right]\right) , \\
L_R' &= \frac{1}{2}\left(\log\left[\frac{m_f^2}{4H^2 - 4H\omega - m_f^2}\right] - \log\left[\frac{m_f^2}{4H^2 + 4H\omega - m_f^2}\right]\right) .
\end{aligned} \tag{5.16}$$

Since ω is strictly less than $(s - m_f^2)/(2\sqrt{s}) = H - m_f^2/(4H)$, we can expand L_R and L_R' as

$$\begin{aligned}
L_R &= \frac{1}{2}\left(\log\left[\frac{m_f^2}{4H^2 - m_f^2}\left(1 + \frac{4H\omega}{4H^2 - m_f^2}\right)\right] + \log\left[\frac{m_f^2}{4H^2 - m_f^2}\left(1 - \frac{4H\omega}{4H^2 - m_f^2}\right)\right]\right), \\
&\approx \log\left[\frac{m_f^2}{4H^2 - m_f^2}\right] - \frac{(4H\omega)^2}{2(4H^2 - m_f^2)^2} \equiv L_\gamma + \mathcal{O}(\omega)^2 , \\
L_R' &= \frac{1}{2}\left(\log\left[\frac{m_f^2}{4H^2 - m_f^2}\left(1 + \frac{4H\omega}{4H^2 - m_f^2}\right)\right] - \log\left[\frac{m_f^2}{4H^2 - m_f^2}\left(1 - \frac{4H\omega}{4H^2 - m_f^2}\right)\right]\right), \\
&\approx \left[\frac{4H\omega}{4H^2 - m_f^2}\right] + \mathcal{O}(\omega)^3 ,
\end{aligned} \tag{5.17}$$

where we have expanded the log terms appropriately, and used the definition of L_γ in Eq. 4.60. We have retained terms only till order $\mathcal{O}(\omega)$ since higher order terms contribute

Real Thermal Photon Collinear Contributions	
(i, j)	$Int_{i,j}^{Coll\gamma}$
$1, 1$	$-\omega\frac{48m_\chi^2}{3m_\phi^4}L_R$
$2, 2$	0
$3, 3(= 1, 1)$	$-\omega\frac{48m_\chi^2}{3m_\phi^4}L_R$
$4, 4(= 1, 1)$	$-\omega\frac{48m_\chi^2}{3m_\phi^4}L_R$
$5, 5$	0
$6, 6(= 1, 1)$	$-\omega\frac{48m_\chi^2}{3m_\phi^4}L_R$
$1, 2$	$-\omega\frac{32m_\chi^2}{m_\phi^6}(2m_\chi^2 - m_f^2)L_R + \frac{64m_\chi^3}{m_\phi^6}(m_\chi^2 - m_f^2)L'_R$
$1, 3$	$-\frac{16m_\chi^2}{\omega m_\phi^4}(4m_\chi^2 - 2m_f^2)L_R - \omega\frac{16m_f^2}{m_\phi^4}L_R + \frac{64m_\chi^3}{m_\phi^4}L'_R$
$1, 4$	$-\omega\frac{32m_\chi^2}{m_\phi^4}L_R - \frac{16}{m_\phi^4}(m_\chi m_f^2)L'_R$
$1, 5 + 2, 4$	$-\omega\frac{32m_\chi^2}{m_\phi^6}(4m_\chi^2 - 3m_f^2)L_R + \frac{32m_\chi^3}{m_\phi^6}(4m_\chi^2 - 6m_f^2)L'_R$
$1, 6 + 3, 4$	$-\frac{32(2m_\chi^2-m_f^2)^2}{\omega m_\phi^4}L_R + \frac{32m_\chi}{m_\phi^4}(4m_\chi^2 - m_f^2)L'_R$
$2, 3(= 1, 2)$	$-\omega\frac{32m_\chi^2}{m_\phi^6}(2m_\chi^2 - m_f^2)L_R + \frac{64m_\chi^3}{m_\phi^6}(m_\chi^2 - m_f^2)L'_R$
$2, 5$	0
$2, 6 + 3, 5$	$-\omega\frac{32m_\chi^2}{m_\phi^6}(4m_\chi^2 - 3m_\chi^2)L_R + \frac{32m_\chi^3}{m_\phi^6}(4m_\chi^2 - 6m_f^2)L'_R$
$3, 6$	$-\omega\frac{32m_\chi^2}{m_\phi^4}L_R - \frac{16m_\chi}{m_\phi^4}(m_f^2)L'_R$
$4, 5(= 1, 2)$	$-\omega\frac{32m_\chi^2}{m_\phi^6}(2m_\chi^2 - m_f^2)L_R + \frac{64m_\chi^3}{m_\phi^6}(m_\chi^2 - m_f^2)L'_R$
$4, 6(= 1, 3)$	$-\frac{16m_\chi^2}{\omega m_\phi^4}(4m_\chi^2 - 2m_f^2)L_R - \omega\frac{16m_f^2}{m_\phi^4}L_R + \frac{64m_\chi^3}{m_\phi^4}L'_R$
$5, 6(= 1, 2)$	$-\omega\frac{32m_\chi^2}{m_\phi^6}(2m_\chi^2 - m_f^2)L_R + \frac{64m_\chi^3}{m_\phi^6}(m_\chi^2 - m_f^2)L'_R$

Table 5.2: *Collinear divergences in various terms of the real* thermal photon *contributions. Overall factors as in Eq. 5.14 have been removed from the terms listed here. See text for the definition of log terms L_R and L'_R.*

at order $\mathcal{O}((T/m_\chi)^4)$ or higher, and are hence small. Note that terms such as the $(1,3)$ contribution in Table 5.2 contain $(1/\omega)$ soft IR terms, so that these terms will contribute at order $\mathcal{O}(T^2)$ (via $\mathcal{O}(\omega)$ terms) when combined with $\mathcal{O}(\omega)^2$ terms in L_R. Similarly, the L'_R terms will also contribute at order $\mathcal{O}(T^2)$. It can be seen from Table 5.2 that the coefficient of L'_R contains terms that are proportional to, and independent of m_f^2. The coefficient of L'_R, when summed over all (i,j) as shown in Eqs. 5.1, 5.2, equals $(0 \times m_\chi^2 + \mathcal{O}(m_f^2))$ and hence this contribution vanishes in the collinear limit as $m_f \to 0$.

In fact, collinear divergent terms arise in all contributions: the *thermal photon*, *thermal fermion* and the *thermal anti-fermion* terms. Their contribution for thermal fermions and anti-fermions is given in Tables 5.3 and 5.4, in terms of different logarithmic terms, L_R and L'_R, defined below.

In the case of real photons, we have the factor $n_B(\omega)$ in the phase space for thermal photons, while we have $(-n_F(\omega_t))$ for thermal fermions (anti-fermions); see Eqs. 2.27 and 2.28 respectively. Hence we compute the collinear contributions in $\sigma_{i,j}^{\gamma,Real}$, from the *thermal photon* contribution to the cross section, as given in Eq. 5.14, as well as from the *thermal fermion* contributions, given by

$$\sigma_{i,j}^{f,Real} = \frac{e^2\pi|\lambda|^4}{32\sqrt{s}Q}\frac{1}{(2\pi)^4}\int \mathrm{d}\omega_t \; [-n_F(\omega_t)] \; \left[-Int_{i,j}^f\right] , \tag{5.18}$$

(that is, the negative sign has been included in the values of $Int_{i,j}^f$ in the tables) with an analogous definition for the *thermal anti-fermion* contribution, $\sigma_{i,j}^{\bar{f},Real}$. We have the log terms L_{R_f} and L'_{R_f} for the real *thermal fermion and anti-fermion* contributions in Tables 5.3 and 5.4:

$$\begin{aligned}
L_{R_f} &= \frac{1}{2}\left(\log\left[\frac{2H(\omega_t - K_t) - m_f^2}{2H(\omega_t + K_t) - m_f^2}\right] + \log\left[\frac{2H(\omega_t - K_t) + m_f^2}{2H(\omega_t + K_t) + m_f^2}\right]\right) , \\
L'_{R_f} &= \frac{1}{2}\left(\log\left[\frac{2H(\omega_t - K_t) - m_f^2}{2H(\omega_t + K_t) - m_f^2}\right] - \log\left[\frac{2H(\omega_t - K_t) + m_f^2}{2H(\omega_t + K_t) + m_f^2}\right]\right) .
\end{aligned} \tag{5.19}$$

Real Thermal Fermion Collinear Contribution	
(i, j)	$Int_{i,j}^{Collf}$
$1, 1$	$-\omega_t \frac{16m_\chi^2}{m_\phi^4} L_{R_f} + \frac{16m_\chi^3}{m_\phi^4} L'_{R_f}$
$2, 2$	0
$3, 3$	0
$4, 4(= 1, 1)$	$-\omega_t \frac{16m_\chi^2}{m_\phi^4} L_{R_f} + \frac{16m_\chi^3}{m_\phi^4} L'_{R_f}$
$5, 5$	0
$6, 6$	0
$1, 2$	$-\omega_t \frac{32m_\chi^2}{m_\phi^6} (2m_\chi^2 - m_f^2) L_{R_f} + \frac{32m_\chi^2}{m_\phi^6} (m_\chi m_f^2) L'_{R_f}$
$1, 3$	$\omega_t \frac{8}{m_\phi^4} (4m_\chi^2 - 3m_f^2) L_{R_f} - \frac{8}{m_\phi^4} (m_\chi m_f^2) L'_{R_f}$
$1, 4$	$-\omega_t \frac{32m_\chi^2}{m_\phi^4} L_{R_f} + \frac{16m_\chi}{m_\phi^4} (2m_\chi^2 + m_f^2) L'_{R_f}$
$1, 5 + 2, 4$	$-\omega_t \frac{32m_\chi^2}{m_\phi^6} (4m_\chi^2 - 3m_f^2) L_{R_f} + \frac{32m_\chi^3}{m_\phi^6} (3m_f^2) L'_{R_f}$
$1, 6 + 3, 4$	$\omega_t \frac{16(2m_\chi^2 - m_f^2)^2}{m_\chi^2 m_\phi^4} L_{R_f} - \frac{16m_\chi}{m_\phi^4} (3m_f^2) L'_{R_f}$
$2, 3$	0
$2, 5$	0
$2, 6 + 3, 5$	0
$3, 6$	0
$4, 5(= 1, 2)$	$-\omega_t \frac{32m_\chi^2}{m_\phi^6} (2m_\chi^2 - m_f^2) L_{R_f} + \frac{32m_\chi^2}{m_\phi^6} (m_\chi m_f^2) L'_{R_f}$
$4, 6(= 1, 3)$	$\omega_t \frac{8}{m_\phi^4} (4m_\chi^2 - 3m_f^2) L_{R_f} - \frac{8}{m_\phi^4} (m_\chi m_f^2) L'_{R_f}$
$5, 6$	0

Table 5.3: *As in Table 5.2 for collinear divergences from* thermal fermions. *See text for a definition of the log terms L_{R_f} and L'_{R_f}.*

Real Thermal Anti-Fermion Collinear Contribution	
(i,j)	$Int_{i,j}^{Coll\overline{f}}$
$1,1$	0
$2,2$	0
$3,3$	$-\omega_t \frac{16m_\chi^2}{m_\phi^4} L_{R_f} + \frac{16m_\chi^3}{m_\phi^4} L'_{R_f}$
$4,4$	0
$5,5$	0
$6,6(=3,3)$	$-\omega_t \frac{16m_\chi^2}{m_\phi^4} L_{R_f} + \frac{16m_\chi^3}{m_\phi^4} L'_{R_f}$
$1,2$	0
$1,3$	$\omega_t \frac{8}{m_\phi^4}(4m_\chi^2 - 3m_f^2) L_{R_f} - \frac{8m_\chi}{m_\phi^4}(m_f^2) L'_{R_f}$
$1,4$	0
$1,5+2,4$	0
$1,6+3,4$	$\omega_t \frac{16(2m_\chi^2 - m_f^2)^2}{m_\chi^2 m_\phi^4} L_{R_f} - \frac{16m_f^2}{m_\phi^4}(3m_\chi^2 - m_f^2) L'_{R_f}$
$2,3$	$-\omega_t \frac{32}{m_\phi^6}(2m_\chi^2 - m_f^2) L_{R_f} + \frac{32m_\chi^3}{m_\phi^6}(m_f^2) L'_{R_f}$
$2,5$	0
$2,6+3,5$	$-\omega_t \frac{32m_\chi^2(4m_\chi^2 - 3m_f^2)}{m_\phi^6} L_{R_f}$
$3,6$	$-\omega_t \frac{32m_\chi^2}{m_\phi^4} L_{R_f} + \frac{16m_\chi}{m_\phi^6}(2m_\chi^2 + m_f^2) L'_{R_f}$
$4,5$	0
$4,6(=1,3)$	$\omega_t \frac{8}{m_\phi^4}(4m_\chi^2 - 3m_f^2) L_{R_f} - \frac{8m_\chi}{m_\phi^4}(m_f^2) L'_{R_f}$
$5,6(=2,3)$	$-\omega_t \frac{32}{m_\phi^6}(2m_\chi^2 - m_f^2) L_{R_f} + \frac{32m_\chi^3}{m_\phi^6}(m_f^2) L'_{R_f}$

Table 5.4: *As in Table 5.3 for collinear divergences from* thermal anti-fermions.

As in the case of the real photon thermal photon calculation, see Eq. 5.17, we can expand these logarithms:

$$
\begin{aligned}
\log\left[\frac{2H(\omega_t - K_t) - m_f^2}{2H(\omega_t + K_t) - m_f^2}\right] &= \log\left[\frac{\omega_t - K_t}{\omega_t + K_t}\right] + \log\left[1 - \epsilon_{f-}\right] - \log\left[1 - \epsilon_{f+}\right] \,, \\
&\equiv L_f + \log\left[1 - \epsilon_{f-}\right] - \log\left[1 - \epsilon_{f+}\right] \,, \\
\log\left[\frac{2H(\omega_t - K_t) - m_f^2}{2H(\omega_t + K_t) + m_f^2}\right] &= \log\left[\frac{\omega_t - K_t}{\omega_t + K_t}\right] + \log\left[1 + \epsilon_{f-}\right] - \log\left[1 + \epsilon_{f+}\right] \,, \\
&\equiv L_f + \log\left[1 + \epsilon_{f-}\right] - \log\left[1 + \epsilon_{f+}\right] \,, \qquad (5.20)
\end{aligned}
$$

where L_f, defined in Eq. 4.64, is the logarithmic term from thermal fermions. Here the ϵ_f's are the small terms

$$
\epsilon_{f-} = \frac{\omega_t + K_t}{2H} \,, \qquad \epsilon_{f+} = \frac{\omega_t - K_t}{2H} \,. \qquad (5.21)
$$

Hence, the various log terms are given by

$$
\begin{aligned}
L_{R_f} &= L_f - \frac{4H^2 - m_f^2}{8H^2}\omega_t K_t = L_f + O(\omega_t)^2 \,, \\
L'_{R_f} &= -\frac{12H^2 - m_f^2}{12H^3}\omega_t + O(\omega_t)^3 \,, \qquad (5.22)
\end{aligned}
$$

similar to the case with virtual thermal fermions, and L_f defined in Eq. 4.64. Again, we find (both for the thermal fermion and thermal anti-fermion contributions) that when summing over all L'_{R_f} terms the coefficient of the m_χ^2 term vanishes[1], leaving terms whose coefficient is proportional to m_f^2, which vanish in the collinear limit. Hence, in the collinear thermal photon and thermal fermion contributions, only terms containing L_R and L_{R_f} survive for the real photon case.

---

[1] Note that the contribution of the tu-cross terms, viz., $(1,4), (1,5+2,4), (1,6+3,4), (2,5), (2,6+3,5)$ and $(3,6)$ comes with a negative sign.

5.2.4 Cancellation of collinear divergences

We have now computed the collinearly divergent terms from all Diagrams (i, j) from both virtual and real photon insertions. These arise from the *thermal phase space* for photons, fermions, and anti-fermions in the case of real photon annihilation cross sections. In the case of virtual contributions, the *thermal photon*, *thermal fermion* and *thermal anti-fermion* contributions come from the corresponding thermal parts of their propagators in Diagrams 1–7 in Figs. 4.2, 4.3 and 4.4. The relevant real and virtual collinear contributions are listed in Tables 5.5, 5.6 and 5.7. Here only the leading s-wave results with $v \to 0$ are shown; the exact expressions are available on-line as a Mathematica notebook [2]. We have dropped the terms L'_{V_f}, L'_R and L'_{R_f} which vanish in the collinear limit; we will deal with them later.

It may be noted that the logarithms are not precisely the same in the real and virtual case; they merely match in the collinear (massless) limit. In the case of *thermal photons*, it can be seen from Table 5.5 that, upon using the definitions of L_R in Eq. 5.16 and its expansion in 5.17, we find that, apart from finite contributions, $L_R = L_V \equiv L_\gamma$ (see Eqs. 4.60, 5.17), so that the collinear divergences (containing both soft IR divergent and IR finite terms) cancel between the real and virtual photon contributions when the photon is thermal. Note that terms proportional to m_f^2 in the coefficient of the log terms vanish in the collinear limit and hence are not collinear divergent.

A similar analysis can be done when the fermion (anti-fermion) is thermal. The results are tabulated in Tables 5.6 (5.7). Here we have the log terms L_{R_f} and L'_{R_f} for the real *thermal fermion* contribution as defined in Eq. 5.22 and the corresponding virtual contributions in Eq. 4.64.

We find that the coefficient of every contribution to L'_{V_f} is proportional to m_f^2 and hence this contribution vanishes in the collinear limit.

As with L'_V, the sum over all (i, j) of L'_{R_f} yields a coefficient which has the form $(0 \times$

Real and Virtual Thermal Photon Collinear Contributions		
i, j	Real	Virtual
$1, 1$	$-\omega\frac{48m_\chi^2}{3m_\phi^4}L_R$	$\omega\frac{48m_\chi^2}{3m_\phi^4}L_V$
$2, 2$	0	–
$3, 3$	$-\omega\frac{48m_\chi^2}{3m_\phi^4}L_R$	$\omega\frac{48m_\chi^2}{3m_\phi^4}L_V$
$4, 4$	$-\omega\frac{16m_\chi^2}{m_\phi^4}L_R$	$\omega\frac{16m_\chi^2}{m_\phi^4}L_V$
$5, 5$	0	–
$6, 6$	$-\omega\frac{48m_\chi^2}{3m_\phi^4}L_R$	$\omega\frac{48m_\chi^2}{3m_\phi^4}L_V$
$1, 2$	$-\omega\frac{32}{3m_\phi^6}(6m_\chi^4 - 3m_\chi^2 m_f^2)L_R$	$\omega\frac{32}{3m_\phi^6}(6m_\chi^4 - 3m_\chi^2 m_f^2)L_V$
$1, 3$	$-\frac{16(4m_\chi^4 - 2m_\chi^2 m_f^2)}{\omega m_\phi^4}L_R - \omega\frac{16m_f^2}{m_\phi^4}L_R$	$\frac{16(4m_\chi^4 - 2m_\chi^2 m_f^2)}{\omega m_\phi^4}L_V + \omega\frac{16m_f^2}{m_\phi^4}L_V$
$1, 4$	$-\omega\frac{32m_\chi^2}{m_\phi^4}L_R$	$\omega\frac{32m_\chi^2}{m_\phi^4}L_V$
$1, 5 + 2, 4$	$-\omega\frac{32m_\chi^2(4m_\chi^2 - 3m_f^2)}{m_\phi^6}L_R$	$\omega\frac{32m_\chi^2(4m_\chi^2 - 3m_f^2)}{m_\phi^6}L_V$
$1, 6 + 3, 4$	$-\frac{32(-2m_\chi^2 + m_f^2)^2}{\omega m_\phi^4}L_R$	$\frac{32(-2m_\chi^2 + m_f^2)^2}{\omega m_\phi^4}L_V$
$2, 3$	$-\omega\frac{32m_\chi^2(2m_\chi^2 - m_f^2)}{m_\phi^6}L_R$	$\omega\frac{32m_\chi^2(2m_\chi^2 - m_f^2)}{m_\phi^6}L_V$
$2, 5$	0	–
$2, 6 + 3, 5$	$-\omega\frac{32m_\chi^2(4m_\chi^2 - 3m_\chi^2)}{m_\phi^6}L_R$	$\omega\frac{32m_\chi^2(4m_\chi^2 - 3m_\chi^2)}{m_\phi^6}L_V$
$3, 6$	$-\omega\frac{32m_\chi^2}{m_\phi^4}L_R$	$\omega\frac{32m_\chi^2}{m_\phi^4}L_V$
$4, 5$	$-32\omega m_\chi^2\frac{2m_\chi^2 - m_f^2)}{m_\phi^6}L_R$	$32\omega m_\chi^2\frac{2m_\chi^2 - m_f^2)}{m_\phi^6}L_V$
$4, 6$	$-\frac{16(4m_\chi^4 - 2m_\chi^2 m_f^2)}{\omega m_\phi^4}L_R - \omega\frac{16m_f^2}{m_\phi^4}L_R$	$\frac{16(4m_\chi^4 - 2m_\chi^2 m_f^2)}{\omega m_\phi^4}L_V + \omega\frac{16m_f^2}{m_\phi^4}L_V$
$5, 6$	$-32\omega m_\chi^2\frac{2m_\chi^2 - m_f^2)}{m_\phi^6}L_R$	$32\omega m_\chi^2\frac{2m_\chi^2 - m_f^2)}{m_\phi^6}L_V$

Table 5.5: *Collinear divergences from Diagram sets* (i, j) *from real and virtual* thermal photon *contributions. Divergent terms from real and virtual contributions cancel. See text for the definition of log terms* L_R *and* L_V*.*

Real and Virtual Thermal Fermion Collinear Contributions		
i, j	Real	Virtual
$1,1$	$-\omega_t \frac{16m_\chi^2}{m_\phi^4} L_{R_f}$	$\omega_t \frac{16m_\chi^2}{m_\phi^4} L_{V_f}$
$2,2$	0	–
$3,3$	0	0
$4,4$	$-\omega_t \frac{16m_\chi^2}{m_\phi^4} L_{R_f}$	$\omega_t \frac{16m_\chi^2}{m_\phi^4} L_{V_f}$
$5,5$	0	–
$6,6$	0	0
$1,2$	$-\omega_t \frac{32m_\chi^2(2m_\chi^2-m_f^2)}{m_\phi^6} L_{R_f}$	$\omega_t \frac{32m_\chi^2(2m_\chi^2-m_f^2)}{m_\phi^6} L_{V_f}$
$1,3$	$\omega_t \frac{8(4m_\chi^2-3m_f^2)}{m_\phi^4} L_{R_f}$	$-\omega_t \frac{8(4m_\chi^2-3m_f^2)}{m_\phi^4} L_{V_f}$
$1,4$	$-\omega_t \frac{32m_\chi^2}{m_\phi^4} L_{R_f}$	$\omega_t \frac{32m_\chi^2}{m_\phi^4} L_{V_f}$
$1,5+2,4$	$-\omega_t \frac{32m_\chi^2(4m_\chi^2-3m_f^2)}{m_\phi^6} L_{R_f}$	$\omega_t \frac{32m_\chi^2(4m_\chi^2-3m_f^2)}{m_\phi^6} L_{V_f}$
$1,6+3,4$	$\omega_t \frac{16(2m_\chi^2-m_f^2)^2}{m_\chi^2 m_\phi^4} L_{R_f}$	$-\omega_t \frac{16(2m_\chi^2-m_f^2)^2}{m_\chi^2 m_\phi^4} L_{V_f}$
$2,3$	0	0
$2,5$	0	–
$2,6+3,5$	0	0
$3,6$	0	0
$4,5$	$-\omega_t \frac{32m_\chi^2(2m_\chi^2-m_f^2)}{m_\phi^6} L_{R_f}$	$\omega_t \frac{32m_\chi^2(2m_\chi^2-m_f^2)}{m_\phi^6} L_{V_f}$
$4,6$	$\omega_t \frac{8m_\chi^2(4m_\chi^2-3m_f^2)}{m_\phi^4} L_{R_f}$	$-\omega_t \frac{8m_\chi^2(4m_\chi^2-3m_f^2)}{m_\phi^4} L_{V_f}$
$5,6$	0	0

Table 5.6: *As in Table 5.5 for collinear divergences in various terms of real and virtual contributions from* thermal fermions. *See text for a definition of the log terms* L_{R_f} *and* L_{V_f}.

Real and Virtual Thermal Anti-Fermion Collinear Contributions		
i, j	Real	Virtual
$1, 1$	0	0
$2, 2$	0	–
$3, 3$	$-\omega_t \frac{16m_\chi^2}{m_\phi^4} L_{R_f}$	$\omega_t \frac{16m_\chi^2}{m_\phi^4} L_{V_f}$
$4, 4$	0	0
$5, 5$	0	–
$6, 6$	$-\omega_t \frac{16m_\chi^2}{m_\phi^4} L_{R_f}$	$\omega_t \frac{16m_\chi^2}{m_\phi^4} L_{V_f}$
$1, 2$	0	0
$1, 3$	$\omega_t \frac{8(4m_\chi^2-3m_f^2)}{m_\phi^4} L_{R_f}$	$-\omega_t \frac{8(4m_\chi^2-3m_f^2)}{m_\phi^4} L_{V_f}$
$1, 4$	0	0
$1, 5 + 2, 4$	0	0
$1, 6 + 3, 4$	$\omega_t \frac{16(2m_\chi^2-m_f^2)^2}{m_\chi^2 m_\phi^4} L_{R_f}$	$-\omega_t \frac{16(2m_\chi^2-m_f^2)^2}{m_\chi^2 m_\phi^4} L_{V_f}$
$2, 3$	$-\omega_t \frac{32(2m_\chi^2-m_f^2)}{m_\phi^6} L_{R_f}$	$\omega_t \frac{32(2m_\chi^2-m_f^2)}{m_\phi^6} L_{V_f}$
$2, 5$	0	–
$2, 6 + 3, 5$	$-\omega_t \frac{32m_\chi^2(4m_\chi^2-3m_f^2)}{m_\phi^6} L_{R_f}$	$\omega_t \frac{32m_\chi^2(4m_\chi^2-3m_f^2)}{m_\phi^6} L_{V_f}$
$3, 6$	$-\omega_t \frac{32m_\chi^2}{m_\phi^4} L_{R_f}$	$\omega_t \frac{32m_\chi^2}{m_\phi^4} L_{V_f}$
$4, 5$	0	0
$4, 6$	$\omega_t \frac{8(4m_\chi^2-3m_f^2)}{m_\phi^4} L_{R_f}$	$-\omega_t \frac{8(4m_\chi^2-3m_f^2)}{m_\phi^4} L_{V_f}$
$5, 6$	$-\omega_t \frac{32m_\chi^2(2m_\chi^2-m_f^2)}{m_\phi^6} L_{R_f}$	$\omega_t \frac{32m_\chi^2(2m_\chi^2-m_f^2)}{m_\phi^6} L_{V_f}$

Table 5.7: *As in Table 5.5 for collinear divergences in various terms of real and virtual contributions from* thermal anti-fermions. *See text for a definition of the log terms L_{R_f} and L_{V_f}.*

$m_\chi^2 + O(m_f^2)$), so that these contributions also vanish in the collinear limit. We are left with terms proportional to L_{V_f} and L_{R_f}, as listed in Tables 5.6 and 5.7. Dropping the finite contributions for now, the collinear contributions from both are given by $L'_{R_f} = L'_{V_f} \equiv L_f$ as defined in Eqs. 5.22 and 4.64.

Notice the unusual structure of L_f, *independent* of the external energy H (except indirectly through the limits on ω_t). To our knowledge, such a dependence has been observed for the first time. With the identification of $L_{V_f} = L_{R_f} \equiv L_f$, again, we see from Tables 5.6, 5.7 that the collinear divergent terms arising from thermal fermion and thermal anti-fermion pieces also cancel between the real and virtual terms. Hence the entire cross section is both soft IR finite and free of collinear divergences to $O(\alpha T^2)$.

It may be useful to point out that the structure of the log terms L_R, L_{V_f} and L_{R_f} is non-trivial and furthermore, ω (or ω_t) dependent and hence can only be exactly numerically computed. Our approximations in Eqs. 4.60, 5.17, and Eqs. 4.64, 5.22, allow for the cancellations to be demonstrated at the level of the integrands themselves, without having to perform the ω (ω_t) integrations. While it is satisfying to see the cancellation of these collinear divergences, it must be kept in mind that heavy fermions such as τ leptons can significantly contribute through these logs, which may substantially alter our results shown in the next section for the nearly massless case. Again, the exact expressions are available on-line [2] for use in numerical computations.

5.2.5 Finite remainder and the real thermal photon cross section

The total *thermal photon* contribution to the real photon dark matter annihilation process arises from the sum of the finite $\widetilde{G}$ and the finite $Int_{i,j}^{\widetilde{K}_{fin}} = (\widetilde{K} + K_{div})$; we have already discussed the latter in the previous section and the corresponding results are listed in Table 5.1. The contribution $Int_{i,j}^{\widetilde{G}}$ from the *thermal photon* $\widetilde{G}$ part from various (i, j) terms (see Eq. 5.14) is shown in Table 5.8, modulo the collinear divergences, which have been separately discussed in Section 5.2.4.

The thermal fermion (and anti-fermion) contributions $Int^{f}_{i,j}$ and $Int^{\overline{f}}_{i,j}$ (see Eq. 5.18) are IR finite and can be simply added to the thermal photon contribution. These are also listed (again, modulo the collinear divergent terms which were discussed in Section 5.2.4) in Table 5.8. The total NLO thermal cross section is thus given by the sum of all these terms. The detailed results are again listed online [2]. Here we present only the s-wave results in the limit that the dark matter momentum Q is small. We present the results separately for the so-called "virtual", "real" and "collinear" parts and then sum them to obtain the total NLO thermal cross section. The "virtual" contributions have already been computed in the previous Chapter. The "real" part arises from the total NLO thermal cross section defined in Eq. 5.4 for the process $\chi\chi \to f\overline{f}(\gamma)$ which is given by

$$\sigma^{Real}_{NLO} = \frac{\alpha|\lambda|^4}{128 v_{rel}} \frac{T^2}{m_\chi^2} m_f^2 \left[\frac{16}{3m_\phi^4} + \frac{160 m_\chi^4}{9 m_\phi^8} \right] , \tag{5.23}$$

where again we have retained terms to order $O(T^2, m_f^2)$. It can be seen that the total real photon thermal cross section is again proportional to the fermion mass squared, and hence is helicity suppressed, as for the thermal virtual cross section in Eq. 4.58, although the individual terms in Tables 5.1, 5.8 are all not so.

The finite "collinear" contribution arises from the finite (independent of L_γ and L_f) contributions of the logarithmic terms, L_V, L'_V and L_{V_f}, L'_{V_f} from the virtual thermal photon and thermal fermion contributions shown in Eqs. 4.60, 4.64, and from the finite terms in L_R, L'_R and L_{R_f}, L'_{R_f} in Eqs. 5.17, 5.22 for the real thermal photon and fermions contributions respectively. The thermal photon and thermal fermion finite "collinear" contributions are given by

$$\begin{aligned} \sigma^{coll,\gamma}_{NLO} &= \frac{\alpha|\lambda|^4}{128 v_{rel}} \frac{T^2}{m_\chi^2} m_f^2 \left[\frac{16}{3m_\phi^4} + \frac{64 m_\chi^4}{3 m_\phi^8} \right] , \\ \sigma^{coll,f+\overline{f}}_{NLO} &= \frac{\alpha|\lambda|^4}{128 v_{rel}} \frac{T^2}{m_\chi^2} m_f^2 \left[\frac{24}{3m_\phi^4} - \frac{16 m_\chi^2}{3 m_\phi^6} \right] , \end{aligned} \tag{5.24}$$

i, j	**Real** $Int^{\widetilde{G}}_{i,j}$ **from** $Int^{\gamma}_{i,j}$	**Real** $Int^{f}_{i,j}$	**Real** $Int^{\overline{f}}_{i,j}$
$1, 1$	$\omega(\frac{32m_\chi^2}{m_\phi^4})$	$-K_t(\frac{32m_\chi^2-12m_f^2}{m_\phi^4})$	0
$2, 2$	$\omega m_\chi^4(\frac{256m_\chi^2-96m_f^2}{m_\phi^8})$	0	0
$3, 3$	$\omega(\frac{32m_\chi^2}{m_\phi^4})$	0	$-K_t(\frac{32m_\chi^2-12m_f^2}{m_\phi^4})$
$4, 4$	$\omega(\frac{32m_\chi^2}{m_\phi^4})$	$-K_t(\frac{32m_\chi^2-12m_f^2}{m_\phi^4})$	0
$5, 5$	$\omega m_\chi^4(\frac{256m_\chi^2-96m_f^2}{m_\phi^8})$	0	0
$6, 6$	$\omega(\frac{32m_\chi^2}{m_\phi^4})$	0	$-K_t(\frac{32m_\chi^2-12m_f^2}{m_\phi^4})$
$1, 2$	$\omega m_\chi^2(\frac{64m_\chi^2-32m_f^2}{m_\phi^6})$	$K_t m_\chi^2(\frac{64m_\chi^2}{m_\phi^6})$	0
$1, 3$	$-\omega(\frac{64m_\chi^2-32m_f^2}{m_\phi^4})$	$-K_t(\frac{32m_\chi^2}{m_\phi^4})$	$-K_t(\frac{32m_\chi^2}{m_\phi^4})$
$1, 4$	$\omega(\frac{32m_\chi^2+16m_f^2}{m_\phi^4})$	$-K_t(\frac{64m_\chi^2-32m_f^2}{m_\phi^4})$	$-K_t(\frac{8m_f^2}{m_\phi^4})$
$1, 5 + 2, 4$	$-\omega m_\chi^2(\frac{128m_\chi^2+32m_f^2}{m_\phi^6})$	$K_t m_\chi^2(\frac{128m_\chi^2-160m_f^2}{m_\phi^6})$	$K_t m_\chi^2(\frac{32m_f^2}{m_\phi^6})$
$1, 6 + 3, 4$	0	$-K_t(\frac{64m_\chi^2-32m_f^2}{m_\phi^4})$	$-K_t(\frac{64m_\chi^2-32m_f^2}{m_\phi^4})$
$2, 3$	$-\omega m_\chi^2(\frac{192m_\chi^2}{m_\phi^6})$	0	$K_t m_\chi^2(\frac{64m_\chi^2}{m_\phi^6})$
$2, 5$	$\omega m_\chi^4(\frac{256m_\chi^2-256m_f^2}{m_\phi^8})$	$-K_t m_\chi^2(\frac{64m_\chi^2}{3m_\phi^8})$	$-K_t m_\chi^2(\frac{64m_\chi^2}{3m_\phi^8})$
$2, 6 + 3, 5$	$-\omega m_\chi^2(\frac{128m_\chi^2+32m_f^2}{m_\phi^6})$	$K_t m_\chi^2(\frac{32m_f^2}{m_\phi^6})$	$K_t m_\chi^2(\frac{128m_\chi^2-160m_f^2}{m_\phi^6})$
$3, 6$	$\omega(\frac{32m_\chi^2+16m_f^2}{m_\phi^4})$	$-K_t(\frac{8m_f^2}{m_\phi^4})$	$-K_t(\frac{64m_\chi^2-32m_f^2}{m_\phi^4})$
$4, 5$	$-\omega m_\chi^2(\frac{192m_\chi^2}{m_\phi^6})$	$K_t m_\chi^2(\frac{64m_\chi^2}{m_\phi^6})$	0
$4, 6$	$-\omega(\frac{64m_\chi^2-32m_f^2}{m_\phi^4})$	$-K_t(\frac{32m_\chi^2}{m_\phi^4})$	$-K_t(\frac{32m_\chi^2}{m_\phi^4})$
$5, 6$	$\omega m_\chi^2(\frac{64m_\chi^2-32m_f^2}{m_\phi^6})$	0	$K_t m_\chi^2(\frac{64m_\chi^2}{m_\phi^6})$

Table 5.8: *The finite real photon contributions from various diagrams: the* thermal photon $\widetilde{G}$ *contribution (Eq. 5.14)* $Int^{\widetilde{G}}_{i,j}$*, and the* thermal fermion and anti-fermion *contributions* $Int^{f}_{i,j}$ *(Eq. 5.18) and* $Int^{\overline{f}}_{i,j}$ *contributions. The total NLO thermal cross section is given by the sum of these contributions with the finite* $\widetilde{K}$ *combination,* $Int^{\widetilde{K}_{fin}}_{i,j}$ *(see Table 5.1) and the finite remainder from the collinear contributions.*

where the contributions shown are the sum of the real and virtual contributions, so that the collinear divergence has cancelled between the two, leaving this finite remainder. Hence, the total finite thermal cross section from both virtual and real photon corrections at NLO is given by the sum of the virtual component computed in Chapter 4, the real component (see Eq. 5.23) where the soft IR divergence has cancelled between the real and virtual parts, and the finite remainder from the sum of the collinear real and virtual parts (see Eq. 5.24). It can be seen that each term is individually helicity suppressed. Hence the addition of real photon emission/absorption to the leading order process $\chi\chi \to f\bar{f}$ does not lift the helicity suppression, so that the contribution is suppressed, just as was the case with the LO and the virtual NLO result. Adding these to the virtual contribution that was computed in Chapter 4; see Eq. 4.58, the total thermal contribution to the dark matter annihilation cross section from $\chi\chi \to f\bar{f}$ as well as $\chi\chi \to f\bar{f}(\gamma)$ is given, to order $\mathcal{O}(\alpha T^2/m_\chi^2)$, by

$$\sigma_{NLO}^{Real+Virtual} v_{rel} = \frac{\alpha|\lambda|^4}{128} \frac{T^2}{m_\chi^2} m_f^2 \left[\frac{32}{3m_\phi^4} + \frac{80m_\chi^2}{3m_\phi^6} + \frac{544m_\chi^4}{9m_\phi^8} \right] . \tag{5.25}$$

As mentioned earlier, the thermal average of this NLO cross section, added to the LO term shown in Eq. 4.9, is the collision term at order $\mathcal{O}(T^2/m_\chi^2)$, which determines how the DM relic density evolved as the Universe cooled [132]. Both the LO and NLO contributions are helicity suppressed. This is in contrast to the case when the dark matter particles are Dirac type fermions, which we briefly discuss below.

5.2.5.1 Thermal real photon cross section for Dirac dark matter

As seen in Eq. 4.12, the LO cross section when the dark matter particles are of Dirac type is not helicity suppressed. In this case, only the t-channel diagrams contribute to the cross section. It turns out that the thermal cross section in this case is also not helicity suppressed. Extracting only the t-channel terms, we have, in the non-relativistic limit, the

s-wave contribution,

$$\sigma_{NLO}^{Real,Dirac} = \frac{\alpha|\lambda|^4}{128 v_{rel}} \frac{T^2}{m_\chi^2} \left[\frac{16m_\chi^2 + 5m_f^2}{3m_\phi^4} + \frac{32m_\chi^2(m_\chi^2 - m_f^2)}{3m_\phi^6} + \frac{32m_\chi^4(2m_\chi^2 - 3m_f^2)}{3m_\phi^8} \right] . \tag{5.26}$$

The finite contribution from the collinear terms is given by

$$\sigma_{NLO}^{Coll,Dirac} = \frac{\alpha|\lambda|^4}{128 v_{rel}} \frac{T^2}{m_\chi^2} \left[\frac{40m_\chi^2 + 18m_f^2}{3m_\phi^4} + \frac{32m_\chi^2(2m_\chi^2 - m_f^2)}{3m_\phi^6} \right] . \tag{5.27}$$

The total NLO cross section from both virtual (see Eq. 4.59) and real photon annihilation processes for Dirac dark matter is then

$$\sigma_{NLO}^{\text{Real+Virtual,Dirac}} = \frac{\alpha|\lambda|^4}{128 v_{rel}} \frac{T^2}{m_\chi^2} \left[\frac{4(8m_\chi^2 + 3m_f^2)}{3m_\phi^4} + \frac{16m_\chi^2(8m_\chi^2 - 5m_f^2)}{3m_\phi^6} + \frac{96m_\chi^4(2m_\chi^2 - 3m_f^2)}{3m_\phi^8} \right] . \tag{5.28}$$

The *ratio* of the NLO thermal correction to the LO cross section for both Majorana and Dirac dark matter particles in the s-wave limit has the same dependence:

$$\frac{\sigma_{NLO}}{\sigma_{LO}}(\text{Majorana}) = \frac{\alpha\pi}{6} \frac{T^2}{m_\chi^2} = \frac{\sigma_{NLO}}{\sigma_{LO}}(\text{Dirac}) , \tag{5.29}$$

with an extra factor of 32 in the Dirac case. Here we have considered the leading $\mathcal{O}(1/m_\phi^4)$ term in both cases[2].

---

[2] Of course, the cross section *to* order $\mathcal{O}(\alpha)$ is the sum of the LO and NLO part; hence when we refer to the "NLO" cross section here, we mean *only* the $\mathcal{O}(\alpha)$ contribution.

Chapter 6

Conclusions and Outlook

Conclusion

In this thesis we presented the finite temperature corrections to the annihilation cross section of both Majorana- and Dirac- type dark matter candidates, considering a model in which the dark matter, χ, annihilates to Standard Model fermions via a scalar portal having Yukawa interaction, $\mathcal{L} \supset (\lambda\, \overline{\chi} P_L f^- \phi^+ + h.c.)$; see Eq. 1.8. From observations we know that the abundance of cold dark matter is encoded in its relic density having the present value $\Omega_c h^2 = 0.120 \pm 0.001$ (or alternatively, as $\Omega_c = 0.265(7)$). As the precision on the value of Ω_c is now at the third decimal place and will improve further with state-of-the-art technologies, we need to improve the precision with which we calculate and predict theoretically the relic abundance of dark matter. This is obtained by solving Boltzmann's equation, Eq. 1.5, which uses the thermal average of the dark matter annihilation cross section as an input, viz., the collision term that determines the evolution of the dark matter densities. Corrections to the annihilation cross section directly impact the relic abundance of the dark matter in theoretical models. Hence there is necessity of calculation of higher order corrections to this annihilation cross section.

Higher order corrections to dark matter annihilation cross sections are broadly calculated in quantum field theory at zero temperature. Extra precision on the annihilation cross section can be achieved by considering the finite temperature corrections which are taken care of in the framework of thermal field theory. In addition, it is known that the evolution of the dark matter density in the Universe occurs at high temperatures. While the *thermal average* of the collision term $\langle \sigma v_{rel} \rangle$ is used in the Boltzmann equation, see Eq. 1.5, the cross section that is used is itself calculated at zero temperature. Hence consistency also demands that thermal corrections to the cross section be included. In this thesis, we have computed the next-to-leading order (in the electromagnetic coupling α) thermal corrections to the dark matter annihilation cross section $\sigma(\chi\chi \to f\overline{f})$ with both virtual and real photon insertions using the techniques of thermal field theory. The corrections are small, of order T^2/m_χ^2, but can be significant in freeze-in scenarios, and with improved precision measurements.

This thesis was started with a brief overview of the relevant areas involved in our work. This included a short introduction to the Standard Model of Particle Physics and Cosmology, and evidences for dark matter through the CMB power spectrum, Lyman-alpha and 21 cm spectral lines, and presence in galaxy clusters and galaxy were presented. Some production mechanisms for dark matter, such as freeze-out, elastic decoupling, freeze-in and Schwinger mechanism were presented. Some dark matter models such as cannibal dark matter, axions and ALPS were also discussed. A brief discussion on various detection techniques—indirect and direct detection and detection through collider searches—for dark matter were presented. We also discussed the motive of this thesis which is to obtain the finite temperature corrections to dark matter annihilation cross sections. In this context, the Boltzmann equation for obtaining dark matter relic densities was also discussed. The model used for this study was also described.

In order to obtain finite temperature correction we need to implement techniques of thermal field theory [114, 139]. We discussed next the real time formalism for thermal field theory and presented the expressions for the thermally modified propagators for scalars, fermions, and photons, as well as modifications to vertices and phase space factors, necessary since we have particle emission into, and absorption from the heat bath.

A major problem which one encounters is divergences in the infrared limit which are much more severe in the finite temperature field theory due to presence of the photon distribution function, $n_B(\omega)$; see Eq. 2.19.

Both the NLO virtual photon corrections to $\chi\overline{\chi} \to f\overline{f}$ and the real photon corrections to $\chi\chi \to f\overline{f}(\gamma)$ contain IR divergences which we dealt with using the Grammer and Yennie technique [126–129]. We briefly described the key features of this technique, which recognises that the divergences arise from the photon sector, while the fermion sector contributes only IR-finite terms. The Grammer and Yennie procedure separates the factor $g_{\mu\nu}$ in the photon propagator (for virtual photons; see Eq. 3.2) and in the photon phase space (arising from the photon polarisation sum in the squared matrix element; see Eq. 3.18), into IR-safe G- (or $\widetilde{G}$-) photon and IR divergent K- (or $\widetilde{K}$-) photon parts (see Eq. 3.2, which greatly simplifies the calculations since the soft IR divergences among K and $\widetilde{K}$ get canceled among each other, as occurs at zero temperature.

After discussing the basic tools for obtaining dark matter annihilation cross section, we presented details of the tree level cross section for $\chi\overline{\chi} \to f\overline{f}$, considering dark matter to be both Majorana type and Dirac type in separate calculations. We then went on to calculate the thermal NLO corrections.

We implemented the Grammer and Yennie technique and calculated the finite contribution to the virtual thermal NLO corrections to the annihilation process. These arise from the thermal parts of the various photon, fermion, and anti-fermion propagators in the contributing Diagrams 1–7, shown in Figs. 4.2, 4.3, and 4.4. We need to use the Grammer and Yennie technique only for the photon thermal contributions since the thermal fermion contributions are IR finite. However, we found that all thermal contributions (from photons, fermions and anti-fermions) contained collinear divergences which also cancelled against analogous contributions from real photon thermal insertions. In our calculations we have taken mass of the mediator scalar to be heavy in comparison to other particles in the heat bath, $m_\phi \gg m_\chi \gtrapprox m_f$, and calculated the $O(T^2)$ finite corrections from the NLO virtual photon insertions.

After the discussion on finite temperate correction to virtual photon insertions, we moved to the finite temperature corrections due to real photon emission and absorption. We again used the Grammer and Yennie technique and explicitly showed the cancellation of IR divergences among the K and $\widetilde{K}$ thermal photon contributions, diagram by diagram; see Table 5.1. For this, we first demonstrated the real–virtual photon correspondence in Section 5.2.2. In addition, we also showed the cancellation of the collinear logarithmic terms, diagram by diagram, in the collinear limit when the fermion mass vanishes; see Tables 4.6, 4.7, and 4.8. Finally, we computed the finite remainder for both the virtual and real photon insertions, to obtain the total thermal corrections to the dark matter annihilation cross section at NLO. These are listed in Eqs. 4.11, 4.58, and 5.23 for the LO, NLO (virtual) and NLO (real) contributions for Majorana type dark matter, and in Eqs. 4.12, 4.59, and 5.26 for Dirac type dark matter. The summed total cross sections are given in Eqs. 5.25 and 5.28 for the Majorana and Dirac cases respectively.

The key findings of this thesis are as follows.

1. We have presented cancellation of soft IR divergences in the theory, implementing the generalized Grammer and Yennie technique in thermal field theory, taking virtual photon correction to the dark matter annihilation process, $\chi\overline{\chi} \to f\overline{f}$ and the real photon emission and absorption counterpart, $\chi\overline{\chi} \to f\overline{f}(\gamma)$. We show that these divergences cancel, diagram by diagram, between the real and virtual contributions.

2. Similarly, we demonstrate the cancellation of collinear divergences at NLO, between the real and virtual contributions.

3. We present the finite thermal corrections to dark matter annihilation cross sections at $O(T^2)$ for virtual and real photon corrections to the dark matter annihilation pro-

cess, assuming the heavy scalar limit.

4. We find that the NLO thermal contributions are helicity suppressed for Majorana dark matter (just as at LO), and not so for Dirac dark matter.

5. Interestingly, it turns out that the ratio of the thermal NLO corrections to LO correction (K-factor) has the same dependence for both Majorana and Dirac type dark matter:

$$\frac{\sigma_{NLO}}{\sigma_{LO}}(\text{Majorana}) = \frac{\alpha\pi}{6}\frac{T^2}{m_\chi^2} = \frac{\sigma_{NLO}}{\sigma_{LO}}(\text{Dirac})\,, \tag{6.1}$$

   with the ratio for the Dirac case being a factor of 32 times larger in the α dependent term. Considering thermal decoupling of dark matter in freeze-out scenario with $1/20 < T/m_\chi < 1/10$, we obtain a minute correction due to finite temperature effects. The contribution may be large in the case of freeze-in scenarios where T/m_χ is larger; this can be significant as the dark matter energy density in our Universe is being precisely determined with state-of-art techniques, having a current value $\Omega_c = 0.265(7)$. Note, however, that this is contingent on the Yukawa coupling λ being known (or better constrained).

Outlook and future directions

While the thermal corrections to the dark matter annihilation cross sections are found to be small, the inclusion of these corrections is required by consistency of the frame-work in which the dark matter relic density is computed using Boltzmann equations. Hence this work can be expanded to various dark matter models of interest; in fact, studies of astroparticle physics with finite temperate are rapidly growing. Possible scenarios can be freeze-in dark matter, coannihilation dark matter, hidden sector dark matter, inert doublet model and various others, where the impact of finite temperature on dark matter annihilation cross sections and relic abundance can be studied using thermal field theory.

Investigating the impact of finite temperature to the relic abundance of dark matter is our current future goal.

Bibliography

[1] S. Navas et al. “Review of particle physics”. In: *Phys. Rev. D* 110.3 (2024), p. 030001. DOI: `10.1103/PhysRevD.110.030001`.

[2] Prabhat Butola, D. Indumathi, and Pritam Sen. *Mathematica Notebooks for Dark Matter Annihilation Cross section at NLO*. `https://www.imsc.res.in/~indu/Academic/DarkMatter/`. Uploaded on 2025-06-03. 2025.

[3] N. Aghanim et al. “Planck 2018 results. VI. Cosmological parameters”. In: *Astron. Astrophys.* 641 (2020). [Erratum: Astron.Astrophys. 652, C4 (2021)], A6. DOI: `10.1051/0004-6361/201833910`. arXiv: `1807.06209 [astro-ph.CO]`.

[4] Louis E. Strigari. “Dark matter in dwarf spheroidal galaxies and indirect detection: a review”. In: *Rept. Prog. Phys.* 81.5 (2018), p. 056901. DOI: `10.1088/1361-6633/aaae16`. arXiv: `1805.05883 [astro-ph.CO]`.

[5] Wayne Hu. “Lecture Notes on CMB Theory: From Nucleosynthesis to Recombination”. In: (Feb. 2008). arXiv: `0802.3688 [astro-ph]`.

[6] Scott Dodelson. *Modern Cosmology*. Amsterdam: Academic Press, 2003. ISBN: 978-0-12-219141-1.

[7] Martin Bauer and Tilman Plehn. *Yet Another Introduction to Dark Matter: The Particle Physics Approach*. Vol. 959. Lecture Notes in Physics. Springer, 2019. DOI: `10.1007/978-3-030-16234-4`. arXiv: `1705.01987 [hep-ph]`.

[8] Steven R. Furlanetto. “Physical Cosmology From the 21-cm Line”. In: (Sept. 2019). arXiv: `1909.12430 [astro-ph.CO]`.

[9] Zixuan Xu, Quan Zhou, and Sibo Zheng. “Constraints on freeze-in dark matter from Lyman-α forest and 21-cm signal: Single-field models”. In: *Phys. Rev. D* 110.11 (2024), p. 115003. DOI: `10.1103/PhysRevD.110.115003`. arXiv: `2407.08225 [hep-ph]`.

[10] Quentin Decant et al. “Lyman-α constraints on freeze-in and superWIMPs”. In: *JCAP* 03 (2022), p. 041. DOI: `10.1088/1475-7516/2022/03/041`. arXiv: `2111.09321 [astro-ph.CO]`.

[11] Zixuan Xu and Sibo Zheng. “Lyman-α limit on axionlike cold dark matter”. In: *Phys. Rev. D* 111.6 (2025), p. 063525. DOI: `10.1103/PhysRevD.111.063525`. arXiv: `2410.15675 [hep-ph]`.

[12] Andi Hektor et al. “Constraints on ALPs and excited dark matter from the EDGES 21-cm absorption signal”. In: *Phys. Lett. B* 785 (2018), pp. 429–433. DOI: `10.1016/j.physletb.2018.09.009`. arXiv: `1805.09319 [hep-ph]`.

[13] Kevork Abazajian and Savvas M. Koushiappas. “Constraints on Sterile Neutrino Dark Matter”. In: *Phys. Rev. D* 74 (2006), p. 023527. DOI: `10.1103/PhysRevD.74.023527`. arXiv: `astro-ph/0605271`.

[14] Ioana A. Zelko et al. “Constraints on Sterile Neutrino Models from Strong Gravitational Lensing, Milky Way Satellites, and the Lyman-α Forest”. In: *Phys. Rev. Lett.* 129.19 (2022), p. 191301. DOI: `10.1103/PhysRevLett.129.191301`. arXiv: `2205.09777 [hep-ph]`.

[15] Keith R. Dienes et al. “Evaluating Lyman-α constraints for general dark-matter velocity distributions: Multiple scales and cautionary tales”. In: *Phys. Rev. D* 106.12 (2022), p. 123521. DOI: `10.1103/PhysRevD.106.123521`. arXiv: `2112.09105 [astro-ph.CO]`.

[16] F. Zwicky. “Die Rotverschiebung von extragalaktischen Nebeln”. In: *Helv. Phys. Acta* 6 (1933), pp. 110–127. DOI: `10.1007/s10714-008-0707-4`.

[17] David J. E. Marsh, David Ellis, and Viraf M. Mehta. *Dark Matter: Evidence, Theory, and Constraints*. Princeton Series in Astrophysics. Princeton University Press, Oct. 2024. ISBN: 978-0-691-24971-1, 978-0-691-24952-0. DOI: `10.1515/9780691249711`.

[18] Vera C. Rubin and W. Kent Ford Jr. “Rotation of the Andromeda Nebula from a Spectroscopic Survey of Emission Regions”. In: *Astrophys. J.* 159 (1970), pp. 379–403. DOI: `10.1086/150317`.

[19] V. C. Rubin, N. Thonnard, and W. K. Ford Jr. “Rotational properties of 21 SC galaxies with a large range of luminosities and radii, from NGC 4605 /R = 4kpc/ to UGC 2885 /R = 122 kpc/”. In: *Astrophys. J.* 238 (1980), p. 471. DOI: `10.1086/158003`.

[20] Elisa G. M. Ferreira. “Ultra-light dark matter”. In: *Astron. Astrophys. Rev.* 29.1 (2021), p. 7. DOI: `10.1007/s00159-021-00135-6`. arXiv: `2005.03254 [astro-ph.CO]`.

[21] Marco Battaglieri et al. “US Cosmic Visions: New Ideas in Dark Matter 2017: Community Report”. In: *U.S. Cosmic Visions: New Ideas in Dark Matter*. July 2017. arXiv: `1707.04591 [hep-ph]`.

[22] J. Silk et al. *Particle Dark Matter: Observations, Models and Searches*. Ed. by Gianfranco Bertone. Cambridge: Cambridge Univ. Press, 2010. ISBN: 978-1-107-65392-4. DOI: `10.1017/CBO9780511770739`.

[23] Eric Kuflik et al. “Elastically Decoupling Dark Matter”. In: *Phys. Rev. Lett.* 116.22 (2016), p. 221302. DOI: `10.1103/PhysRevLett.116.221302`. arXiv: `1512.04545 [hep-ph]`.

[24] Eric Kuflik et al. “Phenomenology of ELDER Dark Matter”. In: *JHEP* 08 (2017), p. 078. DOI: `10.1007/JHEP08(2017)078`. arXiv: `1706.05381 [hep-ph]`.

[25] Manuel A. Buen-Abad, Razieh Emami, and Martin Schmaltz. "Cannibal Dark Matter and Large Scale Structure". In: *Phys. Rev. D* 98.8 (2018), p. 083517. DOI: `10.1103/PhysRevD.98.083517`. arXiv: `1803.08062 [hep-ph]`.

[26] Duccio Pappadopulo, Joshua T. Ruderman, and Gabriele Trevisan. "Dark matter freeze-out in a nonrelativistic sector". In: *Phys. Rev. D* 94.3 (2016), p. 035005. DOI: `10.1103/PhysRevD.94.035005`. arXiv: `1602.04219 [hep-ph]`.

[27] Avirup Ghosh, Sourav Gope, and Satyanarayan Mukhopadhyay. "Cannibal dark matter decoupled from the standard model: Cosmological constraints". In: *Phys. Rev. D* 106.10 (2022), p. 103515. DOI: `10.1103/PhysRevD.106.103515`. arXiv: `2206.11046 [hep-ph]`.

[28] Marco Hufnagel and Michel H. G. Tytgat. "The domain of a cannibal dark matter". In: *JCAP* 09 (2023), p. 012. DOI: `10.1088/1475-7516/2023/09/012`. arXiv: `2212.09759 [hep-ph]`.

[29] Lawrence J. Hall et al. "Freeze-In Production of FIMP Dark Matter". In: *JHEP* 03 (2010), p. 080. DOI: `10.1007/JHEP03(2010)080`. arXiv: `0911.1120 [hep-ph]`.

[30] P. S. Bhupal Dev, Anupam Mazumdar, and Saleh Qutub. "Constraining Non-thermal and Thermal properties of Dark Matter". In: *Front. in Phys.* 2 (2014), p. 26. DOI: `10.3389/fphy.2014.00026`. arXiv: `1311.5297 [hep-ph]`.

[31] Mar Bastero-Gil et al. "Schwinger dark matter production". In: *JCAP* 10 (2024), p. 078. DOI: `10.1088/1475-7516/2024/10/078`. arXiv: `2312.15137 [hep-ph]`.

[32] Anson Hook. "TASI Lectures on the Strong CP Problem and Axions". In: *PoS* TASI2018 (2019), p. 004. DOI: `10.22323/1.333.0004`. arXiv: `1812.02669 [hep-ph]`.

[33] David J. E. Marsh. "Axions and ALPs: a very short introduction". In: *13th Patras Workshop on Axions, WIMPs and WISPs*. 2018, pp. 59–74. DOI: `10.3204/DESY-PROC-2017-02/marsh_david`. arXiv: `1712.03018 [hep-ph]`.

[34] R. D. Peccei. “The Strong CP problem and axions”. In: *Lect. Notes Phys.* 741 (2008). Ed. by Markus Kuster, Georg Raffelt, and Berta Beltran, pp. 3–17. DOI: `10.1007/978-3-540-73518-2_1`. arXiv: `hep-ph/0607268`.

[35] Ciaran O’Hare. *cajohare/AxionLimits: AxionLimits*. `https://cajohare.github.io/AxionLimits/`. Version v1.0. July 2020. DOI: `10.5281/zenodo.3932430`.

[36] Stefano Giagu. “WIMP Dark Matter Searches With the ATLAS Detector at the LHC”. In: *Front. in Phys.* 7 (2019), p. 75. DOI: `10.3389/fphy.2019.00075`.

[37] Tracy R. Slatyer. “Indirect detection of dark matter.” In: *Theoretical Advanced Study Institute in Elementary Particle Physics: Anticipating the Next Discoveries in Particle Physics*. 2018, pp. 297–353. DOI: `10.1142/9789813233348_0005`. arXiv: `1710.05137 [hep-ph]`.

[38] Jennifer M. Gaskins. “A review of indirect searches for particle dark matter”. In: *Contemp. Phys.* 57.4 (2016), pp. 496–525. DOI: `10.1080/00107514.2016.1175160`. arXiv: `1604.00014 [astro-ph.HE]`.

[39] Carlos Pérez de los Heros. “Status, Challenges and Directions in Indirect Dark Matter Searches”. In: *Symmetry* 12.10 (2020), p. 1648. DOI: `10.3390/sym12101648`. arXiv: `2008.11561 [astro-ph.HE]`.

[40] Dan Hooper. “TASI Lectures on Indirect Searches For Dark Matter”. In: *PoS* TASI2018 (2019), p. 010. arXiv: `1812.02029 [hep-ph]`.

[41] J. Berdugo. “Latest Results of the Alpha Magnetic Spectrometer on the International Space Station”. In: *Moscow Univ. Phys. Bull.* 77.2 (2022), pp. 71–82. DOI: `10.3103/S0027134922020126`.

[42] M. Aguilar et al. “The Alpha Magnetic Spectrometer (AMS) on the international space station: Part II — Results from the first seven years”. In: *Phys. Rept.* 894 (2021), pp. 1–116. DOI: `10.1016/j.physrep.2020.09.003`.

[43] R. Alfaro et al. “Searching for TeV Dark Matter in Irregular Dwarf Galaxies with HAWC Observatory”. In: *Astrophys. J.* 945.1 (2023), p. 25. DOI: 10.3847/1538-4357/acb5f1. arXiv: 2302.07929 [astro-ph.HE].

[44] Adila Abdul Halim et al. “Constraints on metastable superheavy dark matter coupled to sterile neutrinos with the Pierre Auger Observatory”. In: *Phys. Rev. D* 109.8 (2024), p. L081101. DOI: 10.1103/PhysRevD.109.L081101. arXiv: 2311.14541 [hep-ph].

[45] P. Abreu et al. “Limits to Gauge Coupling in the Dark Sector Set by the Nonobservation of Instanton-Induced Decay of Super-Heavy Dark Matter in the Pierre Auger Observatory Data”. In: *Phys. Rev. Lett.* 130.6 (2023), p. 061001. DOI: 10.1103/PhysRevLett.130.061001. arXiv: 2203.08854 [astro-ph.HE].

[46] Olivier Deligny. “Searches for ultra-high energy gamma-ray at the Pierre Auger Observatory and implications on super-heavy dark matter”. In: *13th Cosmic-Ray International Studies and Multi-messenger Astroparticle Conference*. July 2024. arXiv: 2408.00795 [astro-ph.HE].

[47] K. Choi et al. “Search for neutrinos from annihilation of captured low-mass dark matter particles in the Sun by Super-Kamiokande”. In: *Phys. Rev. Lett.* 114.14 (2015), p. 141301. DOI: 10.1103/PhysRevLett.114.141301. arXiv: 1503.04858 [hep-ex].

[48] K. Abe et al. “Search for Cosmic-Ray Boosted Sub-GeV Dark Matter Using Recoil Protons at Super-Kamiokande”. In: *Phys. Rev. Lett.* 130.3 (2023). [Erratum: Phys.Rev.Lett. 131, 159903 (2023)], p. 031802. DOI: 10.1103/PhysRevLett.130.031802. arXiv: 2209.14968 [hep-ex].

[49] R. Abbasi et al. “Search for dark matter from the center of the Earth with 10 years of IceCube data”. In: *Eur. Phys. J. C* 85.5 (2025), p. 490. DOI: 10.1140/epjc/s10052-025-14144-7. arXiv: 2412.12972 [astro-ph.HE].

[50] N. Aghanim et al. “Planck 2018 results. I. Overview and the cosmological legacy of Planck”. In: *Astron. Astrophys.* 641 (2020), A1. DOI: 10.1051/0004-6361/201833880. arXiv: 1807.06205 [astro-ph.CO].

[51] A. Albert et al. “Searching for Dark Matter Annihilation in Recently Discovered Milky Way Satellites with Fermi-LAT”. In: *Astrophys. J.* 834.2 (2017), p. 110. DOI: 10.3847/1538-4357/834/2/110. arXiv: 1611.03184 [astro-ph.HE].

[52] M. L. Ahnen et al. “Limits to Dark Matter Annihilation Cross-Section from a Combined Analysis of MAGIC and Fermi-LAT Observations of Dwarf Satellite Galaxies”. In: *JCAP* 02 (2016), p. 039. DOI: 10.1088/1475-7516/2016/02/039. arXiv: 1601.06590 [astro-ph.HE].

[53] Viviana Gammaldi et al. “Dark Matter search in dwarf irregular galaxies with the Fermi Large Area Telescope”. In: *PoS* ICRC2021 (2021), p. 509. DOI: 10.22323/1.395.0509. arXiv: 2109.11291 [astro-ph.CO].

[54] Marcin Misiaszek and Nicola Rossi. “Direct Detection of Dark Matter: A Critical Review”. In: *Symmetry* 16.2 (2024), p. 201. DOI: 10.3390/sym16020201. arXiv: 2310.20472 [hep-ph].

[55] Eugenio Del Nobile. “The Theory of Direct Dark Matter Detection: A Guide to Computations”. In: (Apr. 2021). DOI: 10.1007/978-3-030-95228-0. arXiv: 2104.12785 [hep-ph].

[56] Marc Schumann. “Direct Detection of WIMP Dark Matter: Concepts and Status”. In: *J. Phys. G* 46.10 (2019), p. 103003. DOI: 10.1088/1361-6471/ab2ea5. arXiv: 1903.03026 [astro-ph.CO].

[57] E. Aprile et al. “WIMP Dark Matter Search using a 3.1 tonne × year Exposure of the XENONnT Experiment”. In: (Feb. 2025). arXiv: 2502.18005 [hep-ex].

[58] E. Aprile et al. “Search for Light Dark Matter in Low-Energy Ionization Signals from XENONnT”. In: *Phys. Rev. Lett.* 134.16 (2025), p. 161004. DOI: 10.1103/PhysRevLett.134.161004. arXiv: 2411.15289 [hep-ex].

[59] E. Aprile et al. “First Search for Light Dark Matter in the Neutrino Fog with XENONnT”. In: *Phys. Rev. Lett.* 134.11 (2025), p. 111802. DOI: 10.1103/PhysRevLett.134.111802. arXiv: 2409.17868 [hep-ex].

[60] J. Aalbers et al. “Probing the scalar WIMP-pion coupling with the first LUX-ZEPLIN data”. In: *Commun. Phys.* 7.1 (2024), p. 292. DOI: 10.1038/s42005-024-01774-8. arXiv: 2406.02441 [hep-ex].

[61] Paolo Agnes. “Direct Detection of Dark Matter with DarkSide-20k”. In: *EPJ Web Conf.* 280 (2023), p. 06003. DOI: 10.1051/epjconf/202328006003.

[62] P. Agnes et al. “Constraints on Sub-GeV Dark-Matter–Electron Scattering from the DarkSide-50 Experiment”. In: *Phys. Rev. Lett.* 121.11 (2018), p. 111303. DOI: 10.1103/PhysRevLett.121.111303. arXiv: 1802.06998 [astro-ph.CO].

[63] M. F. Albakry et al. “Light dark matter constraints from SuperCDMS HVeV detectors operated underground with an anticoincidence event selection”. In: *Phys. Rev. D* 111.1 (2025), p. 012006. DOI: 10.1103/PhysRevD.111.012006. arXiv: 2407.08085 [hep-ex].

[64] M. F. Albakry et al. “Search for low-mass dark matter via bremsstrahlung radiation and the Migdal effect in SuperCDMS”. In: *Phys. Rev. D* 107.11 (2023), p. 112013. DOI: 10.1103/PhysRevD.107.112013. arXiv: 2302.09115 [hep-ex].

[65] D. W. Amaral et al. “Constraints on low-mass, relic dark matter candidates from a surface-operated SuperCDMS single-charge sensitive detector”. In: *Phys. Rev. D* 102.9 (2020), p. 091101. DOI: 10.1103/PhysRevD.102.091101. arXiv: 2005.14067 [hep-ex].

[66] G. Angloher et al. “Probing low WIMP masses with the next generation of CRESST detector”. In: (Mar. 2015). arXiv: 1503.08065 [astro-ph.IM].

[67] G. Angloher et al. “Light dark matter search using a diamond cryogenic detector”. In: *Eur. Phys. J. C* 84.3 (2024), p. 324. DOI: 10.1140/epjc/s10052-024-12647-3. arXiv: 2310.05815 [astro-ph.CO].

[68] R. Bernabei et al. “Main results and perspectives on other rare processes with DAMA experiments”. In: *Int. J. Mod. Phys. A* 31.31 (2016), p. 1642010. DOI: 10.1142/S0217751X16420100.

[69] E. Adams et al. “Search for inelastic dark matter-nucleus scattering with the PICO-60 CF3I and C3F8 bubble chambers”. In: *Phys. Rev. D* 108.6 (2023), p. 062003. DOI: 10.1103/PhysRevD.108.062003. arXiv: 2301.08993 [astro-ph.CO].

[70] G. Carosi et al. “Search for Axion Dark Matter from 1.1 to 1.3 GHz with ADMX”. In: (Apr. 2025). arXiv: 2504.07279 [hep-ex].

[71] Zhou Huang et al. “Constraints on the axial-vector and pseudo-scalar mediated WIMP-nucleus interactions from PandaX-4T experiment”. In: *Phys. Lett. B* 834 (2022), p. 137487. DOI: 10.1016/j.physletb.2022.137487. arXiv: 2208.03626 [hep-ex].

[72] Xuyang Ning et al. “Search for Light Dark Matter from the Atmosphere in PandaX-4T”. In: *Phys. Rev. Lett.* 131.4 (2023), p. 041001. DOI: 10.1103/PhysRevLett.131.041001. arXiv: 2301.03010 [hep-ex].

[73] Shuaijie Li et al. “Search for Light Dark Matter with Ionization Signals in the PandaX-4T Experiment”. In: *Phys. Rev. Lett.* 130.26 (2023), p. 261001. DOI: 10.1103/PhysRevLett.130.261001. arXiv: 2212.10067 [hep-ex].

[74] Tao Li et al. “Search for MeV-Scale Axionlike Particles and Dark Photons with PandaX-4T”. In: *Phys. Rev. Lett.* 134.7 (2025), p. 071004. DOI: 10.1103/PhysRevLett.134.071004. arXiv: 2409.00773 [hep-ex].

[75] Xiaopeng Zhou et al. “A Search for Solar Axions and Anomalous Neutrino Magnetic Moment with the Complete PandaX-II Data”. In: *Chin. Phys. Lett.* 38.1 (2021). [Erratum: Chin.Phys.Lett. 38, 109902 (2021)], p. 011301. DOI: 10.1088/0256-307X/38/10/109902. arXiv: 2008.06485 [hep-ex].

[76] Oliver Buchmueller, Caterina Doglioni, and Lian Tao Wang. “Search for dark matter at colliders”. In: *Nature Phys.* 13.3 (2017), pp. 217–223. DOI: `10.1038/nphys4054`. arXiv: `1912.12739 [hep-ex]`.

[77] Antonio Boveia and Caterina Doglioni. “Dark Matter Searches at Colliders”. In: *Ann. Rev. Nucl. Part. Sci.* 68 (2018), pp. 429–459. DOI: `10.1146/annurev-nucl-101917-021008`. arXiv: `1810.12238 [hep-ex]`.

[78] Georges Aad et al. “Search for displaced leptons in $\sqrt{s}$ = 13 TeV and 13.6 TeV pp collisions with the ATLAS detector”. In: (Oct. 2024). arXiv: `2410.16835 [hep-ex]`.

[79] Georges Aad et al. “Search for Light Long-Lived Particles in pp Collisions at s=13 TeV Using Displaced Vertices in the ATLAS Inner Detector”. In: *Phys. Rev. Lett.* 133.16 (2024), p. 161803. DOI: `10.1103/PhysRevLett.133.161803`. arXiv: `2403.15332 [hep-ex]`.

[80] Georges Aad et al. “Search for Heavy Neutral Leptons in Decays of W Bosons Using a Dilepton Displaced Vertex in s=13 TeV pp Collisions with the ATLAS Detector”. In: *Phys. Rev. Lett.* 131.6 (2023), p. 061803. DOI: `10.1103/PhysRevLett.131.061803`. arXiv: `2204.11988 [hep-ex]`.

[81] Vladimir Chekhovsky et al. “Search for dark matter produced in association with one or two top quarks in proton-proton collisions at $\sqrt{s}$ = 13 TeV”. In: (May 2025). arXiv: `2505.05300 [hep-ex]`.

[82] Vladimir Chekhovsky et al. “Search for dark matter production in association with a single top quark in proton-proton collisions at $\sqrt{s}$ = 13 TeV”. In: (Mar. 2025). arXiv: `2503.20033 [hep-ex]`.

[83] “Search for dark matter recoiling from a low-multiplicity jet in proton-proton collisions at 13 TeV”. In: (2025).

[84] Roel Aaij et al. "Search for $A' \to \mu^+\mu^-$ Decays". In: *Phys. Rev. Lett.* 124.4 (2020), p. 041801. DOI: 10.1103/PhysRevLett.124.041801. arXiv: 1910.06926 [hep-ex].

[85] Roshan Mammen Abraham et al. "Shining light on the dark sector: search for axion-like particles and other new physics in photonic final states with FASER". In: *JHEP* 01 (2025), p. 199. DOI: 10.1007/JHEP01(2025)199. arXiv: 2410.10363 [hep-ex].

[86] Henso Abreu et al. "Search for dark photons with the FASER detector at the LHC". In: *Phys. Lett. B* 848 (2024), p. 138378. DOI: 10.1016/j.physletb.2023.138378. arXiv: 2308.05587 [hep-ex].

[87] Alexey Boyarsky et al. "Searches for new physics at SND@LHC". In: *JHEP* 03 (2022), p. 006. DOI: 10.1007/JHEP03(2022)006. arXiv: 2104.09688 [hep-ph].

[88] Matti Kalliokoski et al. "Searching for minicharged particles at the energy frontier with the MoEDAL-MAPP experiment at the LHC". In: *JHEP* 04 (2024), p. 137. DOI: 10.1007/JHEP04(2024)137. arXiv: 2311.02185 [hep-ph].

[89] Yu. M. Andreev et al. "Searching for Light Dark Matter and Dark Sectors with the NA64 experiment at the CERN SPS". In: (May 2025). arXiv: 2505.14291 [hep-ex].

[90] Yu. M. Andreev et al. "Search for Light Dark Matter with NA64 at CERN". In: *Phys. Rev. Lett.* 131.16 (2023), p. 161801. DOI: 10.1103/PhysRevLett.131.161801. arXiv: 2307.02404 [hep-ex].

[91] Yu. M. Andreev et al. "Proof of principle for a light dark matter search with low-energy positron beams at NA64". In: (Feb. 2025). arXiv: 2502.04053 [hep-ex].

[92] *Electron Magnetic Moment*. https://physics.nist.gov/cgi-bin/cuu/Value?muem/.

[93] Anthony DiFranzo et al. "Simplified Models for Dark Matter Interacting with Quarks". In: *JHEP* 11 (2013). [Erratum: JHEP 01, 162 (2014)], p. 014. DOI: 10.1007/JHEP11(2013)014. arXiv: 1308.2679 [hep-ph].

[94] Martin Beneke, Francesco Dighera, and Andrzej Hryczuk. "Relic density computations at NLO: infrared finiteness and thermal correction". In: *JHEP* 10 (2014). [Erratum: JHEP 07, 106 (2016)], p. 045. DOI: 10.1007/JHEP10(2014)045. arXiv: 1409.3049 [hep-ph].

[95] Manuel Drees and Jie Gu. "Enhanced One-Loop Corrections to WIMP Annihilation and their Thermal Relic Density in the Coannihilation Region". In: *Phys. Rev. D* 87.6 (2013), p. 063524. DOI: 10.1103/PhysRevD.87.063524. arXiv: 1301.1350 [hep-ph].

[96] J. Harz et al. "One-loop corrections to neutralino-stop coannihilation revisited". In: *Phys. Rev. D* 91.3 (2015), p. 034028. DOI: 10.1103/PhysRevD.91.034028. arXiv: 1409.2898 [hep-ph].

[97] Michael Klasen, Florian Lyonnet, and Farinaldo S. Queiroz. "NLO+NLL collider bounds, Dirac fermion and scalar dark matter in the B–L model". In: *Eur. Phys. J. C* 77.5 (2017), p. 348. DOI: 10.1140/epjc/s10052-017-4904-8. arXiv: 1607.06468 [hep-ph].

[98] Kalle Ala-Mattinen and Kimmo Kainulainen. "Precision calculations of dark matter relic abundance". In: *JCAP* 09 (2020), p. 040. DOI: 10.1088/1475-7516/2020/09/040. arXiv: 1912.02870 [hep-ph].

[99] Martin Beneke, Robert Szafron, and Kai Urban. "Wino potential and Sommerfeld effect at NLO". In: *Phys. Lett. B* 800 (2020), p. 135112. DOI: 10.1016/j.physletb.2019.135112. arXiv: 1909.04584 [hep-ph].

[100] Martin Beneke, Robert Szafron, and Kai Urban. "Sommerfeld-corrected relic abundance of wino dark matter with NLO electroweak potentials". In: *JHEP* 02 (2021), p. 020. DOI: 10.1007/JHEP02(2021)020. arXiv: 2009.00640 [hep-ph].

[101] Matthew Baumgart et al. “Snowmass White Paper: Effective Field Theories for Dark Matter Phenomenology”. In: (Mar. 2022). arXiv: `2203.08204 [hep-ph]`.

[102] Andrzej Czarnecki et al. “Charged Particle Decay at Finite Temperature”. In: *Phys. Rev. D* 85 (2012), p. 025018. doi: `10.1103/PhysRevD.85.025018`. arXiv: `1110.2171 [hep-ph]`.

[103] Simone Biondini et al. “An effective field theory for non-relativistic Majorana neutrinos”. In: *JHEP* 12 (2013), p. 028. doi: `10.1007/JHEP12(2013)028`. arXiv: `1307.7680 [hep-ph]`.

[104] Simone Biondini et al. “CP asymmetry in heavy Majorana neutrino decays at finite temperature: the nearly degenerate case”. In: *JHEP* 03 (2016). [Erratum: JHEP 08, 072 (2016)], p. 191. doi: `10.1007/JHEP03(2016)191`. arXiv: `1511.02803 [hep-ph]`.

[105] Simone Biondini et al. “Effective field theories for dark matter pairs in the early universe: cross sections and widths”. In: *JHEP* 07 (2023), p. 006. doi: `10.1007/JHEP07(2023)006`. arXiv: `2304.00113 [hep-ph]`.

[106] Tobias Binder et al. “Non-Abelian electric field correlator at NLO for dark matter relic abundance and quarkonium transport”. In: *JHEP* 01 (2022), p. 137. doi: `10.1007/JHEP01(2022)137`. arXiv: `2107.03945 [hep-ph]`.

[107] I. Y. Park and P. Y. Wui. “Influence of finite-temperature effects on CMB power spectrum”. In: (Mar. 2025). arXiv: `2503.07469 [astro-ph.CO]`.

[108] Munshi G. Mustafa, Aritra Bandyopadhyay, and Chowdhury Aminul Islam. “Thermal Field Theory in the Presence of a Background Magnetic Field and its Application to QCD”. In: (Feb. 2025). arXiv: `2503.00075 [nucl-th]`.

[109] G. Jackson and M. Laine. “QED corrections to the thermal neutrino interaction rate”. In: *JHEP* 05 (2024), p. 089. doi: `10.1007/JHEP05(2024)089`. arXiv: `2312.07015 [hep-ph]`.

[110] S. Biondini, M. Eriksson, and M. Laine. “Computing singlet scalar freeze-out with plasmon and plasmino states”. In: (May 2025). arXiv: 2505.05206 [hep-ph].

[111] Pedro Bittar, Subhojit Roy, and Carlos E. M. Wagner. “Self Consistent Thermal Resummation: A Case Study of the Phase Transition in 2HDM”. In: (Apr. 2025). arXiv: 2504.02024 [hep-ph].

[112] M. Laine. “Resonant s-channel dark matter annihilation at NLO”. In: *JHEP* 01 (2023), p. 157. DOI: 10.1007/JHEP01(2023)157. arXiv: 2211.06008 [hep-ph].

[113] Torbjörn Lundberg and Roman Pasechnik. “Thermal Field Theory in real-time formalism: concepts and applications for particle decays”. In: *Eur. Phys. J. A* 57.2 (2021), p. 71. DOI: 10.1140/epja/s10050-020-00288-5. arXiv: 2007.01224 [hep-th].

[114] Michel Le Bellac. *Thermal Field Theory*. Cambridge Monographs on Mathematical Physics. Cambridge University Press, Mar. 2011. ISBN: 978-0-511-88506-8, 978-0-521-65477-7. DOI: 10.1017/CBO9780511721700.

[115] Takeo Matsubara. “A New approach to quantum statistical mechanics”. In: *Prog. Theor. Phys.* 14 (1955), pp. 351–378. DOI: 10.1143/PTP.14.351.

[116] H. Matsumoto et al. “Thermo Field Dynamics in Interaction Representation”. In: *Prog. Theor. Phys.* 70 (1983), pp. 599–602. DOI: 10.1143/PTP.70.599.

[117] Paul C. Martin and Julian S. Schwinger. “Theory of many particle systems. 1.” In: *Phys. Rev.* 115 (1959). Ed. by K. A. Milton, pp. 1342–1373. DOI: 10.1103/PhysRev.115.1342.

[118] L. V. Keldysh. “Diagram Technique for Nonequilibrium Processes”. In: *Sov. Phys. JETP* 20 (1965), pp. 1018–1026. DOI: 10.1142/9789811279461_0007.

[119] Ryogo Kubo. “Statistical mechanical theory of irreversible processes. 1. General theory and simple applications in magnetic and conduction problems”. In: *J. Phys. Soc. Jap.* 12 (1957), pp. 570–586. DOI: 10.1143/JPSJ.12.570.

[120] R. L. Kobes and G. W. Semenoff. “Discontinuities of Green Functions in Field Theory at Finite Temperature and Density”. In: *Nucl. Phys. B* 260 (1985), pp. 714–746. DOI: 10.1016/0550-3213(85)90056-2.

[121] Antti J. Niemi and Gordon W. Semenoff. “Thermodynamic Calculations in Relativistic Finite Temperature Quantum Field Theories”. In: *Nucl. Phys. B* 230 (1984), pp. 181–221. DOI: 10.1016/0550-3213(84)90123-8.

[122] R. J. Rivers. *PATH INTEGRAL METHODS IN QUANTUM FIELD THEORY*. Cambridge Monographs on Mathematical Physics. Cambridge University Press, Oct. 1988. ISBN: 978-0-521-36870-4, 978-1-139-24186-1. DOI: 10.1017/CBO9780511564055.

[123] T. Altherr. “Introduction to thermal field theory”. In: *Int. J. Mod. Phys. A* 8 (1993), pp. 5605–5628. DOI: 10.1142/S0217751X93002216. arXiv: hep-ph/9307277.

[124] N. P. Landsman and C. G. van Weert. “Real and Imaginary Time Field Theory at Finite Temperature and Density”. In: *Phys. Rept.* 145 (1987), p. 141. DOI: 10.1016/0370-1573(87)90121-9.

[125] Ansgar Denner et al. “Feynman rules for fermion number violating interactions”. In: *Nucl. Phys. B* 387 (1992), pp. 467–481. DOI: 10.1016/0550-3213(92)90169-C.

[126] Pritam Sen, D. Indumathi, and Debajyoti Choudhury. “Infrared finiteness of a complete theory of charged scalars and fermions at finite temperature”. In: *Eur. Phys. J. C* 80.10 (2020), p. 972. DOI: 10.1140/epjc/s10052-020-08498-3.

[127] G. Grammer Jr. and D. R. Yennie. “Improved treatment for the infrared divergence problem in quantum electrodynamics”. In: *Phys. Rev. D* 8 (1973), pp. 4332–4344. DOI: 10.1103/PhysRevD.8.4332.

[128] D. R. Yennie, Steven C. Frautschi, and H. Suura. “The infrared divergence phenomena and high-energy processes”. In: *Annals Phys.* 13 (1961), pp. 379–452. DOI: 10.1016/0003-4916(61)90151-8.

[129] D. Indumathi. “Cancellation of infrared divergences at finite temperature”. In: *Annals Phys.* 263 (1998), pp. 310–339. DOI: 10.1006/aphy.1997.5758. arXiv: hep-ph/9607206.

[130] Pritam Sen, D. Indumathi, and Debajyoti Choudhury. “Infrared finiteness of a thermal theory of scalar electrodynamics to all orders”. In: *Eur. Phys. J. C* 79.6 (2019), p. 532. DOI: 10.1140/epjc/s10052-019-7001-3. arXiv: 1812.04247 [hep-ph].

[131] Prabhat Butola, D. Indumathi, and Pritam Sen. “NLO thermal corrections to dark matter annihilation cross sections: A novel approach”. In: *Phys. Rev. D* 110.3 (2024), p. 036006. DOI: 10.1103/PhysRevD.110.036006. arXiv: 2404.15987 [hep-ph].

[132] Paolo Gondolo and Graciela Gelmini. “Cosmic abundances of stable particles: Improved analysis”. In: *Nucl. Phys. B* 360 (1991), pp. 145–179. DOI: 10.1016/0550-3213(91)90438-4.

[133] Wolfram Research Inc. *Mathematica, Version 13.1*. Champaign, IL, 2022. 2022.

[134] P Butola, D. Indumathi, and P. Sen. *Mathematica Notebooks for Dark Matter Annihilation Cross section at NLO*. https://www.imsc.res.in/~indu/Academic/DarkMatter/. Uploaded on 2024-04-20. 2024.

[135] Martin Beneke, Francesco Dighera, and Andrzej Hryczuk. “Finite-temperature modification of heavy particle decay and dark matter annihilation”. In: *JHEP* 09 (2016), p. 031. DOI: 10.1007/JHEP09(2016)031. arXiv: 1607.03910 [hep-ph].

[136] Prabhat Butola, D. Indumathi, and Pritam Sen. “Thermal corrections to dark matter annihilation with real photon emission/absorption”. In: (June 2025). arXiv: 2506.07663 [hep-ph].

[137] Vladyslav Shtabovenko, Rolf Mertig, and Frederik Orellana. “FeynCalc 10: Do multiloop integrals dream of computer codes?” In: *Comput. Phys. Commun.* 306 (2025), p. 109357. DOI: 10.1016/j.cpc.2024.109357. arXiv: 2312.14089 [hep-ph].

[138] R. Mertig, M. Bohm, and Ansgar Denner. “FEYN CALC: Computer algebraic calculation of Feynman amplitudes”. In: *Comput. Phys. Commun.* 64 (1991), pp. 345–359. DOI: 10.1016/0010-4655(91)90130-D.

[139] Mikko Laine and Aleksi Vuorinen. *Basics of Thermal Field Theory*. Vol. 925. Springer, 2016. DOI: 10.1007/978-3-319-31933-9. arXiv: 1701.01554 [hep-ph].

Appendix A

Imaginary time formalism of Thermal field theory

This appendix we will be focused on imaginary time formalism of thermal field theory which we present for completeness. We start with the path integral formalism and obtain imaginary time propagator for the thermal field theory, first in quantum statistical mechanics and then in the thermal field theory for scalar fields.

A.1 Introduction to path integral formalism

Path integral formalism is a Lorentz invariant way of dealing with the problems in quantum mechanics and QFT. In order to obtain dynamics of the particle, we calculate probability amplitude in quantum mechanics. Probability amplitude for a finding a particle at location (q', t'), initially at location (q, t), in time independent potential V(q) is given by

$$F(q', t'; q, t) = \langle q' | e^{-i\hat{H}(t'-t)} | q \rangle \,. \tag{A.1}$$

For convenience we take probability amplitude, F in imaginary time, with following analytic continuation

$$t \to -i\tau \;\; t' \to -i\tau' \;, \tag{A.2}$$

$$F(q', -i\tau'; q, -i\tau) = \langle q' | e^{-\hat{H}(\tau'-\tau)} | q \rangle \;. \tag{A.3}$$

After performing usual procedure of path integral formalism we obtain

$$F(q', -i\tau'; q, -i\tau) = \int \mathcal{D}q(\tau'') \times \exp\Big[- \int_{\tau}^{\tau'} d\tau'' \Big(\frac{1}{2} m\dot{q}(\tau'') + V(q(\tau'')) \Big) \Big] \;. \tag{A.4}$$

Now defining Euclidean action S_E,

$$S_E(\tau' - \tau) := \int_{\tau}^{\tau'} d\tau'' \Big(\frac{1}{2} m\dot{q}(\tau'') + V(q(\tau'')) \Big) \;, \tag{A.5}$$

we end up with

$$F(q', -i\tau'; q, -i\tau) = \int \mathcal{D}q(\tau'') e^{-S_E(\tau'-\tau)} \;. \tag{A.6}$$

For dealing with system at finite temperature, we need analogous expression of probability amplitude (Eq. A.6) in quantum statistical mechanics. Partition function for a system with temperature T($\beta := 1/T$) for complete set of eigenvectors of Hamiltonian $\hat{H}$ is given by,

$$Z(\beta) = \mathrm{Tr}\, e^{-\beta\hat{H}} = \sum_n . e^{-\beta E_n} \;. \tag{A.7}$$

The partition function can be re-expressed for complete set of eigenvectors of position operator as

$$Z(\beta) = \int dq \langle q | e^{-\beta\widehat{H}} | q \rangle \;. \tag{A.8}$$

Comparing with equation Eq. A.3, one obtains

$$Z(\beta) = \int dqF(q, -i\beta; q, 0)\ . \tag{A.9}$$

Further, partition function $Z(\beta)$, can be reincarnated as,

$$Z(\beta) = \int \mathcal{D}q(\tau) \exp\Big[- \int_0^\beta d\tau\Big(\frac{1}{2}m\dot{q}^2(\tau) + V(q(\tau))\Big)\Big]\ . \tag{A.10}$$

Using the definition of Euclidean action from Eq. A.5, we obtain

$$Z(\beta) = \int \mathcal{D}q(\tau)e^{-S_E(\beta)}\ . \tag{A.11}$$

The boundary condition for this integral can be obtained from Eq. A.9:

$$q(\beta) = q(0)\ . \tag{A.12}$$

In order to obtain propagators, we need to define generating functional, $Z(\beta; j)$ ($Z(\beta) = Z(\beta; j = 0)$):

$$Z(\beta; j) = \int \mathcal{D}q(\tau)e^{\left(-S_E(\beta)+\int_0^\beta j(\tau)q(\tau)d\tau\right)}\ . \tag{A.13}$$

The propagator in imaginary time is obtained by functional differentiation of generating functional $Z(\beta; j)$ as follows,

$$\frac{1}{Z(\beta)}\frac{\delta^2 Z(\beta; j)}{\delta j(\tau_1)\delta j(\tau_2)}\bigg|_{j=0} = \frac{1}{Z(\beta)}\int \mathcal{D}q(\tau)q(\tau_1)q(\tau_2)e^{-S_E(\beta)}\ . \tag{A.14}$$

Then the thermal average of time-ordered product for position operator $\hat{q}$ in imaginary time is defined as

$$\langle T\{\hat{q}(-i\tau_1)\hat{q}(-i\tau_2)\}\rangle_\beta = \frac{1}{Z(\beta)}\,\mathrm{Tr}\,[e^{-\beta\hat{H}}T\{\hat{q}(-i\tau_1)\hat{q}(-i\tau_2)\}]\ . \tag{A.15}$$

By definition, thermal average on operator $\hat{A}$ is given by,

$$\langle \hat{A} \rangle_\beta = \frac{1}{Z(\beta)} \mathrm{Tr}(\hat{A} e^{-\beta \hat{H}}) \ . \tag{A.16}$$

The time-ordered product in imaginary time is defined as,

$$\begin{aligned} T\hat{q}(-i\tau_1)\hat{q}(-i\tau_2) &= \hat{q}(-i\tau_1)\hat{q}(-i\tau_2) \ if \ \tau_1 > \tau_2 \ , \\ &= \hat{q}(-i\tau_2)\hat{q}(-i\tau_1) \ if \ \tau_2 > \tau_1 \ . \end{aligned} \tag{A.17}$$

Functional differentiation of generating functional gives the thermal average of time ordered product of position operators; for $\tau_1 > \tau_2$, we have

$$Z(\beta)\langle T(\hat{q}(-i\tau_1)\hat{q}(-i\tau_2))\rangle_\beta = \int dq \langle q| e^{-(\beta-\tau_1)\hat{H}} \hat{q} e^{-(\tau_1-\tau_2)\hat{H}} \hat{q} e^{-\tau_2 \hat{H}} |q\rangle \ . \tag{A.18}$$

With method of path integral formalism, and inserting complete set of position operators at times τ_1 and τ_2 , generating functional $Z(\beta; j)$ takes the form,

$$Z(\beta; j) = \mathrm{Tr}\,[e^{-\beta \hat{H}} T(e^{\int_0^\beta d\tau j(\tau)\hat{q}(-i\tau)})] \ . \tag{A.19}$$

Using periodicity condition $q(\beta) = q(0)$, we have

$$\langle T\{(\hat{q}(-i\beta)\hat{q}(-i\tau)\}\rangle_\beta = \langle T\{\hat{q}(0)\hat{q}(-i\tau)\}\rangle \ . \tag{A.20}$$

Defining a function $\Delta(\tau) = \langle T(\hat{q}(-i\tau)\hat{q}(0)\rangle_\beta$ for $0 \le \tau \le \beta$, $\Delta(\tau)$ follows satisfies (this will later be shown to hold due to KMS relations):

$$\Delta(\tau - \beta) = \Delta(\tau) \ . \tag{A.21}$$

Taking potential for harmonic oscillator and considering $m = 1$ for simplicity

$$V(q) = \frac{1}{2}\omega^2 q^2 \,. \tag{A.22}$$

For this potential, the generating functional takes the form

$$\begin{aligned} Z(\beta; j) &= \int_{q(0)=q(\beta)} \mathcal{D}q(\tau) \exp\left[- \int_0^\beta d\tau \left(\frac{1}{2} q(\tau) \times \left(- \frac{d^2}{d\tau^2} + \omega^2 \right) q(\tau) - j(\tau) q(\tau) \right) \right] , \\ &= Z(\beta) \exp\left[\frac{1}{2} \int d\tau d\tau' \, j(\tau) K(\tau, \tau') j(\tau') \right] . \end{aligned} \tag{A.23}$$

Solving Eq. A.24 we get for Green's function $K(\tau, \tau')$,

$$\left(- \frac{d^2}{d\tau^2} + \omega^2 \right) K(\tau, \tau') = \delta(\tau - \tau') \,. \tag{A.24}$$

For free particle, with Eqs. A.14, A.24 and A.21 we obtain

$$K(\tau, \tau') = \Delta_f(\tau - \tau') \,. \tag{A.25}$$

For $0 \leq \tau \leq \beta$, we get

$$\begin{aligned} \Delta_F(\tau) &= \frac{1}{2\omega} [(1 + n(\omega)) e^{-\omega\tau} + n(\omega) e^{\omega\tau}] \,, \\ n(\omega) &= \frac{1}{e^{\beta|\omega|} - 1} \,. \end{aligned} \tag{A.26}$$

In order to obtain the time ordered product $T(\hat{q}(t)\hat{q}(t'))$ in real time 't' we define two-point correlators with real time as

$$\begin{aligned} D^>(t, t') &= \langle \hat{q}(t) \hat{q}(t') \rangle_\beta \,, \\ D^<(t, t') &= \langle \hat{q}(t') \hat{q}(t) \rangle_\beta = D^>(t', t) \,. \end{aligned} \tag{A.27}$$

$D^>(t,t')$ and $D^<(t,t')$ are related by $D^>(t,t') = D^<(t+i\beta,t')$, known to be the KMS relation. We can rewrite $D^>(t,t')$ after inserting a complete set of eigenvectors of the Hamiltonian

$$D^>(t,t') = \frac{1}{Z(\beta)} \sum_{n,m} e^{-\beta E_n} e^{iE_n(t-t')} \times e^{-iE_m(t-t')} \langle n|\hat{q}(0)|m\rangle \, . \tag{A.28}$$

Here, $D^>(t,t')$ is defined for $-\beta \leq Im(t-t') \leq 0$ (this can be seen from the fact that exponential with argument E_n in Eq. A.28 is convergent in the mentioned range) wheres $D^<(t,t')$ is defined for $\beta \geq Im(t-t') \geq 0$. Evolution of the state in the position space is obtained by the operation of imaginary time evolution operator $e^{-\beta\hat{H}}$ as

$$e^{-\beta\hat{H}}\hat{q}(t)e^{\beta\hat{H}} = \hat{q}(t+i\beta) \, . \tag{A.29}$$

Applying Eq. A.29 to $D^>(t,t')$ and using cyclicity of trace, we get $D^>(t,t') = D^<(t+i\beta,t')$, which is the KMS relation. In the range $0 \leq \tau \leq \beta$, imaginary time propagator $\Delta(\tau)$ is $\Delta(\tau) = D^>(-i\tau,0)$, so $\Delta(\tau-\beta) = \Delta(\tau)$. Time ordered product for real value of t and t' is defined as

$$\begin{aligned} D(t,t') &= \langle T\{\hat{q}(t)\hat{q}(t')\}\rangle \, , \\ &= \theta(t-t')D^>(t,t') + \theta(t'-t)D^<(t,t') \, . \end{aligned} \tag{A.30}$$

A.2 Spectral function $\rho(k_0)$

The two point functions depends on the spectral function, $\rho(k_0)$ (which can be interpreted as thermal average of the commutator $[\widehat{q}(t),\widehat{q}(0)]$):

$$\rho(k_0) = D^>(k_0) - D^<(k_0) \, . \tag{A.31}$$

Here $D^{\lessgtr}(k_0)$ are the Fourier transforms of $D^{\lessgtr}(t)$.

$$D^{\lessgtr}(k_0) = \int_{-\infty}^{\infty} dt e^{ik_0 t} D^{\lessgtr}(t) \,, \tag{A.32}$$

where $D^{\lessgtr}(t)$ is bookkeeping notation for $D^{\lessgtr}(t, 0)$. (We use definitions : $D^{>}(t) := D^{>}(t, 0)$ and $D^{<}(t) := D^{<}(t, 0)$). Applying the KMS conditions, one obtains the relation between $D^{>}(k_0)$ and $D^{<}(k_0)$ as

$$D^{<}(k_0) = e^{-\beta k_0} D^{>}(k_0) \,, \tag{A.33}$$

and by the definition of $D^{>}(k_0)$ and $D^{<}(k_0)$ we can deduce the following relationship

$$D^{<}(k_0) = D^{>}(-k_0) \,. \tag{A.34}$$

We now can reinterpret $D^{>}(k_0)$ and $D^{<}(k_0)$ in the form of spectral function $\rho(k_0)$ and distribution function $f(k_0) = 1/(e^{\beta k_0} - 1)$:

$$D^{>}(K_0) = (1 + f(k_0))\rho(k_0) \,, \qquad D^{<}(K_0) = f(k_0)\rho(k_0) \,. \tag{A.35}$$

In the process of getting the useful form of spectral function we recall definition of $D^{>}(t, t')$ for Eq. A.28 and extract $D^{>}(t)$ from it. With the use of the relation in Eq. A.34 and using the definition of spectral function in Eq. A.34, we obtain

$$\rho(k_0) = \frac{2\pi}{Z(\beta)} \sum_{n,m} e^{-\beta E_n} [\delta(k + E_n - E_m) - \delta(k + E_n - E_m)](|\langle n|\hat{q}(0)|m\rangle|)^2 \,. \tag{A.36}$$

The spectral function in Eq. A.36 has two important properties:

1. spectral function is odd real function of k_0. i.e. $\rho(k_0) = -\rho(-k_0)$,

2. spectral function obey positivity condition which is, $\text{sign}(k_0)\rho(k_0) > 0$.

We will be using $\epsilon(k_0)$ alternatively for sign(k_0) from here onward. Further we will find sum rule for spectral function , $\rho(k_0)$

We can differentiate the spectral function defined in Eq A.31 with respect to t to obtain following relation

$$i\frac{d}{dt}(D^{>}(t) - D^{<}(t)) = \int_{-\infty}^{\infty} \frac{dk_0}{2\pi} k_0 e^{-ik_0 t}(D^{>}(k_0) - D^{<}(k_0)) \ . \tag{A.37}$$

By definition of $D^{\lessgtr}(t)$ we have

$$D^{>}(t) - D^{<}(t) = \langle [\hat{q}(t), \hat{q}(0)] \rangle_{\beta} \ . \tag{A.38}$$

Using the commutation relation

$$[\hat{q}(t), \dot{\hat{q}}(t')] = i \ , \tag{A.39}$$

$$\text{so that } [\dot{\hat{q}}(t'), \hat{q}(0),] = -i \ , \tag{A.40}$$

we can write

$$\int_{-\infty}^{\infty} \frac{dk_0}{2\pi} k_0 e^{-ik_0 t} \rho(k_0) = 1 \ . \tag{A.41}$$

Here we retained $\rho(k_0)$ from Eq. A.31. In the limit $t \to 0$, Eq. A.41 gives the following sum rule

$$\int_{-\infty}^{\infty} \frac{dk_0}{2\pi} k_0 \rho(k_0) = 1 \ . \tag{A.42}$$

Next we find the free spectral propagator. By definition

$$\hat{q} = \frac{1}{\sqrt{2\omega}}(a e^{-i\omega t} + a^{\dagger} e^{i\omega t}) \ , \tag{A.43}$$

and we can rewrite $D^>(t) - D^<(t)$ as

$$D^>(t) - D^<(t) = \frac{1}{2\omega}\langle[a, a^\dagger]e^{-i\omega t} + [a^\dagger, a]e^{i\omega t}\rangle \, . \tag{A.44}$$

Using the property $[a, a^\dagger] = 1$ and taking Fourier transformation of $(D^>(t) - D^<(t))$ in Eq. A.44 we get the free spectral function $\rho_F(k_0)$:

$$\rho_F(k_0) = 2\pi\epsilon(k_0)\delta(k_0^2 - \omega^2) \, . \tag{A.45}$$

This spectral function is independent of temperature.

A.3 Imaginary-time propagator

We recall the imaginary time propagator, $\Delta(\tau) = \langle T(\hat{q}(-i\tau)\hat{q}(0))\rangle_\beta$. Defining its Fourier transform,

$$\Delta(i\omega_n) = \int_0^\beta d\tau e^{i\omega_n}\Delta(\tau) \, , \tag{A.46}$$

since the integral is over a finite interval $[0, \beta]$ we get the inverse Fourier transform in the discrete form as,

$$\Delta(\tau) = T\sum_n e^{-i\omega_n\tau}\Delta(i\omega_n) \, . \tag{A.47}$$

The periodicity condition $(\Delta(\tau - \beta) = \Delta(\tau))$ for finite time interval $[0, \beta]$ leads to discrete values of frequencies ω_n,

$$\omega_n = \frac{2\pi n}{\beta} \, , \tag{A.48}$$

where ω_n are known as **Matsubara frequencies**. The imaginary time propagator $\Delta(\tau) = D^{>}(-i\tau)$ in the interval $[0,\beta]$ can be written as

$$\Delta(\tau) = \int \frac{dk^0}{2\pi} e^{-k_0\tau} D^{>}(k_0)\,. \tag{A.49}$$

Using Eq. A.49 in Eq. A.47 we can rewrite $\Delta(i\omega_n)$ as

$$\begin{aligned}
\Delta(i\omega_n) &= \int_0^\beta d\tau e^{i\omega_n\tau} \int \frac{dk^0}{2\pi} e^{-k_0\tau} D^{>}(k_0)\,, \\
&= \int \frac{dk^0}{2\pi} \int_0^\beta d\tau e^{(i\omega_n - k_0)\tau} D^{>}(k_0)\,, &\text{(A.50)}\\
&= \int \frac{dk^0}{2\pi} \int_0^\beta d\tau e^{(i\omega_n - k_0)\tau} \rho(k_0)(1 + f(k_0)))\,. &\text{(A.51)}
\end{aligned}$$

The integral in Eq. A.51 further can be solved for discrete values of frequencies ω_n (in Eq. A.48) and distribution function $f(k_0)$ ($= e^{\beta k_0} - 1$), which further gives,

$$\Delta(i\omega_n) = -\int_{-\infty}^{\infty} \frac{dk_0}{2\pi} \frac{\rho(k_0)}{i\omega_n - k_0}\,. \tag{A.52}$$

In order to obtain the imaginary time propagator in free field case we use spectral function from Eq. A.51 which gives,

$$\Delta_F(i\omega_n) = \frac{1}{\omega_n^2 + \omega^2}\,. \tag{A.53}$$

The propagator in Eq. A.53 is the solution for Eq. A.52 for only discrete values of ω_n in Eq. A.48. In order to find the solution for continuous spectrum of ω_n, we have to perform analytic continuation on Eq. A.52. A unique analytic continuation can be done considering following two conditions

1. $|\Delta(z)| \to 0$, if $|z| \to \infty$,

2. $\Delta(z)$ is analytic outside the real axis.

The analytic continuation of Eq. A.52 is as follows:

$$\Delta(z) = -\int_{-\infty}^{\infty} \frac{dk_0}{2\pi} \frac{\rho(k_0)}{z - k_0} \, . \tag{A.54}$$

This analytic continuation is necessary for getting relation between retarded (advanced) propagators $D_R(t)$ ($D_A(t)$) and imaginary time propagator $\Delta(i\omega_n)$ in Eq. A.52. The retarded and advanced propagators are defined as

$$\begin{aligned} D_R(t) &= \langle \theta(t)[\hat{q}(t), \hat{q}(0)] \rangle_\beta \, , \\ D_A(t) &= -\langle \theta(-t)[\hat{q}(t), \hat{q}(0)] \rangle_\beta \, . \end{aligned} \tag{A.55}$$

In order to find the relation between retarded propagator and imaginary time propagator we will first take the Fourier transform of the retarded propagator in the momentum space with the use of Eq. A.32.

$$D_R(k_0) = \int_{-\infty}^{\infty} dt e^{ik_0 t} D_R(t) \, . \tag{A.56}$$

We use the representation of θ-function as follows:

$$\theta(t) = i \int_{-\infty}^{\infty} \frac{dk_0'}{2\pi} \frac{e^{-ik_0' t}}{k_0' + i\eta} \, . \tag{A.57}$$

With the use of Eq. A.56 and A.57 we get

$$D_R(k_0) = i \int_{-\infty}^{\infty} \frac{dk_0'}{2\pi} \int_{-\infty}^{\infty} dt \frac{e^{i(k_0 - k_0')t}}{k_0' + i\eta} \langle [\hat{q}(t), \hat{q}(0)] \rangle_\beta \, , \tag{A.58}$$

which, with the use of Eqs. A.31 and A.32 gives

$$D_R(k_0) = i \int_{-\infty}^{\infty} \frac{dk_0'}{2\pi} \frac{\rho(k_0 - k_0')}{k_0' + i\eta} \, . \tag{A.59}$$

With shift of the integral measure we can rewrite this propagator as

$$D_R(k_0) = i\int_{-\infty}^{\infty}\frac{dk_0'}{2\pi}\frac{\rho(k_0')}{k_0 - k_0' + i\eta}\,. \tag{A.60}$$

Now comparing Eq. A.60 with Eq. A.52 we can find the following relation between the retarded (advance) propagator and the imaginary time propagator as

$$D_R(k_0) = -i\Delta(k_0 + i\eta)\,, \tag{A.61}$$

$$D_A(k_0) = i\Delta(k_0 - i\eta)\,. \tag{A.62}$$

Since the free spectral function is temperature-independent, the free retarded and advance propagators will be independent of temperature. We next will find the time-ordered propagator where we can see the finite temperature effect on the free propagator.

A.4 Time-ordered propagator

We recall the time ordered propagators from Eq. A.30:

$$D(t) = \theta(t)D^{>}(t) + \theta(-t)D^{<}(t)\,, \tag{A.63}$$

and take its Fourier transform

$$D(k_0) = \int dt e^{ik_0 t} D(t)\,, \tag{A.64}$$

$$= \int dt e^{ik_0 t}(\theta(t)D^{>}(t) + \theta(-t)D^{<}(t))\,. \tag{A.65}$$

Using the representation of $\theta(t)$ from Eq. A.57 we obtain

$$D(k_0) = i\int_{-\infty}^{\infty}\frac{dk_0'}{2\pi}\left(\int_{-\infty}^{\infty} dt\left(\frac{e^{i(k_0-k_0')t}}{k_0' + i\eta}D^{>}(t) - \frac{e^{i(k_0-k_0')t}}{k_0' - i\eta}D^{<}(t)\right)\right), \tag{A.66}$$

which, with the change of the integral measure, can be written as

$$\begin{aligned} D(k_0) &= i\int_{-\infty}^{\infty}\frac{dk_0'}{2\pi}\left(\int_{-\infty}^{\infty}dt\left(\frac{e^{i(k_0')t}}{k_0-k_0'+i\eta}D^{>}(t)-\frac{e^{i(k_0')t}}{k_0-k_0'-i\eta}D^{<}(t)\right)\right), \\ &= i\int_{-\infty}^{\infty}\frac{dk_0'}{2\pi}\left(\frac{D^{>}(k_0')}{k_0-k_0'+i\eta}-\frac{D^{<}(k_0')}{k_0-k_0'-i\eta}\right), \\ &\overset{Eq.\ A.35}{\Longrightarrow} i\int_{-\infty}^{\infty}\frac{dk_0'}{2\pi}\left(\frac{(1+f(k_0'))\rho(k_0')}{k_0-k_0'+i\eta}-\frac{f(k_0')\rho(k_0')}{k_0-k_0'-i\eta}\right). \end{aligned} \tag{A.67}$$

After solving A.67 we obtain

$$D(k_0) = i\int_{-\infty}^{\infty}\frac{dk_0'}{2\pi}\left(\frac{\rho(k_0')}{k_0-k_0'+i\eta}\right)+\int_{-\infty}^{\infty}dk_0' f(k_0')\rho(k_0')\frac{\eta}{\pi((k_0-k_0')^2+\eta^2)}\ , \tag{A.68}$$

where we have represented the δ-function in the form of Lorentzian function as

$$\lim_{y\to 0}\frac{1}{\pi}\frac{y}{x^2+y^2} = \delta(x)\ , \tag{A.69}$$

and obtain

$$D(k_0) = i\int_{-\infty}^{\infty}\frac{dk_0'}{2\pi}\left(\frac{\rho(k_0')}{k_0-k_0'+i\eta}\right)+\int_{-\infty}^{\infty}dk_0' f(k_0')\rho(k_0')\delta(k_0-k_0')\ , \tag{A.70}$$

which after solving gives

$$D(k_0) = i\int_{-\infty}^{\infty}\frac{dk_0'}{2\pi}\left(\frac{\rho(k_0')}{k_0-k_0'+i\eta}\right)+f(k_0)\rho(k_0)\ . \tag{A.71}$$

We can use the spectral function in Eq A.45 for the free propagator to get the free time ordered propagator as

$$D_F(k_0) = \frac{i}{k_0^2-\omega^2+i\eta}+2\pi n(k_0)\delta(k_0^2-\omega^2)\ . \tag{A.72}$$

The finite temperature dependence can be seen from the factor $n(k_0) = 1/(e^{\beta|k_0|}-1)$ in the free time ordered propagator in Eq. A.45. We have explicitly separated out the part in the propagator due to pure quantum fluctuation and pure thermal fluctuations. Moreover since $n(k_0)$ vanishes in a system at zero temperature, we retain propagator for QFT at zero temperature.

A.5 Finite temperature field theory for scalar fields

Propagators in the imaginary-time formalism

In the previous section we discussed the time-ordered propagator in quantum statistical mechanics and showed the modification of propagator at finite (non-zero) temperature. Our motive here will be to obtain time-ordered propagator for neutral scalar fields. The Lagrangian for the neutral scalar field of mass m in a potential $\mathcal{V}(\phi)$ is given by

$$\mathcal{L} = \frac{1}{2}(\partial_\mu \phi)(\partial^\mu \phi) - \frac{1}{2}m^2\phi^2 - \mathcal{V}(\phi)\,. \tag{A.73}$$

The corresponding Euclidean action is

$$S_E(\beta) = \int_0^\beta d^4x \Big(\frac{1}{2}(\partial_\mu \phi)^2 + \frac{1}{2}m^2\phi^2 + \mathcal{V}(\phi)\Big)\,. \tag{A.74}$$

Further we can get the generating functional $Z(\beta; j)$ for $0 < \tau < \beta$ as [1]

$$Z(\beta; j) = \int \mathcal{D}\phi\ \exp\Big(- S_E(\beta) + \int_0^\beta d^4x j(x)\phi(x)\Big)\,. \tag{A.75}$$

For free-fields, i.e., $\mathcal{V}(\phi) = 0$, the generating functional Eq. A.75 takes the form

$$\begin{aligned} Z_F(\beta; j) = \int \mathcal{D}\phi \exp\Big(- \int_0^\beta d\tau \int d^3x \\ \times \Big(\phi(x)\frac{1}{2}\Big[- \frac{\partial^2}{\partial\tau^2} - \nabla^2 + m^2\Big]\phi(x) - j(x)\phi(x)\Big)\Big)\,. \end{aligned} \tag{A.76}$$

---

[1] Notation: $\int_0^\beta d^4x = \int_0^\beta d\tau \int d^3x$.

Here we took close analogy to the generating functional for the free-particle case in Eq. A.24 for obtaining the generating functional for free-fields. After integrating out $\phi(x)$ fields in the generating functional in Eq. A.76 we obtain

$$Z_F(\beta; j) = Z_F(\beta) \exp\left(\frac{1}{2}\int_0^\beta d^4x d^4y j(x)\Delta_F(x-y)j(y)\right) . \tag{A.77}$$

Here, $\Delta_F(x-y)$ in Eq. A.77 is the Green function for free-field case

$$\left(-\frac{\partial^2}{\partial\tau^2} - \nabla^2 + m^2\right)\Delta_F(x-y) = \delta(\tau_x - \tau_y)\delta(\mathbf{x}-\mathbf{y}) . \tag{A.78}$$

From Eq. A.78 we can obtain

$$(\omega_n^2 + \omega_k^2)\Delta_F(i\omega_n, k) = 1 , \tag{A.79}$$

which is the solution of Eq. A.78 in momentum space with

$$\begin{aligned} \omega_n &= \frac{2\pi n}{\beta} , \\ \omega_k &= (k^2 + m^2)^{1/2} . \end{aligned} \tag{A.80}$$

Following the procedure for free-particle case we can get the imaginary time propagator for free-field case using Eq. A.79 as

$$\Delta_F(i\omega_n, k) = \frac{1}{\omega_n^2 + k^2 + m^2} = \frac{1}{\omega_n^2 + \omega_k^2} . \tag{A.81}$$

The procedure can be extended to charged scalar fields, fermions, and photons. The main difficulty with this approach is that analytical continuation is needed to obtain the real values of the energy from the Matsubara frequencies. This is avoided in the real time formulation, but at the cost of doubling the degrees of freedom.